A STUDY OF LITHIUM/COBALT OXIDE ELECTROCHEMICAL CELLS

A thesis submitted to the

UNIVERSITY OF CAPE TOWN

in fulfilment of the requirements for the degree of

MASTER OF SCIENCE

by

Susan Delia Freese B.Sc (Hons)

National Institute for Materials Research
Council for Scientific and Industrial Research
Pretoria 0001, South Africa

September 1985

CONTENTS

Page

CHAPTER 3: THE ELECTROCHEMICAL PERFORMANCE OF HIGH TEMPERATURE LITHIUM/COBALT OXIDE CELLS 51

ACKNOWLEDGEMENTS

I sincerely thank Dr M M Thackeray for his encouragement, enthusiasm and guidance and without whose continued interest this work would not have reached completion.

I also extend my thanks to my supervisor, Professor L R Nassimbeni for his guidance and interest in this project.

Thanks are also due to my colleagues of the Electrometallurgy Division, NIMR for their friendship and support, especially Dr R Galloway and Mr B U Köhler for their advice and interest.

I wish to extend special thanks to Mr B Myers and Mr J Albain for their help with X-ray diffraction analyses; to Miss L de Picciotto for assistance with X-ray diffraction analyses and the computer programs; to Mr H Lachmann for carrying out chemical analyses using atomic absorption methods; to Mr M MacCathy of the University of Natal for his invaluable advice and assistance in the graphical work; and to Mrs N Brauckmann for typing this thesis so competently.

The Anglo American Corporation of SA is acknowledged for its financial support.

Dr J B Clark, Chief Director of the National Institute for Materials Research, CSIR, is thanked for the use of the laboratory facilities necessary for this project.

Finally, I thank my parents for their continued encouragement, interest and financial assistance and my husband for his support and enthusiasm.

PUBLICATIONS

Sections of this work have been published.

1. M M Thackeray, S D Baker and J Coetzer. The Electrochemical Behaviour of Co_3O_4 and CoO Cathodes in High-Temperature Cells. Mater. Res. Bull., 17, 405 (1982).

2. M M Thackeray, S D Baker, K T Adendorff and J B Goodenough. Lithium Insertion into Co_3O_4: A Preliminary Investigation. Solid State Ionics (1985). In press.

LIST OF ABBREVIATIONS

A/cm^2 : Amperes per centimetre squared

Å : Angstroms

^{a}/o : Atomic per cent

c.c.p. : Cubic-close-packed

h.c.p. : Hexagonal-close-packed

km : Kilometres

m.p. : Melting point

mA : Milli-amperes

μA/cm^2 : Micro-amperes per centimetre squared

mA-hr/g : Milli-ampere hours per gram

mA/cm^2 : Milli-amperes per centimetre squared

^{m}/o or mol% : Mole per cent

Ω cm^2 : Ohm centimetre squared

O.C.V. : Open circuit voltage

3D : Three dimensional

2D : Two dimensional

vs : Versus

V : Volts

Watt-hour/kg or Wh/kg : Watt hours per kilogram

Watt per kg or W/kg : Watts per kilogram

^{w}/o : Weight per cent

XRD : X-ray diffraction

ABSTRACT

The electrochemical behaviour of high temperature Li-Al/LiCl, KCl/ cobalt oxide cells was investigated.

Powder X-ray diffraction techniques were used for the qualitative analysis of the phases generated during charge and discharge of the cells.

At an operating temperature of 420 °C, maximum discharge capacities of up to 546 mA-h/g of cobalt oxide were recorded during the early charge/discharge cycles. Cell performance deteriorated with further cycling due to:

a) an instability of the cobalt oxides in the electrolyte and
b) dispersion of the discharge product, Li_2O into the electrolyte.

During discharge, Co_3O_4 was reduced via CoO to Co metal. If excess Li_2O was added to the cathodes, CoO was oxidized to Co_3O_4 on charging and further oxidation of Co_3O_4 gave rise to an unstable compound with postulated formula $Li_{2x}Co_2O_{3+x}$ for $x > 0$. CoO was the most stable cobalt oxide phase in the molten LiCl, KCl electrolyte.

An investigation of the chemical and electrochemical lithiation of Co_3O_4 at ambient temperature was also carried out. A compositional range of $0 < x < 2$ has been established for $Li_xCo_3O_4$. Powder X-ray diffraction data of $Li_xCo_3O_4$ indicate that the $[Co_2]O_4$ subarray of the spinel structure remains intact. The A-site Co^{2+} ions are displaced to empty octahedral positions to give a rocksalt phase $LiCo_3O_4$ at $x = 1$: the Li^+ ions in excess of $x = 1$ are located in tetrahedral sites.

CHAPTER 1

INTRODUCTION

1.1 SUMMARY

In this chapter the history of battery research is briefly reviewed. Existing electrochemical systems are discussed, the emphasis being placed on battery systems which have electric vehicle and electrical energy storage applications. A number of the more promising battery systems are described and a section is devoted to a review of the development of secondary high temperature cells. A discussion of ambient temperature lithium cells for low power applications follows and the structures of several transition metal oxides that have received considerable interest as cathode materials for these cells are described. The spinel and rocksalt structures are discussed in some detail and their relevance to "solid solution" electrodes stressed. Finally, the investigation of lithium/cobalt oxide cells is justified.

1.2 GENERAL

Until 15 years ago, the battery market was dominated by the rechargeable or secondary lead-acid battery and the primary, disposable zinc-carbon (Leclanché) dry cell. Since then there has been an intense international effort to develop alternative battery systems with improved electrochemical parameters, such as energy density, power generating capability, cycle life, active- and shelf-life etc. This renewed interest in battery research has been brought about by three main factors. Firstly, the 'oil crisis' of the 1970's precipitated a search for alternative forms of energy to those based on fossil fuels for electric vehicle propulsion and off-peak electrical energy storage. Both these applications require secondary batteries which provide a high current drain in the mA/cm^2 and even A/cm^2 range. Secondly, the expanding microelectronics industry has necessitated the development of miniaturized batteries which require a much lower current drain e.g. in the µA/cm^2 range. Thirdly, the NASA space programmes have required high integrity power sources which has led to the development and optimization of alternative battery systems.

Although the revival in interest in electric vehicles arose mainly out of concern over atmospheric pollution caused by petroleum-powered vehicles, it was the 'Oil Crisis' of 1973, reminding the World that fossil fuels are exhaustible, which enhanced this interest and strengthened the case for electric vehicles [1,2,3]. In 1977 the West German Institute for Geophysics and Raw Materials carried out a study [4] which concluded that world fossil fuel resources would be exhausted by 2080 and it is now obvious that shortages of liquid fuels will be one of the most serious energy problems facing the world during the next few decades. It will be possible to alleviate this problem to some degree by developing smaller, more efficient vehicles and by producing synthetic fuels from coal or biomass and reducing non-essential travel. However, none of these offers a real or long-term solution to the problem [5].

The other important application envisioned for secondary batteries is that of a storage medium for load-levelling in electric power generating plants [5,6,7,8]. Advanced batteries could enable electric energy to be stored during off-peak demand to smooth the generating load [7,8].

With the rapid expansion of the microelectronics industry in recent years, there has been considerable interest in the development of miniaturized batteries, particularly lithium batteries [9]. Most of the currently available systems are primary batteries that are presently being used for a number of applications, which include cardiac pacemakers, inertial navigation systems, watches and calculator power sources. Many of these batteries also play a host of military roles, for example, in munitions fusing and portable communications. It is therefore not surprising that the military demand for batteries has strongly influenced research in this field.

A battery converts the chemical energy that is stored in the electrode materials directly into electrical energy. As a battery discharges, electrons released from the anode, where an oxidation reaction occurs, are transferred via the external current to the cathode which is reduced. Mobile ions in the electrolyte transfer the positive or negative charge from one electrode to the other thus completing the electrical circuit (Figure 1.1). The generation of energy can be regulated by controlling the rate at which the electrochemical reaction occurs, i.e. by controlling the rate at which electrons are released to the external circuit. In a secondary battery the electrochemical reaction is reversible and the battery can be recharged. However, primary batteries, such as the Leclanché dry cell, are discarded after use. Such "disposable" batteries are costly and the hunt is now on for alternative materials that can be used in secondary batteries for both low- and high-power applications.

The requirements for each battery application are somewhat different. In all cases a battery is required with a high specific energy density (Watt-hour/kg of battery mass), but in the case of electric vehicles, an additional requirement is high specific power (Watt/kg of battery

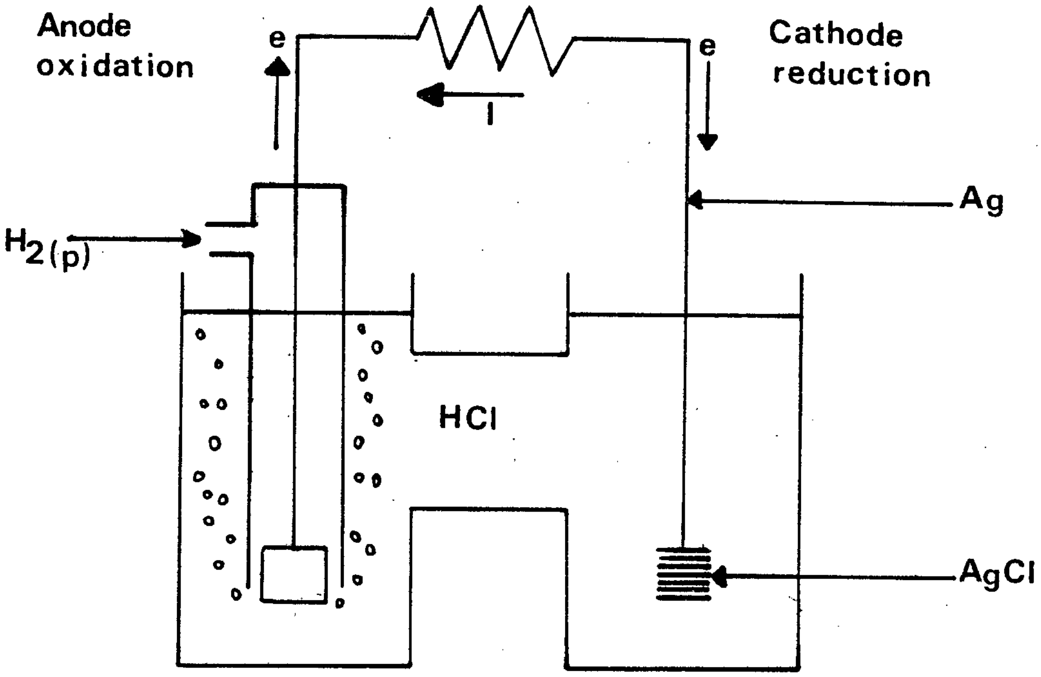

Figure 1.1:

Schematic diagram of the H_2/HCl/AgCl/Ag electrochemical cell

mass). High specific energy is necessary for compact energy storage, whereas a high specific power is dictated by the need for a vehicle to have acceptable acceleration and top speed. The Chapman report [10] suggests that batteries for electric vehicles with energy densities greater than about 80 Watt-hour/kg are required to give the vehicle a range of between 200 and 250 km. There are many varying proposals as to the requirements necessary for a vehicle to be acceptable to the public, but those proposed by Arthur D Little, Inc. for 6 common types of vehicle (Table 1.1) are generally taken to be realistic for transport applications in most developed countries [11]. From Table 1.1 it can be seen that city cars, vans and buses require energy and power densities in the region of 50-180 Watt-hour/kg and 60-130 watt/kg (peak) respectively. The private family car requires a battery of high specific power (~ 200 watt/kg peak) to provide sufficient acceleration and hill-climbing capability, and a high specific energy (>150 watt-hour/kg) to give the vehicle a practical range of about 200-300 km.

TABLE 1.1

Specifications for electric car power sources

	Small utility car	City car	Delivery van	Delivery truck	City Bus	Family car
Energy density (Wh/kg)	30-70	50-100	60-120	60-100	60-180	150-300
Peak power density (W/kg)	60-80	70-110	80-130	60-120	60-90	140-250
Cycle life	1 000 deep discharge cycles					

Among the factors affecting the specific energy are electronegativity and equivalent weight. The elements having the lowest electronegativity are those of groups IA and IIA of the periodic table, viz. the alkali and alkaline-earth metals. These elements are the most suitable for use as anodes since, as indicated by their low electronegativities, they surrender their electrons more readily than other elements. The elements with the highest electronegativities are found in groups VIA and VIIA, viz. the chalcogens and the halogens. These elements have the greatest affinity for electrons and are therefore most suitable for use as cathodes. This large difference in electronegativities provides a relatively large cell voltage. However, since low equivalent weight is also a prerequisite for high specific energy, the elements occurring early in the periodic table are the most desirable [12,13].

Specific power is improved by minimizing the electronic and electrolytic resistances of the cell and by operating the cell at elevated temperatures, which increases the exchange current density [1,12,13].

More than thirty electrochemical systems have been suggested as potential candidates for electric vehicle batteries, but many of these can be eliminated on account of the large quantities of rare materials which they require. The remaining fifteen to twenty systems each possess major barriers to commercialization and only a few of the battery candidates show some promise of being successfully developed and commercialized [5]. Most electric passenger vehicles being tested today operate on the lead-acid system, but even with great improvements in both battery performance and vehicle design, the lead-acid powered vehicles will not provide the private driver with the speed, acceleration and range that he has come to accept from petroleum powered vehicles.

1.3 REVIEW OF EXISTING ELECTROCHEMICAL SYSTEMS

1.3.1 High Energy Density/High Power Density Systems for Electric Vehicles and Energy Storage

At present, a great deal of international research is being carried out on a fairly large number of electrochemical systems. A summary of likely performance figures of some of the most commonly studied systems is given in Figure 1.2 [14]. It is important to note that none get within a factor or two of the internal combustion engine.

The most promising electrochemical systems for the near term (10-15 years) include:

i) Lead-acid
ii) Nickel-zinc
iii) Nickel-iron

These systems are already in use, or are close to commercialization. Battery systems which show some promise, but which still require a great deal of research and developmental work, include such systems as:

i) zinc-chlorine
ii) sodium-sulphur
iii) lithium-metal sulphide

Current performance figures for these systems are summarized in Table 1.2.

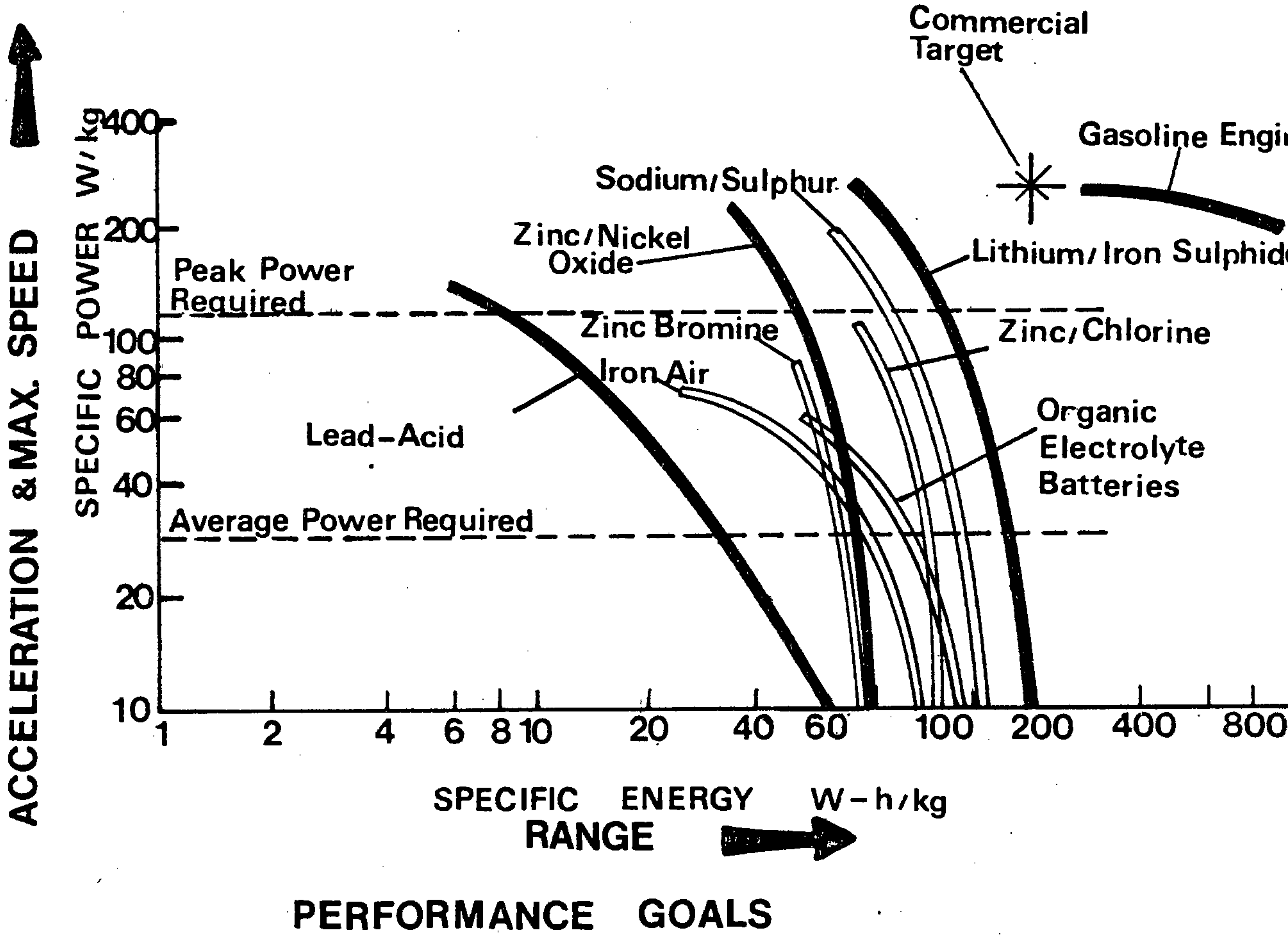

Figure 1.2 :

This figure was presented by General Motors at the Electric Vehicle Conference in Philadelphia (October 1978)

1.3.1.1 Lead-acid battery

The lead-acid battery has been used for electric traction for over a hundred years and is the most widely used secondary electrochemical system today [3,5]. The lead-acid cell in the charged state consists of a lead (Pb) anode, a lead dioxide (PbO_2) cathode and an electrolyte solution of sulphuric acid [7]. The overall cell reaction is:

TABLE 1.2

Candidate electric vehicle batteries

Battery					Current performance			
System	Electrolyte	Temp. (°C)	Open-circuit voltage (V)	Energy density (theoretical) (Watt-hour/kg)	Energy density (Watt-hour/kg)	Power (Peak) (Watt/kg)	Cycle Life	Depth of discharge (%)
Lead-acid	H_2SO_4	20-30	2,05	171	22*	50	700+	90
Lead-acid (improved)	H_2SO_4	20-30	2,05	171	30*	50-100	500+	60
Ni-Zn	KOH	20-30	1,706	321	66**	150+	400+***	65
Ni-Zn (vibrocel)	KOH	20-30	1,706	321	45-65**	-	1 200+	-
Ni-Fe	KOH	20-30	1,370	267	55**	50-100	1 500+	90
$Zn\text{-}Cl_2 \cdot 6H_2O$	$ZnCl_2$	50	2,12	465	110-151^{+++}	88-132^{+++}	400+	-
Na-S	$\beta\text{-}Al_2O_3$	300-375	1,76-2,08	664	180^{+++}	220^{+++}	300+	60
$Li/Al\text{-}FeS_2$	LiCl-KCl (eutectic)	400-450	1,8	625	70**,***	50***	250+	50
Li/Al-FeS	LiCl-KCl (eutectic)	400-450	1,6	869	40-60***	-	600+	50

* At 1-hour rate

** At 2-hour rate

***Cell only

$^{+++}$Projected figures

Cycle life depends on a number of factors, including depth of discharge, rate of charge and discharge, temperature and amount of over-charge. This information is rarely provided in full, but lifetimes given in Table 1.2 are for batteries and cells operating under deep discharge cycles required in electric vehicle applications.

$$Pb + 2H_2SO_4 + PbO_2 \underset{\text{charge}}{\overset{\text{discharge}}{\rightleftharpoons}} PbSO_4 + 2H_2O + PbSO_4$$

During the reaction, the electrodes remain solid, because lead, lead dioxide and lead sulphate are all relatively insoluble in sulphuric acid [1].

The lead-acid system has an open-circuit potential of approximately 2,05 V and a theoretical energy density of 171 Watt-hour/kg [1,5,13] (see Table 1.2). However, at present the energy densities actually achieved from conventional lead-acid batteries are around 22, 29 and 34 Watt-hour/kg at the 1-, 2- and 5-hour rates, respectively, i.e. the achievable energy density is dependent upon the discharge rate.

There are however, a number of drawbacks to the lead-acid system:

i) low energy density,
ii) slow recharging time,
iii) corrosion of the grid structure supporting the active material,
iv) the need for careful maintenance of the electrolyte; water must be added to make up that lost by electrolysis, and self-discharge reactions.

The development of 'advanced' lead-acid batteries would in fact require one or more major technological break-throughs [5].

1.3.1.2 Nickel-zinc battery

Nickel-zinc batteries have been greatly improved over the last few years and as a result, this system has emerged as one of the leading contenders for transportation applications in the near-term. However, before nickel-zinc batteries can become commercially viable, they must be able to provide a considerably greater number of charge-discharge cycles. This appears to be the only remaining major problem to their successful development [5].

In the nickel-zinc system, zinc acts as the anode, the nickel cathode is in the form of NiOOH and the electrolyte is typically 30-35% KOH [1,5]. The overall cell reaction is:

$$2\ NiOOH + H_2O + Zn \underset{charge}{\overset{discharge}{\rightleftharpoons}} 2Ni(OH)_2 + ZnO$$

This system has an open-circuit potential of 1,706 V and a theoretical energy density of 321 Watt-hours/kg [1,13] (see Table 1.2). Batteries have been built with energy densities at the two-hour rate of 66,0, 44,4 and 40,1 Watt-hours/kg by Yardney Electric Corporation, Deutsche Automobilgeseltschaft (DAUG) and AGA Innovation Centre (Sweden), respectively [1].

In spite of the high theoretical and practical energy density of the nickel-zinc battery, it has a short cycle life and this is its main drawback. The short cycle life is due to the fact that the discharge product ZnO is partly soluble in the electrolyte resulting in shape changes of the electrode structure. The solubility of ZnO also results in dendrite formation at the zinc anode during charge and in electrode densification.

Other problems found in this system include:

i) nickel electrode cost
ii) mass-production
iii) hydrogen liberation at the negative electrode
iv) separator stability
v) temperature control

General Motors has announced its intention to produce a nickel-zinc electric car for sale to the public by the mid 1980's, but this is on the assumption that a solution to the lifetime problem is found very soon.

1.3.1.3 Nickel-iron battery

Thomas Edison developed the nickel-iron battery in 1901 [5,13] and it was the most prominent secondary battery in industrial use until the 1920's. The nickel-iron battery is still widely used in Russia, but in many countries it has been almost entirely displaced by the lead-acid battery. However, recent advances in the system have revived interest in this battery.

The nickel-iron battery has an anode consisting of finely divided iron and a cathode consisting of finely divided, hydrated nickel peroxide. The electrolyte is KOH. The negative iron electrode is oxidized in two steps during discharge of the cell. Firstly, iron is oxidized to the ferrous ion. This is followed by oxidation of the ferrous to the ferric ion. Discharge of the cell is therefore characterized by the two reactions:

$$Fe + 2NiOOH + 2H_2O \underset{charge}{\overset{discharge}{\rightleftharpoons}} Fe(OH)_2 + 2Ni(OH)_2$$

$$Fe(OH)_2 + NiOOH + H_2O \underset{charge}{\overset{discharge}{\rightleftharpoons}} Fe(OH)_3 + Ni(OH)_2$$

$$Fe + 3NiOOH + 3H_2O \underset{charge}{\overset{discharge}{\rightleftharpoons}} Fe(OH_3) + 3Ni(OH)_2$$

In recent years developers of this system have concentrated on the utilization of the upper plateau reaction only [5].

The nickel-iron system has an open circuit potential of 1,370 V [1,13] and a theoretical energy density of 267 watt-hours/kg (see Table 1.2). Matsushita Electrical Industrial Company in Japan achieved 82,5 watt-hours/kg at the 5-hour rate with nickel-iron batteries tested in vehicles, while in Germany, Varta obtained 50 watt-hours/kg at the 5-hour rate. Westinghouse in the USA has achieved 44-55 watt-hours/kg from these batteries at the 2-hour rate [15].

The nickel-iron battery has a number of attractive qualities; it is the only system among the major contenders that has exhibited ruggedness and long life [5,13] (it has achieved between 1 500 and 2 000 cycles [1]), the system is virtually fool-proof electrically, little damage being incurred by deep discharge, short circuiting and overcharging. Furthermore, the batteries can be stored for long periods without corrosion or deterioration.

The major shortcomings of the nickel/iron system include:

i) high initial cost
ii) mediocre energy density
iii) poor high rate capability
iv) low cell voltage
v) poor performance at low temperatures (i.e. at ~ 0 °C)
vi) bulkiness
vii) substantial self-discharge
viii) hydrogen gassing during charge

The nickel-iron battery is, however, a major contender for use in electric buses and trucks [5].

1.3.1.4 Zinc-chlorine battery

The zinc-chlorine battery has long been recognized as offering high energy and low cost, but until fairly recently was not exploited due to the difficulty in chlorine management [5]. The principle developer of this battery has been Energy Development Associates (EDA). The unique feature of the EDA battery is the storage of chlorine as the solid chlorine hydrate by refrigeration below 9,6 °C [1,5].

The zinc-chlorine battery has an electrolyte consisting of an aqueous solution of zinc chloride and operates at a temperature around 40-50 °C. During charge, zinc is deposited on the negative plates of the battery and chlorine gas is generated at the positive plates. The circulating electrolyte replenishes the zinc chloride and removes the chlorine which is cooled and stored externally as chlorine hydrate [1,5]. The cell reaction is:

$$Zn + Cl_2 \cdot 6H_2O \underset{charge}{\overset{discharge}{\rightleftharpoons}} ZnCl_2 + 6H_2O$$

The zinc-chlorine system has an open-circuit potential of 2,12 V and a theoretical energy density of 465 watt-hours/kg (see Table 1.2). The present specific energy obtained from a zinc-chlorine battery is about 75-85 watt-hours/kg.

This battery offers very attractive possibilities as an off-peak energy-storage device and a great advantage in its favour is that the raw materials required for its manufacture are both inexpensive and readily available.

Disadvantages of this system include:

i) complexity of the system
ii) loss of energy efficiency due to the refrigeration and pumping systems
iii) lack of suitability for electric vehicle applications due to its intrinsic bulkiness and safety problems

There is however, little doubt that zinc-chlorine batteries with specific energies of about 100 watt-hour/kg and service lifetimes possibly greater than 5 years will be developed.

1.3.1.5 Development of secondary high temperature cells

In order to maximize the specific power of an electrochemical cell, the electronic and electrolytic resistances of the cell must be minimized. This can be done by selecting electrolyte materials of high ionic conductivity and electrode materials with high electrical conductivity. This can also be achieved to some extent by optimizing the cell design. The largest contribution to the internal resistance of electrochemical cells is usually made by the electrolyte [12]. As a result, it is essential to minimize the resistance of an electrolyte to maximize the specific power. This can be achieved by the use of fused-salt electrolytes, which have far lower resistivities than aqueous or organic solvent electrolytes [1,13]. Unfortunately, fused-salt electrolytes necessitate operation of the cell at a temperature above the melting point of the salts and this is usually well above 100 °C and sometimes as high as 650 °C. Operation at these elevated temperatures has the added advantage of increasing the exchange current densities (rates of the electrode reactions).

Unfortunately, operation at these high temperatures poses a number of problems, in particular with materials and seal degradation. Melting of the electrolyte salts causes large increases in volume, which poses a design problem, while the necessity of heating the battery prior to use, poses an operational problem.

(a) Sodium-sulphur battery

It was the discovery of very high sodium ion mobility above room temperature in sodium β-alumina by Weber and Kummer at Ford in 1967 [16] that led to the concept of a sodium-sulphur battery with a solid electrolyte operating at elevated temperatures [17,18]. As a result, the sodium-sulphur cell is the only cell discussed here under the secondary high-temperature battery systems which does not have a fused-salt electrolyte.

β-alumina has a layer structure as shown in Figure 1.3. Four layers of close-packed oxygen atoms contain four-fold and six-fold co-ordinated aluminium in an atomic arrangement analogous to that found in spinel, $MgAl_2O_4$. The formula of β-alumina, $Na_2O{\bullet}xAl_2O_3$ where x is in the range 8 to 11, is not compatible however, with an infinitely extending spinel structure. A deficiency of aluminium results in every fifth layer of oxygen atoms being only one-quarter filled and it is in this partially empty layer that the sodium ions are found [19,20].

The unusual electrical properties of β-alumina were only discovered recently by Weber and Kummer, although the crystal structure was essentially solved many years earlier [21]. When the electrical conductivity at 300 °C was measured, it was realized that the current was carried exclusively by sodium ions and not by electrons.

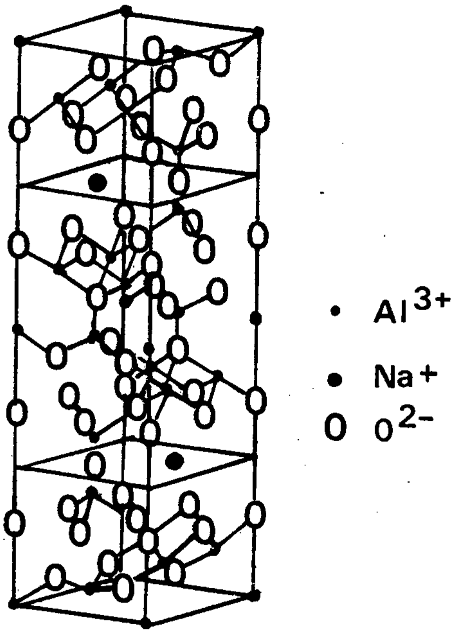

Figure 1.3:
The β-alumina structure. The densely populated close-packed 'spinel blocks' containing aluminium and oxygen ions separate the mirror planes which contain the mobile sodium ions. The density of oxygen atoms in the mirror planes is only one-quarter of that in the spinel blocks. The separation between mirror planes is just over 11 Å.

In terms of the requirements of high energy/high power density, the sodium-sulphur cell is most attractive. Since the active materials, sodium and sulphur, are both liquid at the operating temperature (300-375 °C), the solid β-alumina electrolyte physically separates the molten electrodes and at the same time allows transport of Na^+ ions from one electrode to the other during charge and discharge of the cell. The sodium-sulphur cell is made up of a tube of β-alumina containing a liquid sodium anode and surrounding this, an annulus of graphite felt loaded with liquid sulphur which serves as the cathode [1,5,7,12,22]. The graphite felt is necessary to provide current collection at the cathode since sulphur is not electronically conducting.

The cell reaction can be written as:

$$xNa^+ + xe^- + yS \underset{\text{charge}}{\overset{\text{discharge}}{\rightleftharpoons}} Na_xS_y \qquad [12]$$

However, the reaction mechanism of the sulphur electrode is quite complex. For the first 60% of discharge, sulphur is converted to sodium pentasulphide (Na_2S_5), which is immiscible with sulphur. The open-circuit voltage of the cell is constant at 2,08 V throughout this stage as the cathode is two-phase. Further discharge results in the transformation of Na_2S_5 to a single-phase polysulphide with a composition between Na_2S_3 and $Na_2S_{2,7}$ at 360 °C. For the single-phase region, the open-circuit voltage falls continuously to 1,76 V and then remains constant as solid Na_2S_2 begins to separate out in the melt. In order to keep all the phases liquid throughout the compositional range, the sodium-sulphur cell must be operated between 300 and 375 °C. The discharge curve of a sodium-sulphur cell under load is depicted in Figure 1.4.

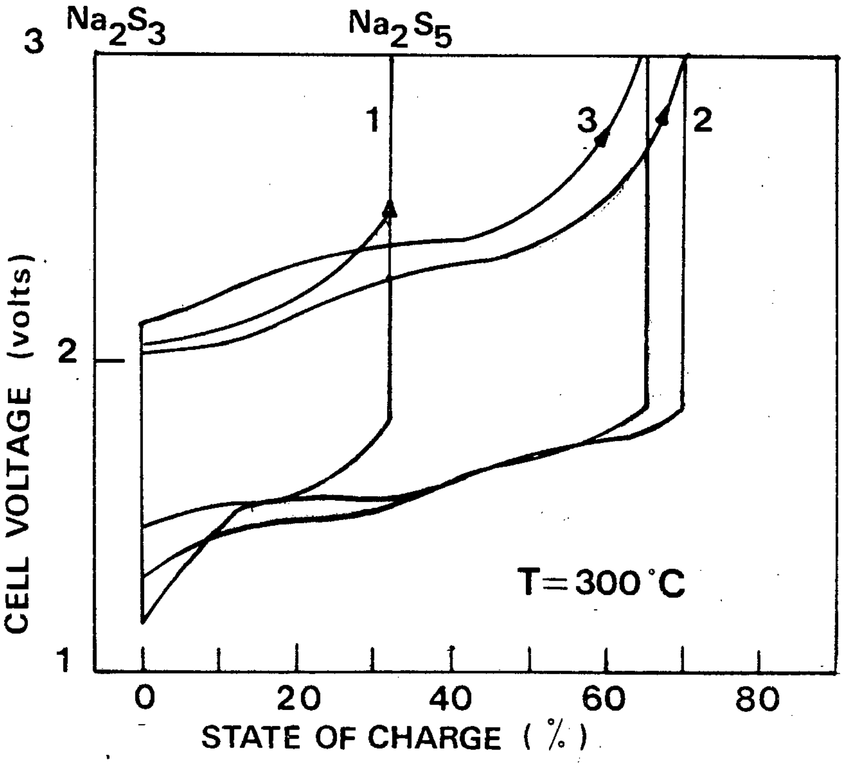

Figure 1.4:
Charge discharge behaviour of three Na-S cells with a current density of 80 mA/cm^2. Cell 1: Cathode chamber filled with carbon felt and sulphur. Cell 2: Cathode chamber filled with graphite felt and sulphur: vertical channels free from felt at the electrolyte tube. Cell 3: Cathode chamber filled with graphite felt and sulphur + 0,8 at.% Se + 0,8 mol.% B_2S_3 [7].

The sodium-sulphur cell has a theoretical energy density of about 750 watt-hours/kg which makes this system particularly attractive.

Although this cell is in an advanced state of development, there are a number of technical problems besetting this system, the major ones being:

i) difficulty in the manufacture of β-alumina
ii) limited durability of the β-alumina tubes
iii) safety - in the event of tube failure, there would be a violent reaction between molten sodium and sulphur
iv) corrosion of cell components by the sodium polysulphides at the cell operating temperature [23].

(b) Lithium-aluminium/iron sulphide battery

The lithium-aluminium/iron sulphide battery is currently under development at the Argonne National Laboratory in the USA. Iron sulphide has been investigated as a positive electrode material [1,5,7,8,24] mainly as a consequence of the failure to develop high-temperature lithium cells due to the high volatility of elemental sulphur. The problem of containing the sulphur electrode was circumvented by employing a solid iron sulphide electrode (either FeS_2 or FeS). The electrolyte of this battery is a molten salt consisting of a eutectic mixture of LiCl/KCl that melts at 352 °C. Elemental lithium is also molten at the operating temperature of this battery (450 °C), but this can be immobilized by alloying it with aluminium to form a solid electrode without incurring too much loss in lithium activity. When FeS_2 is the active cathode material the battery discharges in two stages according to the following reactions:

$$2\text{Li (alloyed with Al)} + FeS_2 \underset{\text{charge}}{\overset{\text{discharge}}{\rightleftharpoons}} FeS + Li_2S \qquad [25]$$

$$2\text{Li (alloyed with Al)} + FeS \underset{\text{charge}}{\overset{\text{discharge}}{\rightleftharpoons}} Fe + Li_2S \qquad [26]$$

$$4\text{Li (alloyed with Al)} + FeS_2 \underset{\text{charge}}{\overset{\text{discharge}}{\rightleftharpoons}} Fe + 2Li_2S$$

The use of lithium-aluminium alloys and iron sulphide electrodes has resulted in the development of practical cells delivering energy densities of ~ 70 watt-hours/kg at the 2-hour rate and peak densities of ~ 50 watts/kg and having lifetimes of 200-250 cycles. Argonne National Laboratory's long-term target energy density is 175-185 watt-hours/kg at the 4-hour rate and the target power density is greater than 100 watts/kg at 50% discharge. The upper voltage plateau occurs at 1,6 V and the lower at 1,3 V.

Unfortunately, a number of problems are encountered with the lithium-aluminium/iron sulphide system. The iron sulphide electrode suffers from excessive swelling of the positive electrode [8]. Furthermore, the upper plateau reaction is not completely reversible and this has cast doubt upon the potential usefulness of the Li-Al/FeS_2 system [14].

Another problem encountered with iron sulphide electrodes is due to a reaction that occurs between the iron sulphide and the potassium ions of the LiCl-KCl electrolyte to form a Li-K-Fe-S compound, designated the J-phase [1,14,27]. This reaction causes high polarization, which results in low utilization of the active material in the positive electrode. The addition of Cu_2S to the FeS electrode modifies the J-phase [1,28] and reduces the polarization of the electrode, thereby resulting in a high utilization of the theoretical capacity [1,29].

Lithium plating during charge is another source of problems in the Li-Al/FeS_2 cells. This produces dendritic growth which eventually results in short-circuiting of the cell [14]. In addition, expensive materials are required as electrode separators [1].

In order to improve the electrical conductivity of the iron sulphide electrode, current collectors must be added to obtain a better utilization of the active material at high current rates. Unfortunately, this creates yet another problem, since most common metallic electronic conductors react with metallic sulphides at elevated temperatures. Only graphite and molybdenum have been found to be stable in the cell environment. Molybdenum, however, is too scarce and expensive to make it commercially attractive [14].

There are a number of problems hindering the successful development of this battery, but it has emerged as one of the most promising intermediate-term batteries for electric vehicle propulsion.

(c) Lithium-aluminium/transition metal oxide systems

Iron oxide cathodes

Transition metal oxides are attractive alternatives to their sulphide counterparts because of their less corrosive nature [30]. Furthermore, transition metal oxides offer higher electrode capacities on account of the lower mass of oxygen compared to sulphur [31].

Lithium-aluminium/iron oxide systems have been investigated using α-Fe_2O_3 and Fe_3O_4 cathodes [31]. These systems were tested using a cell design similar to that of the FeS_2 system described above: the electrolyte was the molten eutectic salt, LiCl/KCl. These systems were found to operate reversibly at 420 °C. In general, cells with α-Fe_2O_3 and Fe_3O_4 cathodes exhibited similar discharge characteristics. In view of a report [32] that lithium can be incorporated into α-Fe_2O_3 at ambient temperature, the structural characteristics of cathodes in high temperature Li-Al/LiCl, KCl/ α-Fe_2O_3 cells were investigated recently [33]. It was found that if the reaction were characterized by a continuous insertion of lithium into, and iron extrusion from, the cubic-close-packed oxide lattice of Fe_2O_3, it would be possible to characterize every phase of the cathode during the reaction by the compound $Li_xFe_{2-x/3}O_3$ for $0 < x < 6$. The reaction sequence could then be represented by:

$$\alpha\text{-}Fe_2O_3(\text{h.c.p.}) \xrightarrow{420\ ^{\circ}C} \gamma\text{-}Fe_2O_3(\text{c.c.p.})$$

$$\text{I} \quad \updownarrow \quad 0{,}375\ Li$$

$$Li_{0,375}Fe_{1,875}O_3(LiFe_5O_8) + 0{,}125\ Fe$$

$$\text{II} \quad \updownarrow \quad 1{,}125\ Li$$

$$Li_{1,5}Fe_{1,5}O_3\ (LiFeO_2) + 0{,}375\ Fe$$

$$\text{III} \quad \updownarrow \quad 2{,}250\ Li$$

$$Li_{3,75}Fe_{0,75}O_3\ (Li_5FeO_4) + 0{,}75\ Fe$$

$$\text{IV} \quad \updownarrow \quad 2{,}250\ Li$$

$$3Li_2O + 0{,}75\ Fe$$

This is the reaction sequence proposed by Godshall et al. [30] in a study of the ternary Li-Fe-O system at 400 °C assuming that thermodynamic equilibrium is always attained during each stage of the discharge reaction.

Three features of this reaction sequence should be highlighted:

i) during discharge, lithium is inserted into, and iron extruded from a cubic-close-packed oxide lattice; this process is reversible.

ii) for $0 < x < 1{,}5$, lithiation of γ-Fe_2O_3 (spinel) to yield α-$LiFeO_2$ (rocksalt), via $LiFe_5O_8$ (spinel), results in complete occupation of the octahedral sites of the structure. During the transition from spinel to rocksalt the unit cell volume decreases by 1%. During the transition α-$LiFeO_2$ to Li_2O (antifluorite-type structure), cations migrate from octahedral to tetrahedral interstices; the increase in volume associated with this transition is massive (36,41%)*.

iii) the limited solubility of the lithium-iron-oxide phases in the molten LiCl/KCl electrolyte accounts for the good coulombic efficiencies and lifetimes reported earlier for this type of cell [31]. It is only on deep discharge, with the generation of Li_2O and its slow dispersion into the electrolyte, that a gradual deterioration in cell performance occurs.

---

*Note: Detailed descriptions of the spinel and rocksalt structures are given later in Sections 1.4.2 and 1.4.3.

Although the Li-Al/LiCl, KCl/α-Fe_2O_3 system has a relatively low average operating voltage (~ 1 V), it still offers a high energy density (~ 400 watt-hours/kg) based on the masses of the electrode materials only. This energy density can be achieved for many months of continuous cycling, provided that the cells are not discharged too deeply. One disadvantage of this system is its power capability, which is significantly inferior to the Li-Al/FeS_2 system. The experiments do, however, indicate that transition metal oxides/sulphides having a spinel or rocksalt structure, can be effectively used in high temperature lithium cells.

1.3.2 Ambient temperature lithium cells for low power applications

The reaction of lithium with most solid inorganic compounds that might be considered for use as cathode materials, involves either a displacement reaction such as the hypothetical one shown below:

$$2MO_2 + 2Li \longrightarrow M_2O_3 + Li_2O$$

or a lithium insertion reaction characterized by:

$$xLi + MO_2 \longrightarrow Li_xMO_2$$

Displacement reactions involve extensive bond breakage, atomic reorganization and formation of new bonds, which in many cases are not reversible. However, one type of reaction which is generally reversible is the intercalation reaction. An ideal intercalation reaction involves the insertion of a guest species into a host lattice with minimal structural rearrangement of the host [2,6,7,34,35]. Although there is no bond breakage within the host during an intercalation reaction, the bonds may be slightly perturbed, as for example when a slight expansion of the host structure occurs. Reactions similar to intercalation reactions, which also depend on the structure of the host, but in which larger structural modifications, such as bond cleavage, occur, are termed topotactic or topochemical reactions. These reactions may, or may not, be reversible, depending on the specific nature of the structural changes. Unfortunately, the terms intercalation, topotactic and topochemical are often used interchangeably, whereas it would be more accurate to include these terms under the broader term of insertion.

It has been found that many transition metal oxides and sulphides can reversibly accommodate hydrogen or alkali-metal ions into their structure over a wide range of solid solution and are therefore of interest as possible cathode materials in batteries [36]. Such electrodes are commonly called "solid-solution electrodes".

Such insertion/extraction reactions with a host matrix at ambient temperatures are not only of technical interest, for example in battery research, but are also of scientific interest. Scientifically, such reactions permit low-temperature synthesis of compounds that may be inaccessible by high-temperature techniques. In particular, unusual formal valence states and/or ionic ordering may be realized [37]. Low temperature lithiation can be readily achieved electrochemically [38] or chemically by use of n-butyllithium [39].

From a technical viewpoint, the amount of power that can be delivered by an electrochemical system is determined by the rate of ionic transport in the anode, cathode and the electrolyte. It has only recently been appreciated that the reversibility and rate of a chemical reaction in a lithium cell are greatly influenced by the structure of the cathode before, during and after the reaction. The appreciation of this structure-property relationship has led to research into a number of transition metal oxides and transition metal chalcogenides which possess particularly unusual and interesting crystal structures [30,38,40,41,42,43,44] in an attempt to find improved cathode materials.

Several transition metal oxides and sulphides that have received considerable interest as cathode materials for ambient temperature lithium batteries, will be discussed in this section. Particular emphasis will be placed on the structural characteristics of the oxide cathodes. These will include:

i) TiS_2
ii) $LiCoO_2$
iii) ReO_3
iv) the vanadium oxides, V_2O_5, V_6O_{13} and VO_2
v) WO_3
vi) β-MnO_2
vii) γ-MnO_2
viii) spinel electrodes
    a) Fe_3O_4
    b) Mn_3O_4 and $LiMn_2O_4$

1.3.2.1 TiS_2

The possibility of insertion compound electrodes for non-aqueous ambient temperature secondary batteries of high specific energy and power was first demonstrated with the Li/TiS_2 cell in 1976 [38]. Lithium was reversibly inserted into and extracted from a TiS_2 cathode, Li_xTiS_2 over the compositional range $0 \leqslant x \leqslant 1$. TiS_2 is considered highly attractive for use as a cathode material in lithium batteries because it possesses a number of desirable properties [45], namely:

i) a high free energy of reaction, i.e. a large ΔG
ii) a small variation in free energy change during reaction
iii) little structural change on reaction
iv) high reversibility of the chemical reaction
v) a good electronic conductivity
vi) high diffusivity of lithium ions in the structure
vii) no solubility in common electrolytes

TiS_2 consists of layers of sulphur-titanium-sulphur sandwiches, between which there is no chemical bonding but only weak Van der Waals' bonding (see Figure 1.5). Therefore, lithium ions can be readily inserted between these layers into the "Van der Waals' gap" without radically altering the overall structure [38]. The lithium and titanium ions reside in alternate layers. In $LiTiS_2$ the lithium and titanium ions occupy all the octahedral interstices of the structure in alternate layers of the close-packed sulphur lattice [46]. Lithium insertion is accompanied by an expansion of the "c" unit cell axis.

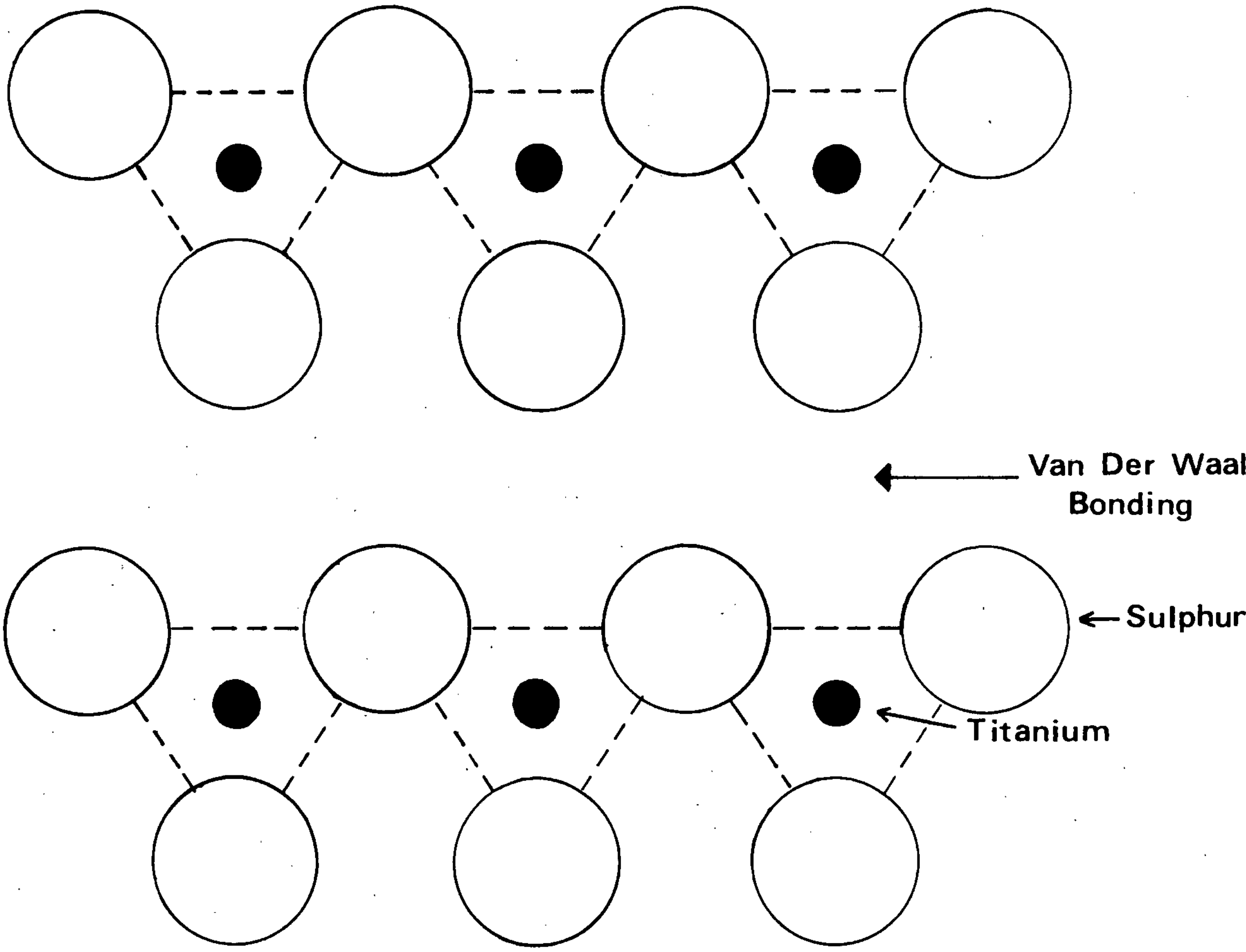

Figure 1.5:
Structure of TiS_2 looking down the B axis. The atoms are all in the same plane [38]

The intercalation and de-intercalation of lithium with TiS_2 has been accomplished more than 600 times [47], indicating that true intercalation reactions can form the basis of secondary batteries. Such TiS_2 cells have been manufactured as small button cells for watches, but before large lithium batteries can be made commercially available, safe high-rate electrolytes have to be found.

1.3.2.2 $LiCoO_2$

$LiCoO_2$ is a layered transition metal oxide which has the $CdCl_2$-type structure [48,49] in which the anions form a close-packed pseudocubic array. The Li^+ and Co^{3+} ions reside in octahedral sites in alternate layers formed by the anion lattice as shown in Figure 1.6.

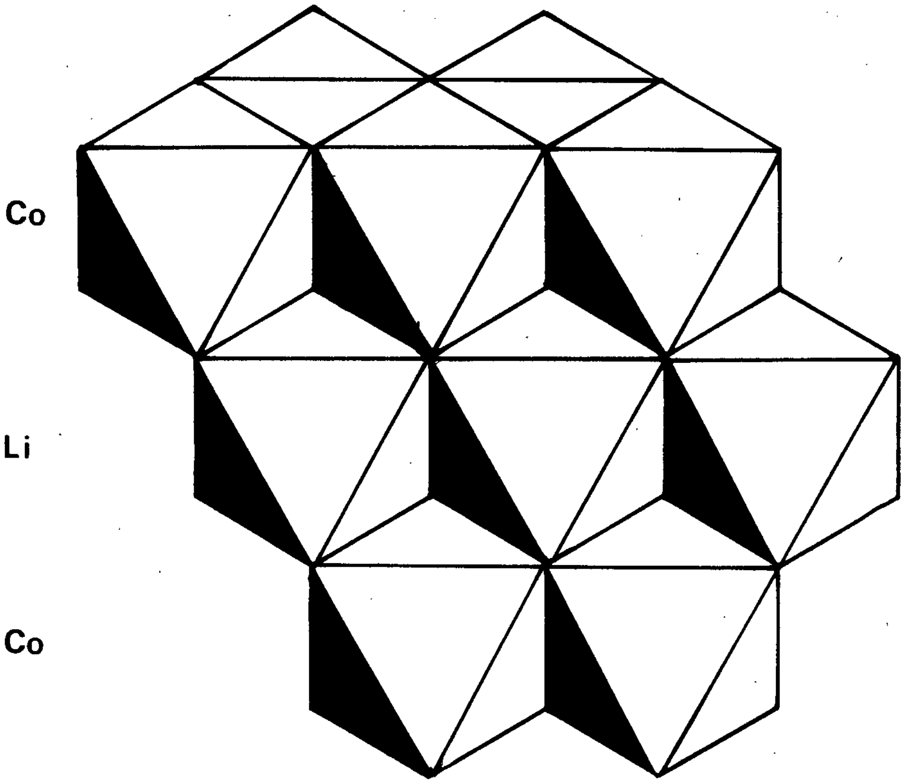

Figure 1.6:
Schematic diagram of the $LiCoO_2$ structure [48]

Mizushima et al. [48] have investigated the electrochemical extraction of lithium from $LiCoO_2$ at room temperature to form Li_xCoO_2 ($0 < x \leq 1$). They found that preliminary voltage-composition curves showed low overvoltages and good reversibility over a large range of x. It was also demonstrated that during lithium extraction the CoO_2 sublattice remained intact.

1.3.2.3 ReO_3 and related structures

A class of compounds that is very interesting as potential hosts in practical rechargeable cells is formed by those based on the ReO_3 structure. The ReO_3 structure consists of octahedra extending in all three directions through corner sharing only. This type of connection produces cavities in the structure which, as noted by Murphy [6,50], are perovskite-like. The mineral, perovskite, $CaTiO_3$, has a structure in which the oxide ions and the large cations (Ca^{2+}) form a cubic close-packed array in which the smaller cation (Ti^{4+}) occupies those octahedral interstices formed exclusively by oxide ions as shown in Figure 1.7. Figure 1.8 shows how the octahedra in the ReO_3 structure may generate this perovskite-like cavity.

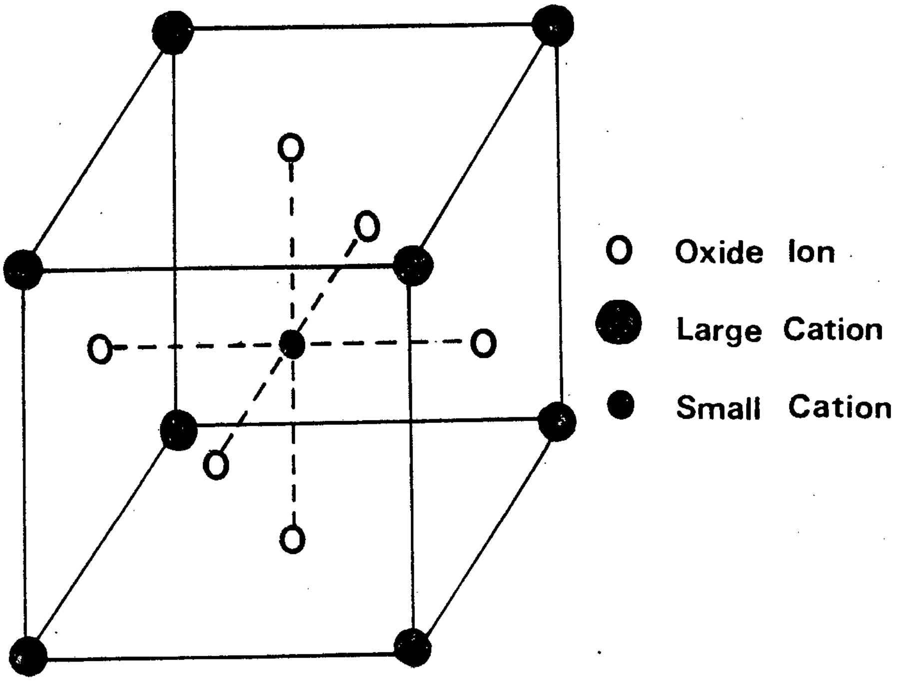

Figure 1.7:
The perovskite structure [39]

Connection of the square faces of the cavities produces channels which run in three perpendicular directions and are expected to ensure fast Li^+ mobility. However, it has been demonstrated that cubic ReO_3, on acceptance of more than one Li^+/mole, turns to rhombohedral $LiReO_3$ and

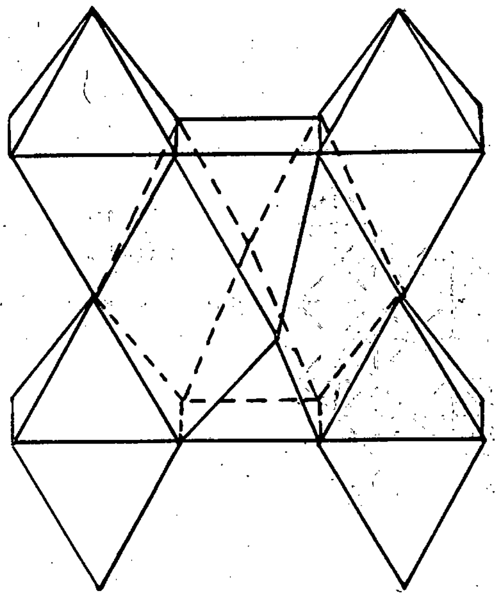

Figure 1.8:
Perovskite-like cavity of ReO_3

Li_2ReO_3 phases [51,52]. This transformation accounts for the slow electrochemical Li^+ uptake/removal and has been explained on the basis of a twisting of the ReO_3 lattice about the shared corners. This twist transforms a 12-coordinate cavity into two 6-coordinate octahedral cavities sharing faces. It is only the extreme flexibility of this structure, in which the building units are only corner shared, that make the occurrence of this 'twisting' phenomenon feasible. By introducing edge sharing into the structure, twisting may be largely controlled, although the directions for Li^+ diffusion are then reduced from 3 to 2, or even to 1 [49].

1.3.2.4 The vanadium oxides, V_2O_5, V_6O_{13} and VO_2

Edge sharing in ReO_3-related structures may be induced by shear mechanisms, such as observed in the vanadium oxides, V_2O_5, V_6O_{13} and VO_2 [6,53,54]. These vanadium oxides may be thought of as derived from ReO_3 by a first shear mechanism in the case of V_2O_5, and by a second shear mechanism in the case of V_6O_{13} and VO_2 as shown in Figure 1.9.

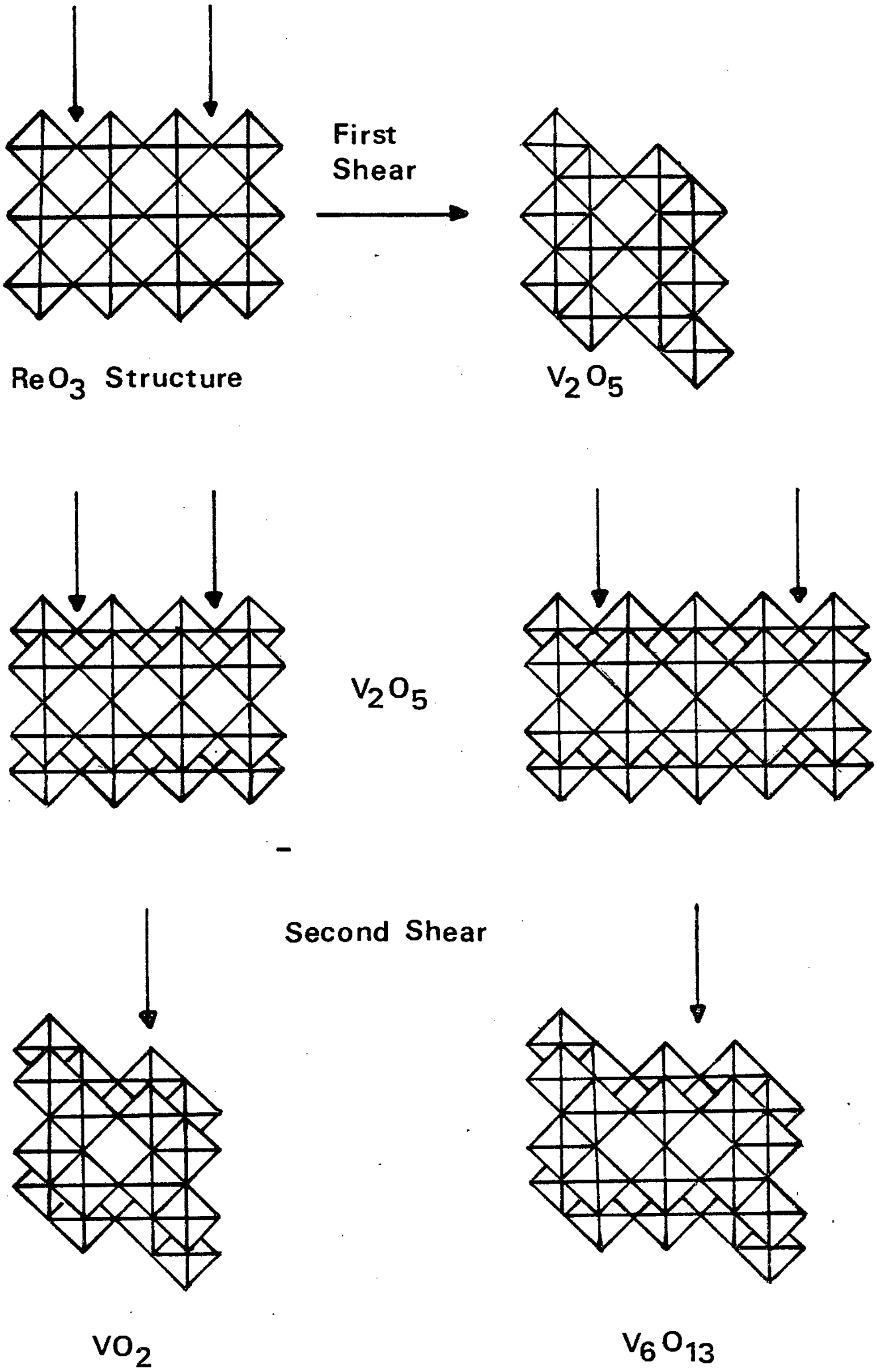

Figure 1.9:

Formation of V_2O_5 (first shear) and of V_6O_{13} and VO_2 (second shear) from ReO_3. The arrows indicate the shear planes [53].

Although the V_2O_5 structure may be considered as being constructed of "V_2O_5 ribbons" formed by the shearing of two ReO_3 chains together, this is an over-simplification. The true V_2O_5 structure is considerably distorted from this, the coordination being closer to trigonal bipyramidal than octahedral, making V_2O_5 a layer compound as shown in Figure 1.10.

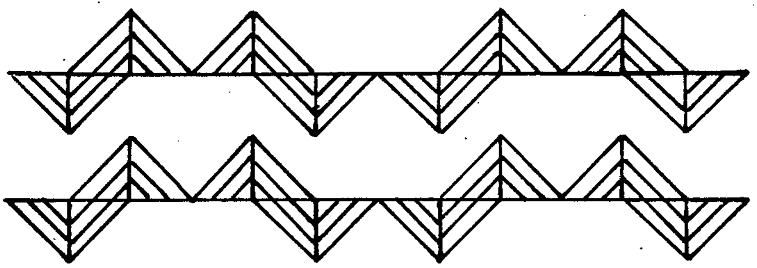

Figure 1.10:

The V_2O_5 structure: trigonal bipyramidal representation [55].

This arrangement allows for easy insertion of electropositive species into the oxide matrix [55] and lithium may be intercalated chemically or electrochemically into the V_2O_5 lattice to give the ternary phases $Li_xV_2O_5$ ($0 < x < 2,0$) [38,39]. It has been shown that V_2O_5 can be used reversibly in non-aqueous high-power lithium cells [56].

The phases in the ambient temperature $Li_xV_2O_5$ system have been investigated in the range $0 < x < 1,0$ [41,57]. At low lithium content ($x < 0,1$), phase I, with lattice parameters very close to those of V_2O_5 and isostructural with the known high-temperature α-$Li_xV_2O_5$ [58], is formed by insertion of lithium between the V_2O_5 layers. There are two other distinct phases occurring between $0,1 < x < 1,0$, both with ranges of homogeneity. These also have lattice constants closely related to those of V_2O_5, indicating that topochemical insertion of lithium occurs.

The structure of V_6O_{13} is the most interesting of the vanadium oxides from an electrochemical point of view (see Figure 1.11). V_6O_{13} consists of edge-shared octahedra forming single and double zig-zag chains linked together by further edge-sharing. The resulting sheets are interconnected by corner-sharing, thus giving a three dimensional framework which is relatively open [49,55]. This fact, coupled with its metallic conductivity, has led to the investigation of V_6O_{13} as a potential cathode material for non-aqueous lithium cells.

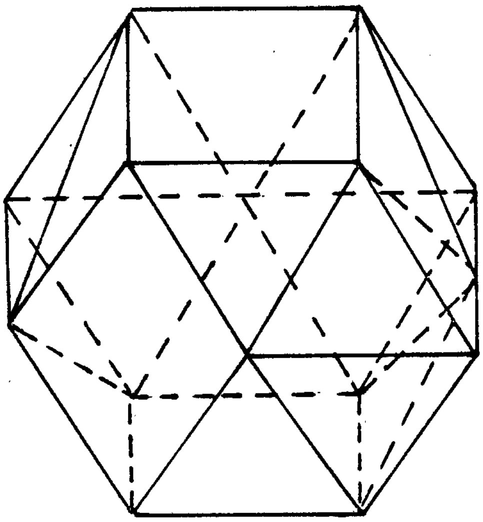

Figure 1.11:
Cavity of V_6O_{13} .

The reversible electrochemical behaviour of V_6O_{13} versus lithium is observed for up to one lithium per transition metal [50]. Reaction with n-butyllithium suggests that a final stoichiometry of $Li_8V_6O_{13}$ may be attainable electrochemically if the particle size is small enough. At present V_6O_{13} appears to be very promising for use as a battery cathode. Its average potential versus lithium is 2,2 V and has a theoretical energy density of 800 watt-hours/kg based on eight lithiums per V_6O_{13} [59].

1.3.2.5 WO_3

Corner-sharing between octahedra can give rise to structures other than the ReO_3-type. An interesting example is provided by the recently prepared hexagonal WO_3. This structure consists of WO_6 octahedra which are connected in such a way as to form a wide hexagonal channel running through the structure [60]. What is interesting about these compounds endowed with large tunnels, is the capability of accepting considerably higher amounts of Li^+ than their perovskite-like counterparts. Monoclinic WO_3, having the typical ReO_3 structure, may only intercalate 0,67 Li^+ per W [61], whereas hexagonal WO_3 accepts $2Li^+$ per W [60].

1.3.2.6 β-MnO_2

β-MnO_2 has the rutile-type structure. This structure can be described as an hexagonal close-packed oxygen lattice based on edge-sharing octahedra forming infinite chains in one direction. These chains are linked by corner-sharing, thus forming unidirectional channels containing one octahedral or two tetrahedral sites for Li^+ [49] (see Figure 1.12).

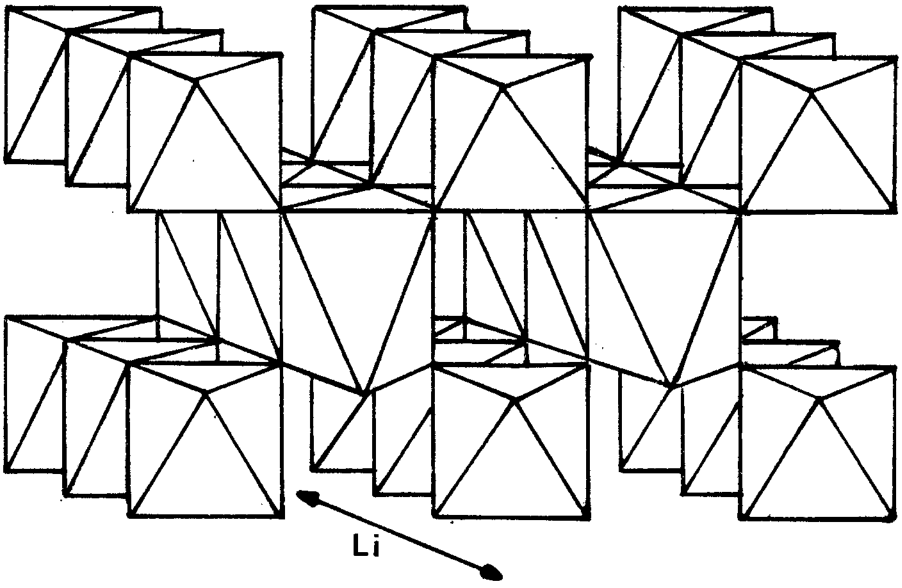

Figure 1.12:
Rutile structure showing channels along [001] for Li^+ diffusion [62].

Murphy et al. [62,63] have investigated a number of rutile-type oxides and found that their ability to insert Li^+ correlates with unit cell volume and electronic conductivity. A good electronic conductivity facilitates lithium insertion by having a screening effect on the repulsion forces between Li^+ ions. A large cell volume corresponds to large channel sizes within the structure, which also enhances insertion. Hong [64] has pointed out that, from a geometrical point of view, the bottleneck formed by a square planar array of oxygen ions is usually sufficient to allow jumping of Li^+ from site to site. However, the situation is rather less favourable for the rutiles, because each Li^+ has to pass through a transition state based on three oxygen ions. As a result, only rutile-type structures with relatively large channels may incorporate appreciable amounts of Li^+. Therefore, although this class of compounds provides interesting examples of unidirectional channels able to accommodate Li^+ ions, none have so far proved useful for battery applications [49].

Recent reports have shown that up to ~ 0,2 Li^+ ions can be incorporated within the channels of the rutile structure [65]. Prolonged reaction of β-MnO_2 with n-butyllithium transforms the rutile phase into the spinel $LiMn_2O_4$ [37].

1.3.2.7 γ-MnO_2

Although this material has been linked with the spread of lithium batteries in the market, little is known about the mechanistic aspects of lithium incorporation in its structure [49]. γ-MnO_2 is used as the starting material for cathodes of both aqueous and non-aqueous cells and has a structure consisting of a ramsdellite matrix (double chains of edge-shared MnO_6 octahedra) containing random areas of pyrolusite (single chains of edge-shared MnO_6 octahedra which are rutile-like) as shown in Figure 1.13.

On heating, the γ-MnO_2 structure alters to form so-called γ/β- and β-phases [67]. In terms of capacity and energy density, the γ/β-phase has been found to be the most efficient [68,69], but the reason why it performs better than the β-phase is not yet clearly understood. Voinov [70] has shown that in γ/β-MnO_2, Li^+ ions occupy corner-shared tetrahedral sites only, but so far, the reversibility of this process has received little attention. Pistoia [49] has carried out preliminary investigations and observed that a γ/β-phase cycles in a less satisfactory way than a pure γ-phase which confirms the findings of Manev [71]. This result is in agreement with X-ray analyses which show

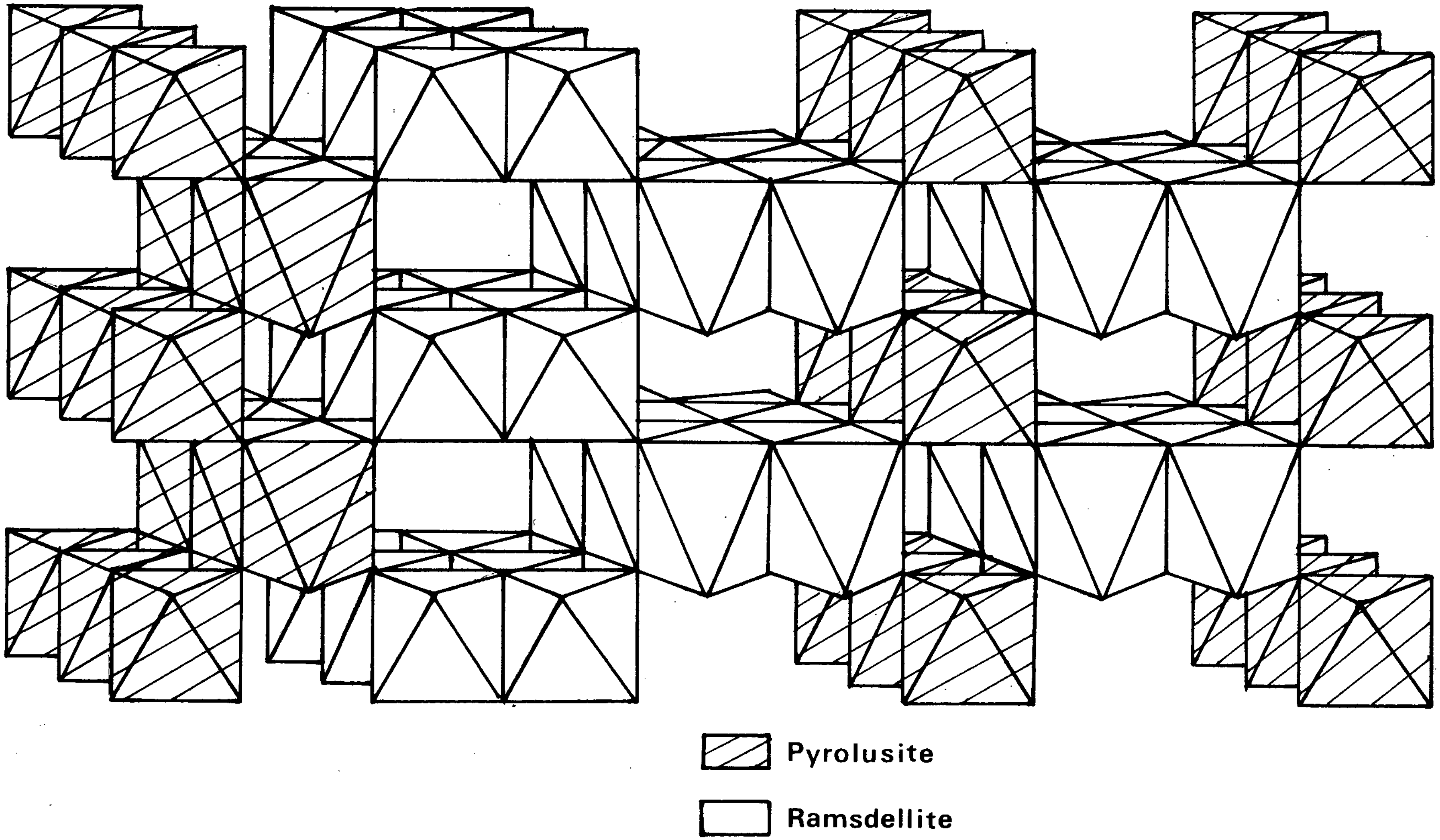

Figure 1.13:

Idealized representation of the nsutite (γ-MnO_2) structure. Pyrolusite domains indicated by shaded octahedra [66].

structure retention to a large degree during lithium insertion into γ-MnO_2 and significant alterations in structure for lithium insertion into γ/β-MnO_2 [67]. However, an explanation for this is not available as yet.

1.3.2.8 Spinel electrodes

(a) Fe_3O_4

Until recently, investigators of insertion compounds for battery applications had concentrated predominantly on compounds having layered, 2-dimensional (2D) structures such as TiS_2 and Li_xCoO_2. However, initial studies [31] on magnetite, Fe_3O_4, which has a spinel-type structure revealed that the $[B_2]X_4$ subarray of the $A[B_2]X_4$ spinel provides a close-packed anionic, 3-dimensional framework for Li^+ ion transport and that Fe_3O_4 itself could accept up to one Li^+ ion per formula unit.

X-ray diffraction data of $Li_{1.5}Fe_3O_4$ [32] indicated that almost all (>98%) of the iron ions are situated on octahedral positions. This implies that during the lithiation process, Fe^{3+} ions, which normally reside in tetrahedral sites, are reduced and displaced by the inserted lithium ions into neighbouring, empty octahedral sites via a common tetrahedral/octahedral face. An important observation was that during the whole of the lithiation process, the $[Fe_2]O_4$ or $[B_2]X_4$ framework of the spinel structure remained intact.

The diffusion rates of lithium ions into the close-packed structure of Fe_3O_4 are much slower than those into the layered TiS_2 and $Li_{1-y}CoO_2$ structures. This is not surprising when one considers the rigid character of the spinel framework. It has been shown by direct observation [72] that the Van der Waals-bonded layers of TiS_2 are prised apart by lithiation of TiS_2. In the Fe_3O_4 spinel, the framework is volume-constrained and diffusion of lithium ions through a common tetrahedral-octahedral face is restricted by a more severe interface bottleneck [32].

(b) Mn_3O_4 and $LiMn_2O_4$

Following the discovery that the $[Fe_2]O_4$ spinel framework of Fe_3O_4 provided a 3-dimensional space for Li^+ ion diffusion, an investigation of the lithiation of the spinels Mn_3O_4 and $LiMn_2O_4$ was undertaken at ambient temperatures [37]. Hausmannite, Mn_3O_4 was chosen because it is analogous to magnetite, Fe_3O_4 and cubic $LiMn_2O_4$ was investigated because it offers the possibility of having only lithium ions in the interstitial space of the $[Mn_2]O_4$ framework of the system $Li_{1+x}[Mn^{3+}_{1+x}Mn^{4+}_{1-x}]O_4$. The manganese oxides are of particular interest because manganese is stable in octahedral sites over a wide range of oxidation states, from Mn^{2+} through Mn^{3+} to Mn^{4+}.

Hausmannite, Mn_3O_4 is an electronic insulator on account of its valence distribution. Mn^{3+} is a d^4 ion and therefore has an orbitally degenerate ^5Eg ground state in the cubic phase which produces a cooperative Jahn-Teller distortion to tetragonal symmetry [73]. It was realised [37] that if lithiation of Mn_3O_4 reduces Mn^{3+} to Mn^{2+} as $Li_xMn^{2+}[Mn^{3+}_{2-x}Mn^{2+}_x]O_4$, then the magnitude of the tetragonal c/a ratio and the tetragonal-cubic transition temperature T_t should decrease with increasing x. It should therefore be possible to demonstrate directly that the charge-compensating electrons occupy d states of the host array by monitoring the room temperature lattice parameter.

In the case of $LiMn_2O_4$, previous studies [74] had shown that a cooperative Jahn-Teller distortion to tetragonal symmetry should occur for $x \approx x_c$, where the critical Mn^{3+} ion concentration can be expected to fall in the range $0 < x_c < 0{,}2$. Since the cubic-tetragonal transition is first order [75], a two-phase region can be expected for $0 < x < 1$.

X-ray diffraction analyses [37] showed that the $[Mn_2]O_4$ subarray of the $A[B_2]X_4$ spinels remains unperturbed during lithiation of Mn_3O_4 and $LiMn_2O_4$ and that the electrons compensating for the Li^+ ion charge reduce Mn^{3+} to Mn^{2+} in Mn_3O_4 and Mn^{4+} to Mn^{3+} in $Li[Mn_2]O_4$. In $Li_xMn_3O_4$, the tetragonal distortion due to a cooperative Jahn-Teller distortion by octahedral-site Mn^{3+} ions, decreases as x increases as would be expected. The X-ray data also showed that the inserted Li^+ ions occupy the interstitial octahedral sites of the $[Mn_2]O_4$ framework in Mn_3O_4 and that the tetrahedral site Mn^{2+} ions are displaced to the empty interstitial octahedral positions: this indicates an intercalation process similar to that found for Fe_3O_4. The final product is a rocksalt-like structure having a peculiar ordering of the cations.

The electrochemical data for lithium insertion into $LiMn_2O_4$ indicate the existence of a two-phase region [37] as was anticipated because of the first-order character of the cooperative Jahn-Teller distortion [75]. It was found [37] that a cubic phase exists in the range $0 \leqslant x \leqslant 0,1$ and a tetragonal phase in the range $0,85 \leqslant x \leqslant 1,25$. Reaction with lithium in the region $x > 1,25$ appears to destroy the 'spinel' structure leaving unidentified products. X-ray diffraction confirms the existence of both cubic and tetragonal phases in the compositional range $0,1 \leqslant x \leqslant 0,8$. X-ray data again indicated that Li^+ ions are inserted into the octahedral interstitial positions of the $[Mn_2]O_4$ framework, but in this case the tetrahedral site Li^+ ions are not displaced into the octahedral positions. Although unanticipated, this observation is consistent with an insertion in $Li_xFe_3O_4$ to the compositional limit $x \approx 2$. This implies that there is no large discontinuity in the electrostatic barrier to insertion on changing from insertion into octahedral sites to insertion into tetrahedral sites within the framework of the spinel structure.

1.4 THE RELEVANCE OF THE SPINEL AND ROCKSALT STRUCTURES TO SOLID-SOLUTION ELECTRODES

1.4.1 General

The important influence of the structure of the cathode on the reversibility and rate of a chemical reaction in an electrochemical cell has already been stressed in Section 1.3.2. Experiments on solid electrolytes first showed that Na^+ and K^+ ions have their highest mobilities in framework structures, which more easily admit a relatively smooth ionic potential over a continuous path in interstitial space [76]. Unfortunately, the known solid-solution framework structures having a high metallic conductivity contain the heavier, more expensive 4d- or 5d-block framework ions. However, Li^+ ion transport would appear to be faster in close-packed-arrays of large polarizable anions [32]. For example, the well-known layered compound, Li_xTiS_2 accepts Li^+ ions into alternate octahedral-site layers of a close-packed-hexagonal anion array, the charge being neutralized by electrons entering into the 3d bands of the TiS_2 layers [77]. The TiS_2 layers are bound together by Van der Waals forces and become prised apart by the Li^+ ions. The c-axis of Li_xTiS_2 expands by 10 percent for $x = 1$ [38]. In the "close-packed" anion array of Li_xTiS_2, the Li^+-ion mobility is enhanced by the freedom of the crystal to expand along the c-direction. A similar c-axis flexibility and Li^+-ion mobility are found in the analogous layered oxide $Li_{1-y}CoO_2$, which contains lithium ions on alternate octahedral-site layers of the close-packed cubic anion array, the charge-compensating electrons occupying the $Co^{4+}/^{3+}$ ($3d^6$-band) couple of the CoO_2 layers [48]. The preference of the larger alkali ions for trigonal-prismatic versus octahedral coordination prevents Na^+ ion incorporation into close-packed layer structures over analogously large solid-solution ranges [78], which emphasizes the potential importance of Li^+ ions. As a result, interest has been sparked in the possibility of designing 3-dimensional (3D) close-packed-anion structures which will allow the transport of Li^+ ions. Obviously, the Li^+-ion mobilities in any such 3D structures will be hindered by the fact that these structures are volume-constrained, unlike the layered, 2D structures, which are flexible in the c-direction. Since it has been recognized [32,37] that the $[B_2]X_4$ subarray of an $A[B_2]X_4$ cubic spinel may provide such a close-packed-anion, 3-dimensional framework for Li^+ ion transport, a better understanding of the spinel structure is desirable.

1.4.2 The Spinel Structure

The spinel structure-type is derived after the mineral "spinel" with formula $MgAl_2O_4$ [79,80]. The structure of the spinel group of compounds was first investigated by Bragg [81] and Nishikawa [82]. In the ideal cubic spinel structure, with the origin of the unit cell at the centre ($\bar{3}m$), the close-packed anions are located at the 32e positions of the space group $Fd\bar{3}m$. Each unit cell contains 64 tetrahedral interstices situated at three non-equivalent positions 8a, 8b and 48f, and 32 octahedral interstices situated at the crystallographically non-equivalent positions 16c and 16d.

The spinel structure can be symbolized as AB_2X_4, there being eight $[AB_2X_4]$ in the unit cell. The A cations occupy $^1/_8$ of all the available tetrahedral sites, designated the 8a sites, while the B cations occupy $^1/_2$ of the octahedral sites, these being the 16d sites [40,42, 80,83]. The empty 16c sites form an interconnected 3-dimensional array of edge-shared sites, each site sharing edges with six other 16c sites and sharing common faces with two 8a tetrahedral sites. Figure 1.14 depicts a schematic diagram of the spinel structure.

The spinel structure is adopted by numerous compounds in which a wide variety of metal cations may be stabilized on the A and B sites of the cubic close-packed-anion lattice. Examples include such compounds as Co_3O_4, Mn_3O_4, $LiMn_2O_4$ and $CoFe_2O_4$ [80].

In some spinels, however, the A and B cations are arranged differently, half the B cations occupying the interstitial positions usually occupied by the A cations. This is referred to as the 'inverse spinel structure' and can be represented as $B[AB]X_4$ [79,80,84]. Magnetite, Fe_3O_4 adopts the inverse spinel structure, i.e. $Fe^{3+}[Fe^{2+}Fe^{3+}]O_4$. The reason for its high electronic conductivity (σ = 200 ohm^{-1}cm^{-1}) compared to such compounds as Mn_3O_4, which has the normal spinel structure, $Mn^{2+}[Mn_2^{3+}]O_4$, is due to the continuous electron exchange between the Fe^{2+} and Fe^{3+} ions on the octahedral B sites of the spinel structure [85,86].

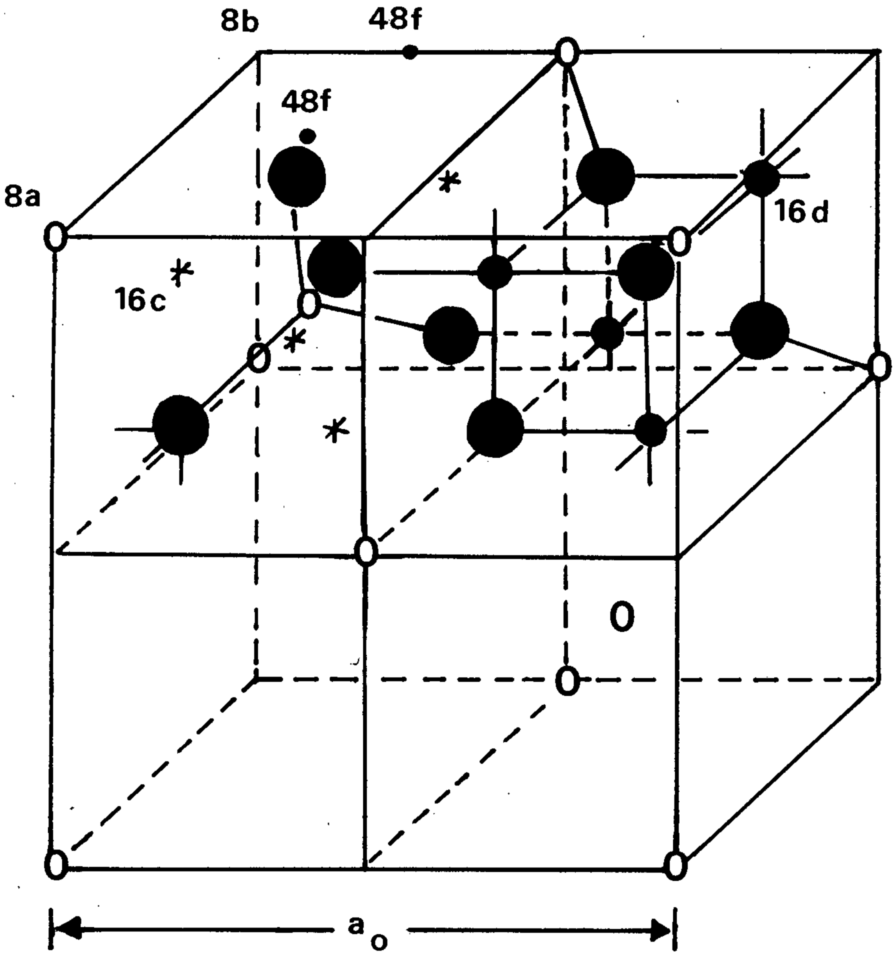

Figure 1.14:
Two quadrants of the cubic $A[B_2]X_4$ spinel, space group $Fd3m(O_h^7)$ [32].

1.4.3 The Rocksalt Structure

The rocksalt structure is also referred to as the sodium chloride structure, since this type of structure occurs in sodium chloride crystals. In the case of rocksalt-type transition metal oxides, such as MnO, CoO, NiO, FeO and TiO, the oxygen ions are arranged in a cubic-close-packed array as in the spinel structure, but all of the octahedral interstitial sites are filled randomly with cations and none of the tetrahedral sites are occupied [40,80,84,87]. Figure 1.15 depicts a schematic diagram of the rocksalt structure.

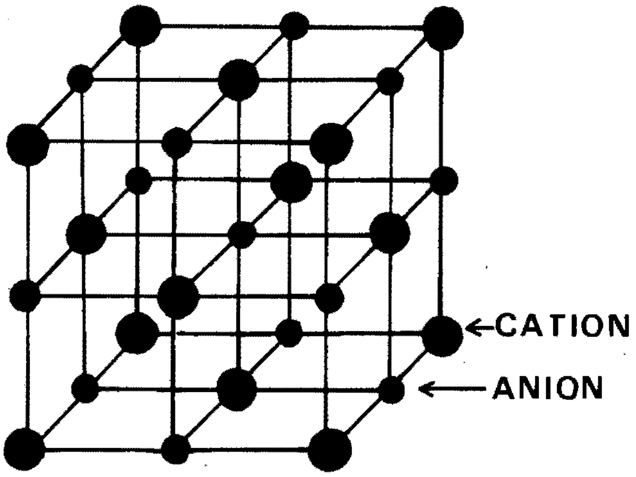

Figure 1.15:
The unit cell of the rock-salt (NaCl) structure [80].

Although the idealized CoO rocksalt structure is normally assigned to space group Fm3m (O_h^5), a = 4,260 Å [88], its structure can be correlated to the spinel structure by regarding the Co^{2+} ions as occupying all the octahedral sites (16c and 16d) of space group Fd3m, the 64 tetrahedral sites remaining empty.

1.4.4 The Correlation Between the Spinel and Rocksalt Structures

An understanding of both the spinel and the rocksalt structures emphasizes the similarities in their structures. The correlation between the two structures is borne out by the insertion of lithium into both Fe_3O_4 and Mn_3O_4, which can accommodate at least one lithium ion per formula unit [32,37].

It has been established that during lithiation of these compounds at room temperature, the $[B_2]X_4$ framework of the spinel structure remains intact. Lithiation of Fe_3O_4 and Mn_3O_4 to form $Li_xFe_3O_4$ and $Li_xMn_3O_4$ respectively results in migration of the 8a-site Fe^{3+} and Mn^{2+} ions into neighbouring empty octahedral sites (16c). The lithium ions occupy the remaining octahedral sites (16c), and at x = 1,0 all the octahedral sites of the cubic-close-packed anion array are occupied, as in rocksalt, but with partial ordering that retains transition metal ions on the 16d sites of the original $[B_2]X_4$ spinel framework.

1.5 COBALT OXIDE - AN ALTERNATIVE CATHODE MATERIAL

Lithium-aluminium/LiCl, KCl/Fe_3O_4 cells have been found to operate reversibly at 420 °C [31] and have shown good electrochemical characteristics in terms of electrode capacity, rechargeability and lifetime. The Fe_3O_4 spinel phase and $LiFeO_2$ rocksalt phase generated during discharge have been shown to be stable in the cell environment. It is therefore of interest to study other spinel and rocksalt systems as cathodes in high temperature lithium batteries. The choice of transition metal must be restricted to the first row of the transition metal series in order to preserve a high specific energy. The cobalt oxide systems Co_3O_4 (spinel) and CoO (rocksalt) satisfy a number of the requirements for such high temperature lithium cells, in particular their attractive theoretical capacities and voltage vs lithium. Moreover, spinels appear to be promising solid-solution electrodes for ambient temperature lithium batteries.

This thesis reports on the electrochemical and structural characterization of Co_3O_4 and CoO electrodes in high temperature cells and of Co_3O_4 electrodes in ambient temperature lithium cells.

CHAPTER 2

EXPERIMENTAL

2.1 INTRODUCTION

This chapter describes the cell designs used for the electrochemical testing of cobalt oxide cathodes at high and ambient temperature. Cell components are also described. A short description of the electrochemical testing procedure is given and various characterization techniques employed are presented.

2.2 HIGH TEMPERATURE ELECTROCHEMICAL CELLS

2.2.1 Cell Design

The cell design used for evaluating the performance of cobalt oxide cathodes at elevated temperatures, was based on a simple two-electrode system. A diagrammatic sketch of the cell assembly is illustrated in Fig. 2.1. The anode consisted of a lithium-aluminium alloy cast into a stainless-steel cup. The cathode material was lightly compacted in a porous (50%) graphite cup. A molybdenum wire attached to the cup served as the electrical feed to the external circuit. The anode and cathode were separated by several layers of finely woven ZrO_2 and BN cloth which acted as particle retainer for the anode and insulator respectively. The cell assembly was immersed in a dry eutectic melt of LiCl, KCl (42 mol% KCl, 58 mol% LiCl) and contained in a highly dense α-Al_2O_3 jacket (supplied by Thermal Syndicate) and hermetically sealed under argon. Cells were operated at 420 ^{o}C.

2.2.2 Cathodes

Cells were loaded in the charged state and also in the fully discharged state. In the former case cathodes consisted of a powdered mixture of the appropriate cobalt oxide (Cerac, -325 mesh, purity >99,5%) and graphite (to enhance the conductivity of the cathode), lightly compacted in a porous graphite cup. In the latter case, the graphite cup contained an intimate mixture of finely divided cobalt metal (Cerac, -325 mesh, purity >99,5%), Li_2O (Cerac, -100 mesh, purity 99%) and graphite powder. In an attempt to improve the performance of the cells, cells were also assembled with an excess of Li_2O in the cathode. A series of cells having cathodes consisting of Co metal and Li_2O in different proportions, and graphite, were also investigated.

2.2.3 The Anode

The anode consisted of a lithium-aluminium alloy containing approximately 30 a/o lithium (m.p. of Li is 180,54 °C and the m.p. of Al is 660,37 °C [89]) cast into a stainless steel cup at 900 °C (m.p. of the alloy is 720 °C [90]). The electromotive force (e.m.f.) of these alloys has been found to be independent of the composition of the alloy over a range from 7 a/o to 47 a/o lithium, but varies with temperature, T(K) according to the equation:

$$E(mV) = 451,07 - 0,2202T$$ [91]

At 420 °C the lithium-aluminium alloy functions at a voltage 0,30 V less than pure lithium.

2.2.4 The Electrolyte

The electrolyte was a dry eutectic mixture of LiCl (58 mol%) and KCl (42 mol%). Melting point determinations of the LiCl, KCl eutectic were carried out on a Gallenkamp Micro Melting Point Apparatus MF-350. The melting point was found to be 352 °C which is in agreement with the literature value [92].

2.2.5 Graphite Cups

Porous graphite cups were used to contain the cathode material and graphite powder. The surface area of the base of the cup was 10,7 cm^2. The molybdenum feed was secured to the lid and the cup inverted as illustrated in Figure 2.1.

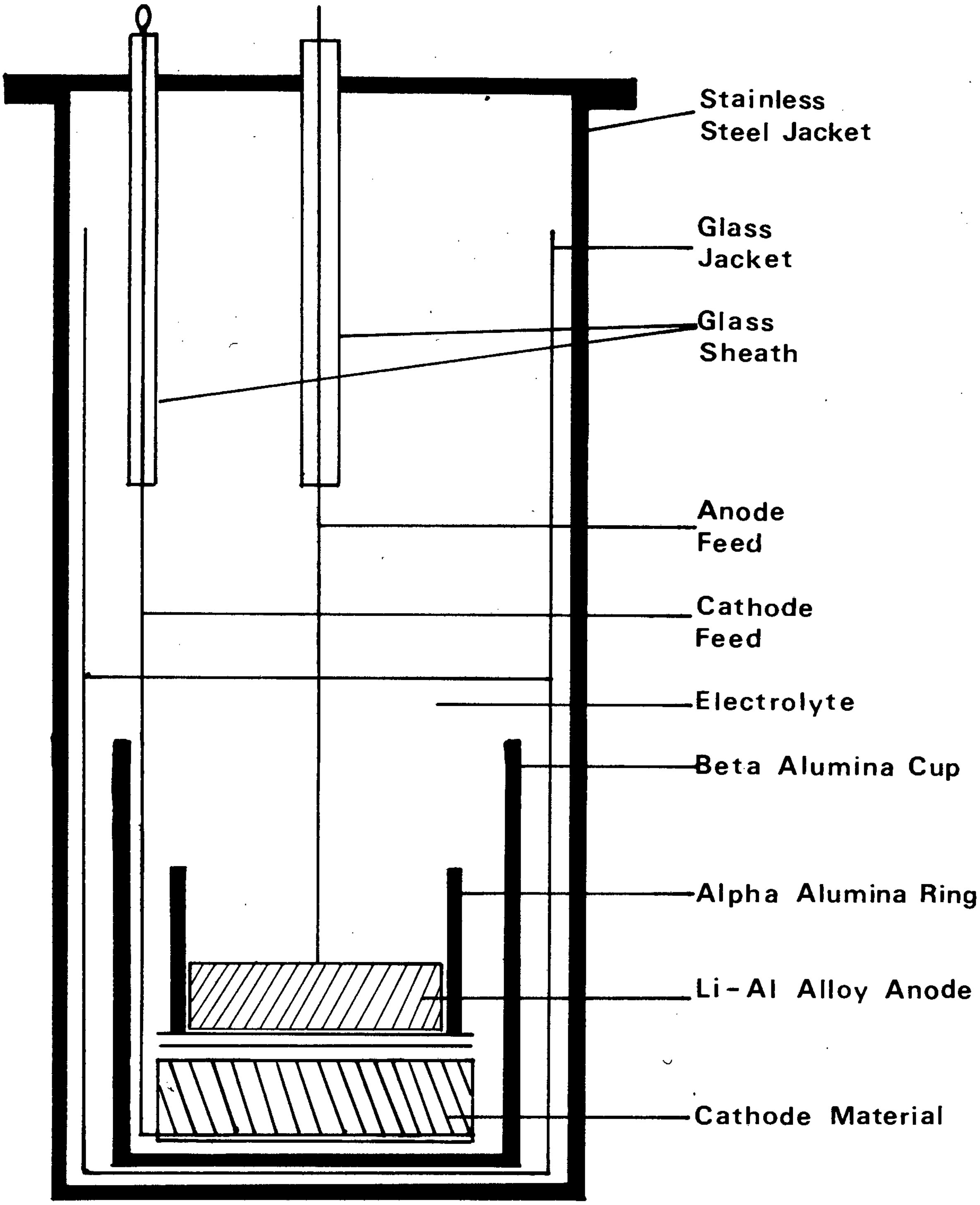

Figure 2.1:
A typical test cell

A good porosity of the graphite cups was necessary:

a) to ensure good access of the electrolyte to the active cathode material and
b) to minimize the internal resistance of the cell.

However, as some difficulty was experienced in achieving 100% wetting of the oxide particles by the molten electrolyte, an attempt was made to increase the porosity of the cups by heat-treatment at 600 °C in air for 2 hours, prior to use. Careful control of heating times was necessary; too long a heating time resulted in mechanically weak structures.

2.2.6 Separators

The cells assembled for this investigation employed a separator consisting of coarsely woven BN (Boron nitride) felt ± 2 mm thick (Carborundum Co.) together with zirconium oxide felt (Zircar Products Inc., type ZYW 30A).

2.2.7 The Cathode Current Collector

A strand of molybdenum wire (0,5 mm diameter) served as the current collector for the cathode (see Figure 2.1). The upper section of the wire was surrounded by a glass sheath to which it was secured with an epoxy glue. This enabled a seal to be effected where the wire passed through the lid of the steel jacket which housed the cell.

2.2.8 The Anode Current Collector

A stainless steel rod screwed into the base of the stainless steel cup containing the lithium-aluminium alloy, served as the electrical feed for the anode (see Figure 2.1). A glass sheath was secured to the stainless steel rod with epoxy glue in a similar fashion to that on the molybdenum wire, thereby effectively sealing the cell from the outside atmosphere.

The components of a typical cell can be seen in the photograph in Figure 2.2.

Figure 2.2:
Components of a typical high temperature lithium/cobalt oxide cell.

2.2.9 Cell Operation

Each cell was connected to a Philips PE 1535 DC power supply and was charged and discharged at current densities between 2 and 5 mA cm^{-2} as measured relative to the surface area of the graphite cup. The charge and discharge characteristics were monitored continuously on a single pen chart recorder on which the cell voltage was recorded as a function of time. Voltage measurements were made under load and also on open circuit by interrupting the charge/discharge cycles at intermittent periods and allowing the system to equilibrate for up to half an hour.

A typical test cell under operation is depicted in Figure 2.3.

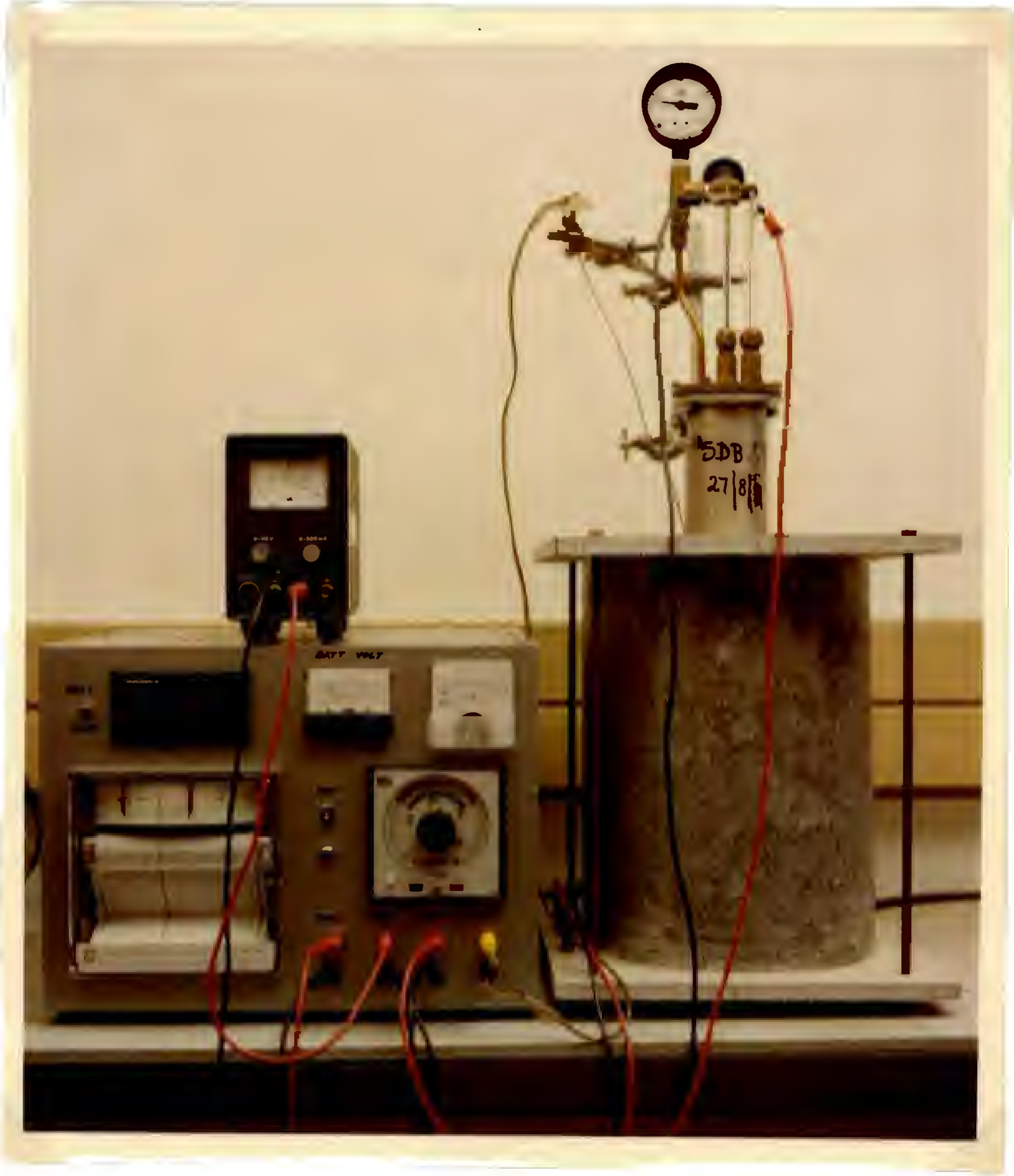

Figure 2.3:
A typical high temperature test cell under operation.

2.3 AMBIENT TEMPERATURE ELECTROCHEMICAL CELLS

2.3.1 Cell Design

The cell design used for evaluating the performance of cobalt oxide cathodes at room temperature, was based on a simple two-electrode system of the following form:

Li/1M $LiBF_4$ solution in propylene carbonate/Co_3O_4

A diagrammatic sketch of the cell assembly is illustrated in Figure 2.4.

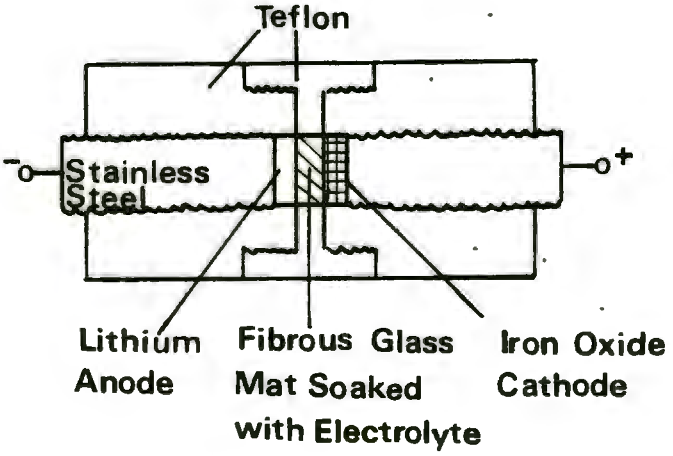

Figure 2.4:
A typical test cell.

The anode consisted of a small disc of lithium metal. The cathode consisted of ~ 50 mg Co_3O_4 powder (Cerac, -325 mesh, purity >99,5%) compacted at 5 kg/cm^2 onto a fine, stainless-steel, gauze disc 1 cm in diameter. Four layers of a fibrous glass mat served as both separator for the electrodes and as retainer for the electrolyte. Cells were assembled and discharged under argon in a glovebox.

2.3.2 Cell Operation

Cells were discharged at constant current (~ 20 µA) using a Princeton Applied Research (PAR) 173 Model D potentiostat/galvanostat. The discharge characteristics were monitored continuously on a single pen chart recorder on which the cell voltage was recorded as a function of time. Open-circuit voltages were recorded at intermittent periods during discharge. Each open-circuit reading was taken after the cell had equilibrated for up to 120 hours.

2.4 CHEMICAL LITHIATION OF COBALT OXIDE AT AMBIENT TEMPERATURE

Samples of Co_3O_4 were lithiated chemically to verify the structural characteristics of lithiated Co_3O_4 samples prepared electrochemically. The advantages of chemical lithiation are that it is fast and bulk samples can be prepared, compared to the very slow electrochemical methods that use only small amounts of material.

2.4.1 Method of Chemical Lithiation

All chemical reactions of Co_3O_4 (Cerac, -325 mesh, >99,5%) using n-butyllithium (Alfa Products, 15 w/o solution in hexane) as lithiating agent, were performed under a nitrogen atmosphere. An excess of n-butyllithium, calculated on the basis of 1,2, 1,7 and 2,0 moles of lithium per mole of Co_3O_4 respectively, was injected into each of three reaction flasks that typically contained 0,5 g Co_3O_4 in 30 ml of dry hexane. Each flask was continuously stirred at 50 °C for 24 hours. This procedure was then repeated, this time stirring each flask continuously at 50 °C for 48 hours. Finally, an excess of n-butyllithium, calculated on the basis of 3,5 moles of lithium per mole of Co_3O_4, was injected into a reaction flask containing 0,5 g Co_3O_4 in 30 ml of dry hexane. The contents of this flask were continuously stirred at 50 °C for 4 days and 19 hours (115 hours).

After reaction, the products were thoroughly washed with hexane to remove the excess n-butyllithium and finally vacuum-dried and stored under argon.

2.4.2 Chemical Analysis of Lithiated Cobalt Oxide

The lithium contents of the $Li_xCo_3O_4$ samples were determined using atomic-absorption methods by Mr H Lachmann at the National Chemical Research Laboratory of the CSIR.

2.5 STRUCTURAL ANALYSIS OF SAMPLES

Identification of the various phases generated at the cathode, at high temperature and ambient temperature during charge and discharge, was done by powder X-ray diffraction (XRD) methods at room temperature, using either a Philips PW 1050 diffractometer with a quartz analysing monochromator, or an automated Rigaku Powder Diffractometer. CuKα ($\bar{\lambda}$ = 1,54178 Å) radiation was used. Peak positions were measured against an internal silicon standard. Structural analyses of the chemically lithiated Co_3O_4 samples were obtained in the same way.

Cathode samples from the high temperature cells were loaded in a glovebox under mylar foil, which provided an airtight seal. These samples were analysed in an unwashed state and were also analysed after being washed with water to eliminate the LiCl, KCl electrolyte peaks which tended to dominate the X-ray patterns.

Samples of lithiated Co_3O_4 prepared electrochemically and chemically at ambient temperature were also loaded in a glovebox, but were sprayed with a layer of plastic (Plastik-Spray 70) to exclude air. This spray gave rise to increased background scattering on the X-ray diffraction spectra, particularly at low 2θ values. However, a few of the diffraction spectra of chemically lithiated samples were also collected in air.

CHAPTER 3

THE ELECTROCHEMICAL PERFORMANCE OF HIGH TEMPERATURE LITHIUM/COBALT OXIDE CELLS

3.1 INTRODUCTION

At the beginning of this chapter, the electrochemical performance of the various cell components is described and discussed. This is followed by a section concerning the nature of the discharge curves for the high temperature cells. Much information regarding the reaction mechanism occurring at an electrode, can be gathered from the nature of the discharge curve of an electrochemical cell. Plots of the equilibrium voltage versus composition give rise to either a voltage plateau, which indicates a multiphase reaction, or a continuous drop in voltage, which indicates a single-phase reaction. The Gibbs Phase Rule and Nernst Equation are used to explain why a multiphase reaction yields a voltage plateau, while a single-phase reaction gives rise to a voltage drop. This is followed by descriptions and discussions of the discharge curves for the various lithium/cobalt oxide cells investigated. Finally, a section regarding the theory of overpotential and relating it to the high temperature cells, is included.

3.2 CELL COMPONENTS

3.2.1 The Lithium-Aluminium Alloy Anode

The need for an element of low atomic weight and low electronegativity for use as the anode in high energy density, high power density battery systems, has already been mentioned in Section 1.2. Lithium metal electrodes satisfy both these requirements [90,91]. Unfortunately, it is the high electrochemical reactivity of lithium and its relatively low melting point (180,54 °C) [89] that result in corrosion problems in high temperature cells and difficulty in containment of the lithium when used as an electrode [90,91,93]. In order to reduce these problems, solid alloys of lithium, such as the lithium-aluminium alloy, have been investigated and good electrochemical performance of lithium-aluminium alloys (composition range 17-69 a/o Li) has been reported [91,94,95]. However, alloying the lithium reduces the theoretical specific energy of a cell, because of the reduced activity of the lithium in the alloy and the added weight of the alloying metal [96].

Studies [97] of aluminium-rich alloys have shown that a solid solution of lithium in aluminium was formed up to 7,1 a/o lithium at 300 °C and up to 8,5 a/o lithium at 400 °C. This phase is known as the α-phase and it has been confirmed by quantitative metallography and lattice parameter measurements [98]. As the lithium concentration is increased at these temperatures, two phases are formed, the α-phase and β-phase, where the β-phase consists of β-LiAl [7,93,98]. The phase diagram of the lithium-aluminium alloy system is depicted in Figure 3.1. The two phase region extends to approximately 45,8 a/o lithium, this value being constant over the temperature range 150-550 °C. Yao et al. [91] in their studies, found that constant potential was indicated by the alloy up to 46,97 a/o lithium, which implies that a constant lithium activity exists on the alloy surface over the composition range from 6,91 to 46,97 a/o lithium in aluminium.

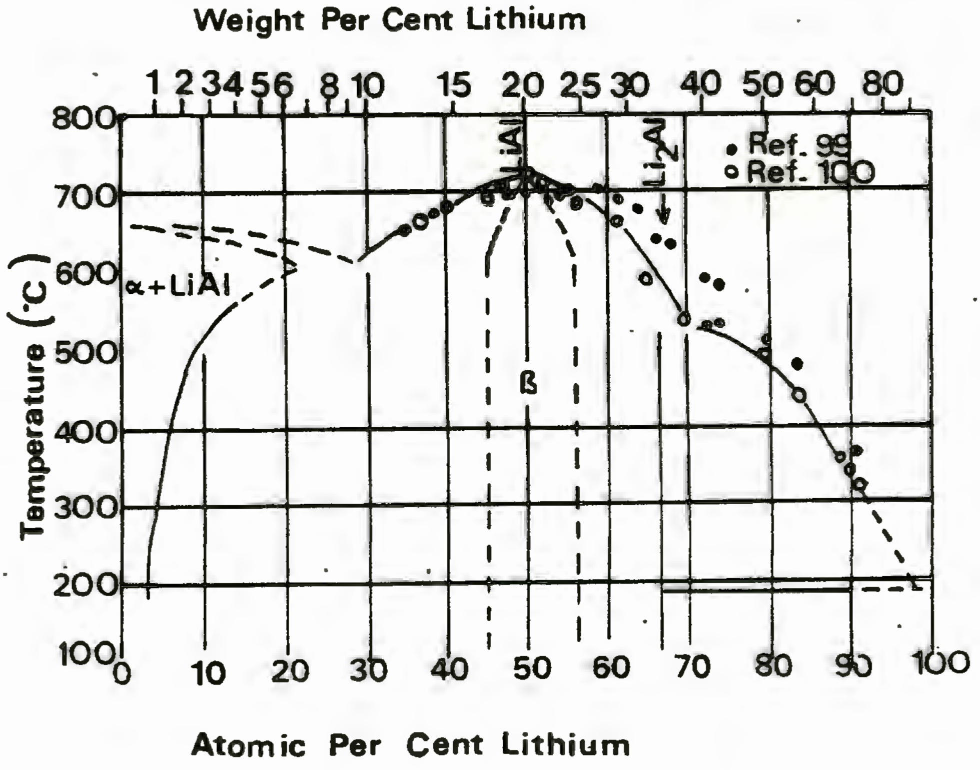

Figure 3.1:
Phase diagram of lithium-aluminium system.

In these studies the lithium-aluminium alloy anode was used as the reference electrode during current-voltage readings for polarization assessment and for the measurement of O.C.V. values. Although lithium-aluminium alloys are reported to exhibit good electrochemical behaviour [91,94,95,101] and to be able to hold a current density of 150 mA/cm^2 without showing any significant polarization [91], the fact that the composition of these alloys changes during cell cycling enhances concentration overpotential effects.

Lithium anodes are seriously hindered by dendritic deposition of lithium during cell charging which results in electrical short circuits [90,93]. It has been hypothesized [93] that freshly deposited lithium is highly active, reacting with most solvents and associated impurities in the cells. The use of lithium-aluminium alloys would obviously alleviate this problem to some degree since the lithium activity is reduced by alloying. Unfortunately, dendrite formation is still a serious problem even when lithium-aluminium alloy anodes are employed and often leads to cell failure due to electrical short circuiting.

Another serious problem encountered with lithium-aluminium alloys is that of volume changes during cell cycling [24]. These alloys are reported to increase in volume during charging [91] with the result that the alloy structure becomes increasingly porous. In this study, the lithium-aluminium alloys were found to undergo excessive volume changes in some cases, especially after long periods of cell cycling. This often led to electrical short circuits resulting in cell failure. Photographs of two anodes which suffered serious swelling during cell operation are depicted in Figures 3.2 and 3.3. Figure 3.3 shows an anode which swelled in only one part of the alloy. This localised swelling was evident in a number of the anodes.

Dendrite formation and large volume increases in the lithium-aluminium anode impose severe limitations on the cell cycle life and the anode was found to be one of the limiting factors in these high temperature lithium/cobalt oxide cells. Gay et al. [90], in their studies of

Figure 3.2:
Lithium-aluminium alloy anode showing serious volume increase after successive cycling of a high temperature lithium/cobalt oxide cell.

lithium-aluminium alloy electrodes, also found that these electrodes were limiting at high discharge rates. This appears to be the case in the cells studied in this investigation and lithium-aluminium electrode alloys will certainly have to undergo further development before they meet all the requirements of high energy density batteries.

3.2.2 The Electrolyte

Since the largest contribution to the internal resistance of an electrochemical cell is usually made by the electrolyte, the use of fused-salt electrolytes instead of aqueous electrolytes or organic solvent

Figure 3.3:

Lithium-aluminium alloy anode exhibiting localized swelling after undergoing a long period of cycling in a lithium/cobalt oxide cell.

electrolytes, would greatly reduce the internal resistance of a cell [1,12,13]. This is due to the fact that fused-salt electrolytes have far lower resistivities than aqueous or organic electrolytes [1,13,102]. The conductivities of various electrolytes are compared in Table 3.1. Unfortunately, most molten lithium halide salts have high melting points, but this can be reduced by forming eutectic salts [14], for example with KCl, such as the LiCl, KCl eutectic used in this study. A diagram of melting point versus composition for the LiCl, KCl eutectic system is depicted in Fig. 3.4. The eutectic mixture at 58 mol% LiCl, 42 mol% KCl melts at 352 °C.

TABLE 3.1:

Electrical conductivity (σ) of various electrolytes

LIQUIDS						
(i) Aqueous		t(°C)	σ(Ω^{-1}cm^{-1})	(ii) Molten	t(°C)	σ(Ω^{-1}cm^{-1})
H_2SO_4	(~ 3,75 M)	20	0,76	LiCl	637	5,86
NaCl	(~ 7,5 M)	20	0,23	NaCl	807	3,60
KCl	(1 M)	20	0,10	KCl	787	2,20

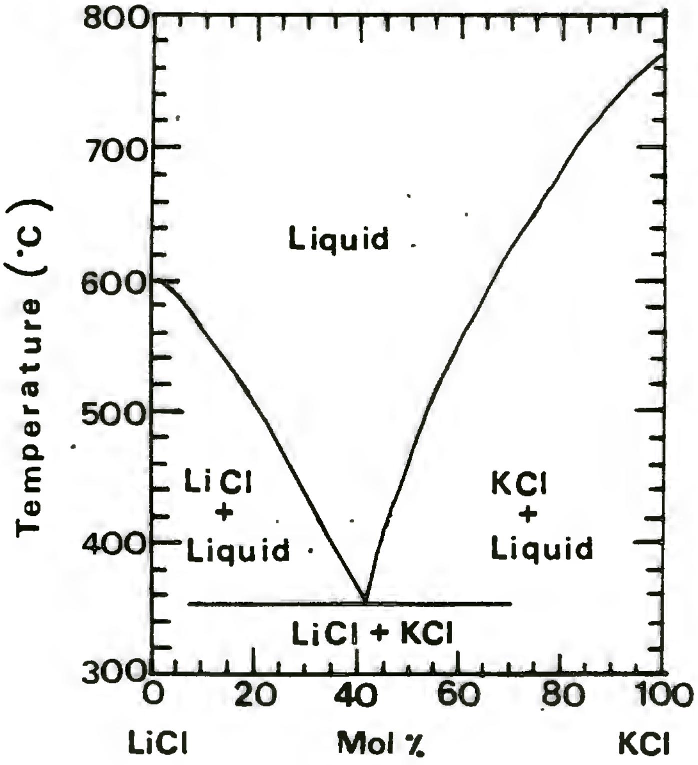

Figure 3.4:

Melting point versus composition (mol%) for the LiCl. KCl system.

Operation of the cell at elevated temperatures, necessitated by the use of fused salts, does have the advantage of increasing the exchange-current densities (rates of the electrode reactions) [1,12], but otherwise these high temperatures result in a number of problems, the worst being material and seal degradation [1,13]. Other problems encountered with fused salt batteries include:

i) immobilization of the constituents
ii) structural and volume changes on cycling
iii) self-discharge
iv) container corrosion
v) provision of adequate insulation for high temperature maintenance.

3.2.3 The Stability of Molybdenum in the LiCl, KCl Eutectic Electrolyte

Chlorination of the molybdenum wire used as the electrical contact from the cathode to the positive terminal of the cell, was prevalent in many of the high temperature cells and often resulted in cell failure, particularly during the charge cycle if the charging voltage reached ~ 2,8 V. The decomposition voltage of the LiCl, KCl eutectic with respect to molybdenum was therefore determined. Using a molybdenum/lithium-aluminium alloy couple, the decomposition voltage of the eutectic with respect to molybdenum was found to be approximately 2,8 V. The plot of current (mA) versus voltage (V) for the determination of this decomposition potential is depicted in Figure 3.5.

At high voltages molybdenum reacts with the eutectic to form molybdenum chloride, which leads to corrosion of the molybdenum wire. The value quoted for the Li^+/Mo (chloride) reaction at 298 K by Gibson and Sudworth [104] is 3,19 V, the reaction being:

$$2LiCl + Mo \rightleftharpoons 2\,Li + MoCl_2 \qquad (3.1)$$

Taking into account the voltage drop due to the increase in temperature ($\Delta T = 395$ K) and the fact that the lithium-aluminium alloy functions at a voltage 0,30 V less than pure lithium, the theoretical E°

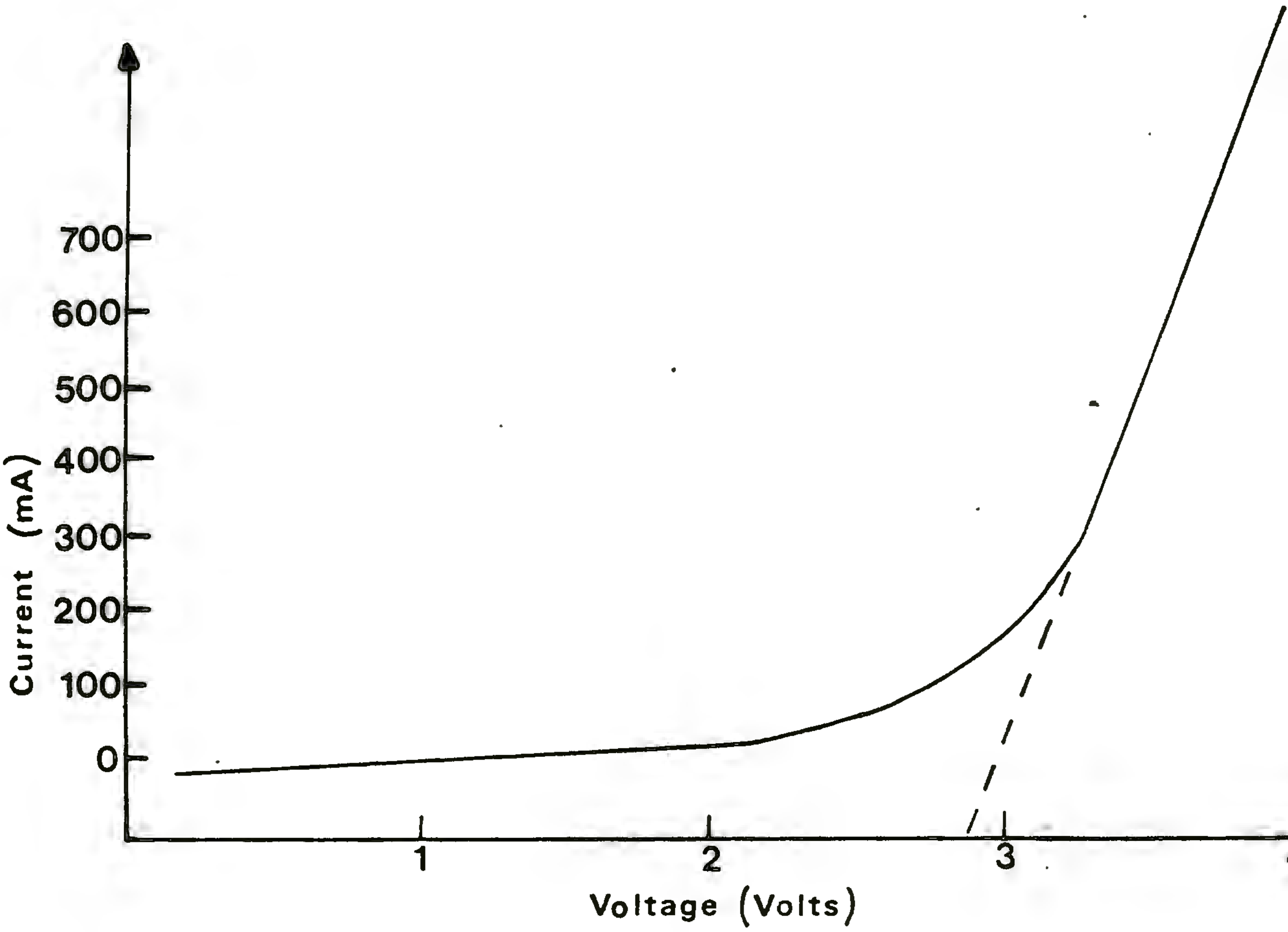

Figure 3.5:

Plot of current (mA) versus voltage (V) for determination of the decomposition potential of LiCl,KCl eutectic with respect to molybdenum.

value for the formation of molybdenum chloride in the cell environment was calculated to be 2,81 V. This is in very good agreement with the experimentally determined decomposition voltage of 2,8 V. Subsequently, cells were not charged above a limit of approximately 2,2 V and no further serious problems with the molybdenum wire were encountered.

In the high temperature cells investigated in this study, electrochemical attack of the molybdenum wire usually occurred at, or near the surface of the LiCl, KCl eutectic and was obviously due to a reaction between the electrolyte and the molybdenum. Figures 3.6 and 3.7 depict corroded ends of the molybdenum wires which were employed in high temperature lithium/cobalt oxide cells.

As a result of the high cost and low availability of molybdenum, alternative electronically conducting materials for these high temperature cells will have to be found.

Figure 3.6:
Photograph of corroded end of a molybdenum wire used in a high temperature lithium/cobalt oxide cell (magnified 1000x)

3.2.4 Separators

An electrode separator must meet a number of requirements in order to ensure successful operation of the cell. The most important functions of the separator are to provide electrical isolation of the electrodes from each other while at the same time containing sufficient electro-

Figure 3.7:

Photograph of corroded end of a molybdenum wire used in a high temperature lithium/cobalt oxide cell (magnified 1000x)

lyte to allow good ionic conduction between the electrodes. A separator should also retain the active materials within their respective electrodes, be chemically stable in the cell environment at the operating temperature, be thin enough to permit close electrode spacing, be flexible and mechanically strong enough to sustain the dimensional changes that occur during cell cycling and be easily wet by the electrolyte [105,106,107].

On account of its high oxidation potential and reactivity, lithium causes serious materials problems. It reacts with virtually every known ceramic separator. Boron nitride cloth has so far proved to be one of the very few materials that is not only fairly stable to attack by lithium, but also satisfies most of the above requirements [14,105, 106]. However, the fabric weave presently attainable in BN cloth is not sufficiently robust to completely retain the active materials within the electrodes and this has led to the use of a thin layer of zirconium oxide fabric, which has a tighter weave, in conjunction with the BN separator. ZrO_2, however, is weakly electronically conductive in the cell environment and therefore this material can only be used as a particle retainer and not as an electrode separator [105].

BN has proved to be a very effective separator, but due to its high cost, an alternative, less costly material will have to be found before mass production of reasonably priced cells is feasible.

3.3 DISCHARGE CURVES FOR HIGH TEMPERATURE LITHIUM/COBALT OXIDE CELLS

3.3.1 General

Open-circuit-voltage plots were characterized by several voltage plateaus that were clearly distinguishable from each other during charge, but not always during discharge. The fact that a voltage plateau exists, indicates that the reaction occurring is a multiphase reaction. This becomes obvious if the following hypothetical multiphase reaction of a divalent transition metal oxide is considered:

$$2Li + MO \longrightarrow M + Li_2O \qquad (3.2)$$

During discharge there are three distinct phases in the cathode, namely MO, M and Li_2O. The Gibbs Phase Rule states [89,108,109] that:

$$F = C - P + 2 \qquad (3.3)$$

where F = number of degrees of freedom for the system to be in equilibrium

C = number of components to define each and every phase

P = number of phases

For the above reaction:

$C = 3$ (i.e. M, Li and O)
$P = 3$ (i.e. MO, M and Li_2O)

Therefore $F = 2$.

The two degrees of freedom which must be defined for the system to be in equilibrium are temperature and pressure. Under these conditions the composition of the various phases in the cathode is constant, i.e. all phases are at unit activity, i.e.

$$\frac{[MO]}{[M]} = \frac{1}{1} \qquad (3.4)$$

The Nernst Equation for the potential of an electrode [110] states that:

$$E_{el} = E^{o}_{el} - \frac{RT}{nF} \ln \frac{[OX]}{[RED]} \qquad (3.5)$$

where E_{el} = electrode potential
E^{o} = standard oxidation potential of the electrode
$[OX]$ = concentration of the oxidized species i.e. MO
$[RED]$ = concentration of the reduced species i.e. M

Therefore, when:

$$\frac{[MO]}{[M]} = \frac{1}{1}$$

then:

$$\frac{RT}{nF} \ln \frac{[MO]}{[M]} = 0$$

and thus:

$$E_{el} = E^{o}$$

This means that since the lithium anode also operates as a constant voltage electrode the system remains in equilibrium independent of the concentration of the oxidized and the reduced species in the cathode, or in other words, independent of the composition of the electrodes and this gives rise to a voltage plateau.

On the other hand, a single-phase insertion process is characterized by a drop in voltage with changing composition. For example, consider the following insertion reaction:

$$xLi + Co_3O_4 \longrightarrow Li_xCo_3O_4 \quad \text{(single-phase)} \qquad (3.6)$$

As lithium enters Co_3O_4, the Co^{III} to Co^{II} ratio changes. In other words, the ratio of the concentration of the oxidized species to the concentration of the reduced species, changes. Therefore, in the Nernst Equation, the value of E_{el} drops constantly as lithium enters the structure. From a thermodynamic viewpoint, the number of degrees of freedom that must be defined for the system to remain in thermodynamic equilibrium according to the Gibbs Phase Rule (Eqn. 3.3), is three since:

$$C = 2 \qquad (Li + Co_3O_4)$$
$$P = 1$$

i.e. the composition must be defined as well as the temperature and pressure.

It is obvious that for practical applications, a multiphase electrode process would be preferable to a single-phase electrode process, since a cell which delivers a constant voltage is desirable for most applications.

3.3.2 Discharge Curve for a High Temperature Lithium/Co_3O_4 Cell

A typical open-circuit voltage (OCV) plot as a function of the state of charge obtained from a Li-Al/LiCl, KCl/Co_3O_4 cell is illustrated in Figure 3.8.

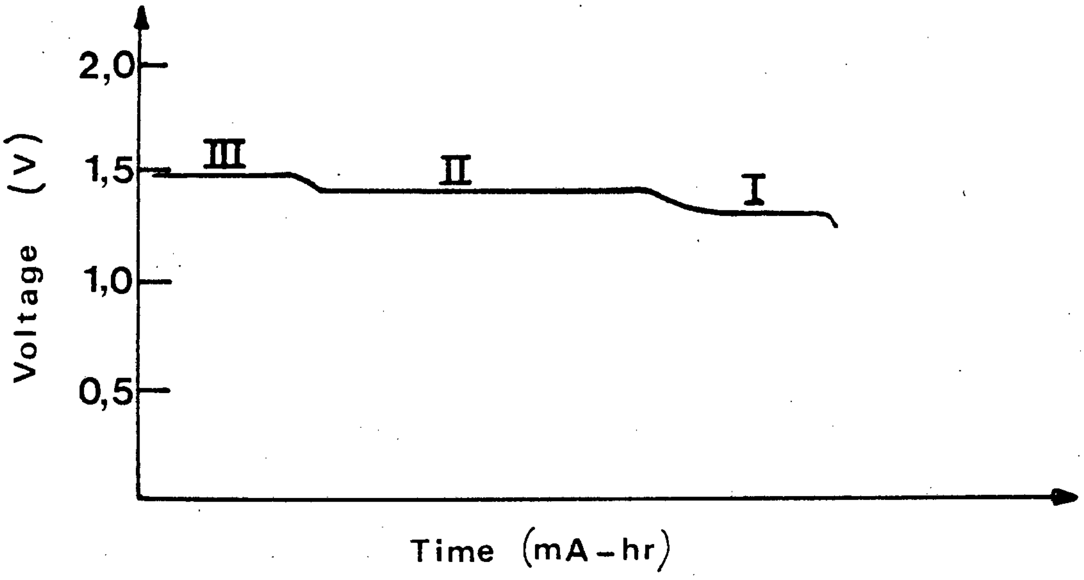

Figure 3.8:
OCV plot as a function of the state of charge for a
Li-Al/LiCl,KCl/Co_3O_4 cell at 420 °C

Plateau III, having an E_0 value of 1,47 V, was only present in the first few cycles, after which it completely disappeared. Plateau II (E_0 = 1,41 V) was the dominant plateau during cycling of this type of cell. Plateau I (E_0 = 1,31 V), which was not always well defined, was short and generally contributed less than 10% to the maximum capacity obtained from any one cell. In some cases where cells were overcharged, evidence of a plateau existing at 2,03 V was found and this was ascribed to the chlorination of cobalt. For the reaction:

$$Co + 2LiCl \longrightarrow CoCl_2 + 2Li \text{ (alloyed with Al)} \qquad (3.7)$$

the theoretical voltage calculated from the electrochemical data [104] is 2,185 V which is in fairly good agreement with the value obtained for this plateau.

The theoretical capacity calculated from the electrochemical data [104] for the following reduction:

$$Co_3O_4 \longrightarrow Co \qquad (3.8)$$

is 884,86 mA-hr/g. The maximum discharge capacity obtained from a LiAl/LiCl,KCl/Co_3O_4 cell was 546 mA-hr/g which is 62% of the theoretical capacity.

3.3.3 Discharge Curve for a High Temperature Lithium/Co_3O_4,Li_2O Cell

In an attempt to improve the discharge capacities obtained from Li-Al/LiCl,KCl,/Co_3O_4 cells, an excess of Li_2O was added to some of the Co_3O_4 cathodes. A typical open-circuit voltage (OCV) plot as a function of the state of charge obtained from one of these cells is depicted in Figure 3.9.

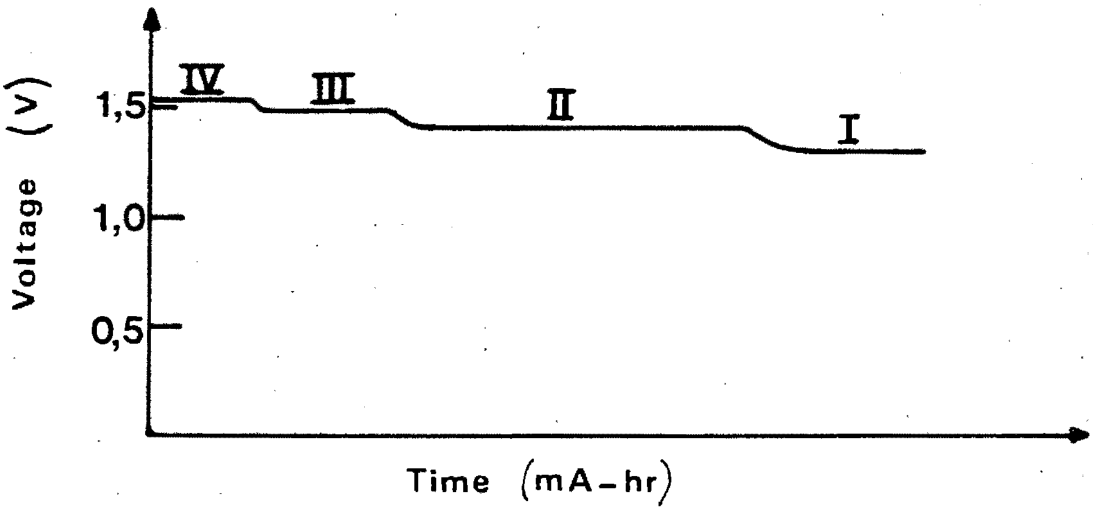

Figure 3.9:
OCV plot as a function of the state of charge for a Li-Al/LiCl,KCl/Co_3O_4,Li_2O cell at 420 °C

Plateau IV having an E_0 value of 1,53 V, was only present when a Co_3O_4 cathode, to which excess Li_2O had been added, was initially subjected to a charge cycle. This plateau disappeared rapidly with successive cycling. Plateau III (E_0 = 1,47 V) only appeared in the first few cycles and it too disappeared with successive cycling. After the initial few cycles, the Co_3O_4 cathodes with excess Li_2O behaved in a similar manner to Co_3O_4 cathodes. Plateau II (E_0 = 1,41 V) became the dominant plateau and plateau III (E_0 = 1,31 V) was not always well defined and generally contributed less than 10% to the maximum capacity achieved by any one cell. Over-charging of these cells also gave rise to a chlorination plateau at 2,03 V.

Surprisingly, the maximum discharge capacity obtained from a Li-Al/LiCl,KCl/Co_3O_4,Li_2O cell was only 42% of the theoretical capacity compared to 62% obtained from a Li-Al/LiCl,KCl/Co_3O_4 cell.

3.3.4 Discharge Curve for a High Temperature Lithium/CoO Cell

Li-Al/LiCl,KCl/CoO cells exhibited similar electrochemical behaviour to a Li-Al/LiCl,KCl/Co_3O_4 cell which had undergone successive cycling. A typical OCV plot as a function of the state of charge obtained from a Li-Al/LiCl,KCl/CoO cell is depicted in Figure 3.10.

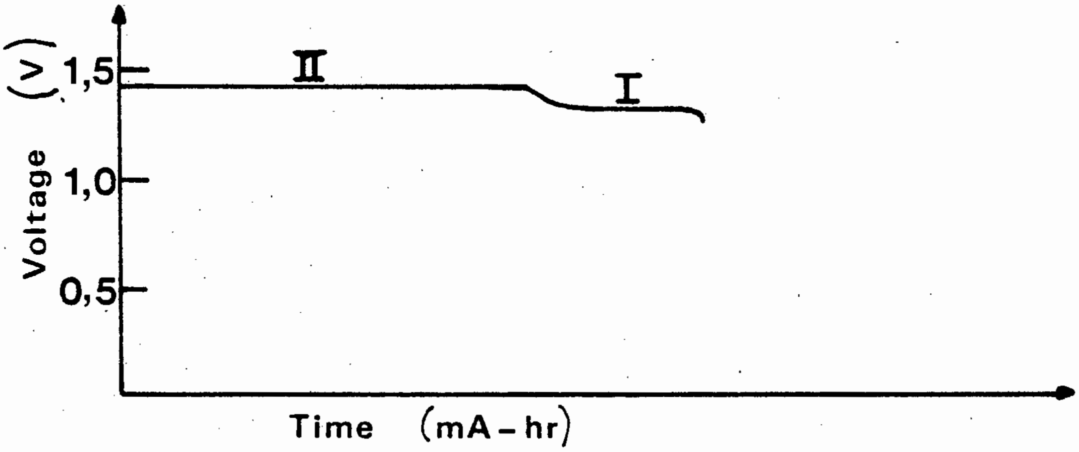

Figure 3.10:

OCV plot as a function of the state of charge for a Li-Al/LiCl,KCl/CoO cell at 420 °C

No evidence of Plateaus III and IV were found and Plateau II (E_0 = 1,41 V) was the dominant plateau. In this case too, Plateau I (E_0 = 1,31 V) was short and not always well defined, generally contributing less than 10% to the maximum capacity obtained from a cell. The plateau due to chlorination was again evident in cells which were overcharged.

The theoretical capacity of a CoO electrode calculated from the electrochemical data [104] for the following reaction:

$$2Li + CoO \longrightarrow Co + Li_2O \qquad (3.9)$$

is 710,88 mA-hr/g. Poor discharge capacities were obtained from Li-Al/LiCl,KCl/CoO cells, 36% of the theoretical capacity being the maximum obtained from this type of cell.

3.3.5 Discharge Curve for a High Temperature Lithium/CoO,Li_2O Cell

As in the case of the Co_3O_4 cathodes, an excess of Li_2O was added to some of the CoO cathodes in an attempt to improve the discharge capacities obtained from them. Li-Al/LiCl,KCl/CoO,Li_2O cells exhibited similar electrochemical behaviour to Li-Al/LiCl,KCl/Co_3O_4,Li_2O cells and a typical O.C.V. plot as a function of the state of charge is depicted in Figure 3.11.

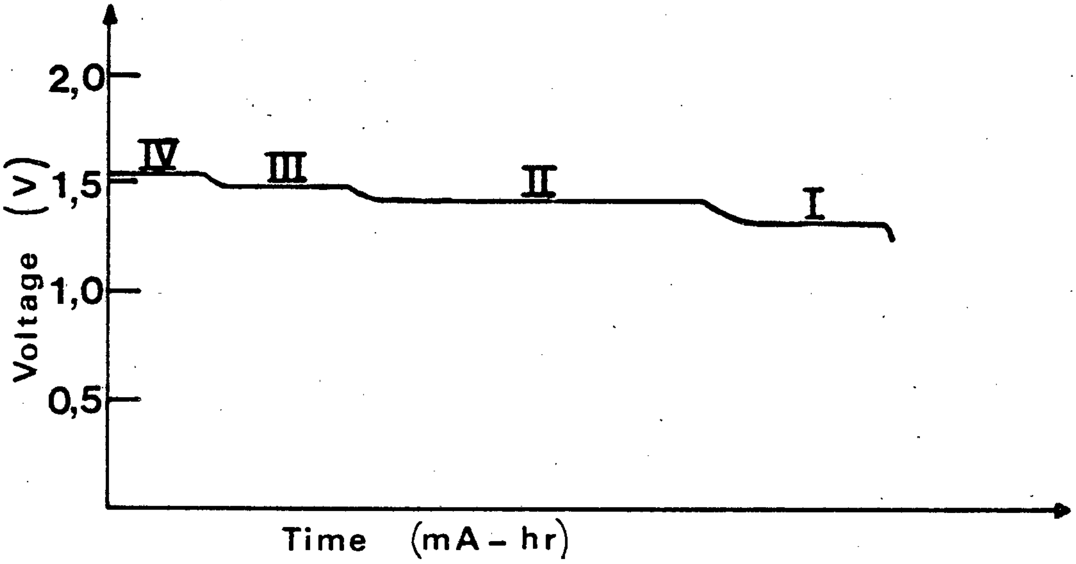

Figure 3.11:
O.C.V. plot as a function of the state of charge for a Li-Al/LiCl,KCl/CoO,Li_2O cell at 420 °C

Plateau III (E_0 = 1,47 V) and plateau IV (E_0 = 1,52 V) were present when a Li-Al/LiCl,KCl/CoO,Li_2O cell was initially subjected to a charge cycle. As with the Li-Al/LiCl,KCl/Co_3O_4,Li_2O cells these plateaus both disappeared with successive cycling. Thereafter, these cathodes behaved in a similar manner to the other cathodes investigated: plateau II (E_0 = 1,41 V) predominated, while plateau I (E_0 = 1,32 V) tended to be very short, contributing less than 10% of the maximum capacity achieved by any of these cells. A plateau at 2,03 V was also evident in the discharge curves of those cells which had been over-charged.

Addition of excess Li_2O to CoO cathodes significantly improved the discharge capacities of these cells. Using the theoretical capacity calculated for the reduction of a CoO electrode to Co as in equation 3.9, the maximum discharge capacity obtained from a Li-Al/LiCl,KCl/CoO,Li_2O cell was 63% of the theoretical capacity. This is a vast improvement on the 36% obtained from Li-Al/LiCl,KCl/CoO cells.

3.3.6 Discharge Curve for a High Temperature Lithium/Co,Li_2O Cell

High temperature Li-Al/LiCl,KCl/Co,Li_2O cells were found to exhibit similar electrochemical behaviour to those cells loaded in the charged state. A typical O.C.V. plot as a function of the state of charge for a Li-Al/LiCl,KCl/Co,Li_2O cell is depicted in Figure 3.12.

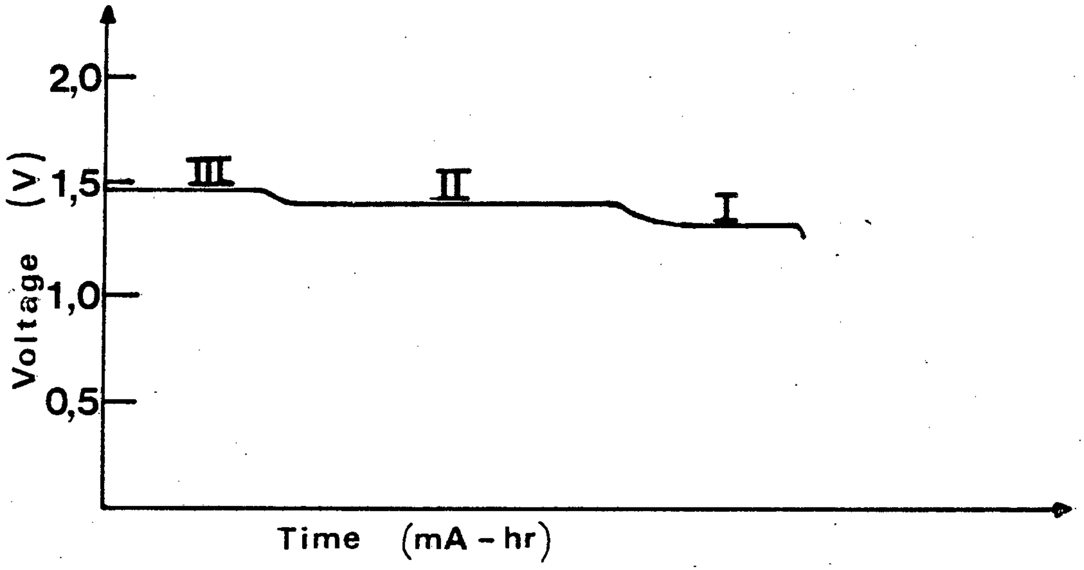

Figure 3.12:
O.C.V. plot as a function of the state of charge for a
Li-Al/LiCl,KCl/Co,Li_2O cell at 420 °C

No evidence of plateau IV (E_0 = 1,52-1,53 V) was found during the cycling of Li-Al/LiCl,KCl/Co,Li_2O high temperature cells. Only in those cells containing a large excess of Li_2O, was any evidence of plateau III (E_0 = 1,47 V) apparent and then it was short and generally found only in the first few charge cycles. Once again, plateau II (E_0 = 1,41 V) was the dominant plateau, while plateau I(E_0 = 1,31 V) was short and generally contributed less than 10% to the maximum capacity obtained from any of these cells. As would be expected, there was a fair amount of evidence of the plateau (E_0 = 2,03 V) ascribed to the chlorination of cobalt, when these cells were overcharged.

Using the theoretical capacity calculated for equation 3.9, the maximum discharge capacity obtained from a Li-Al/LiCl,KCl/Co,Li_2O cell was 50% of the theoretical value.

3.3.7 Summary of the Performance of High Temperature Lithium/Cobalt Oxide Cells

The open-circuit voltages, or E_0 values, of the plateaus occurring during the cycling of the various types of lithium/cobalt oxide cells, as recorded towards the end of each charge plateau, are listed in Table 3.2.

TABLE 3.2

E_0 values (V) for the charge plateaus and maximum discharge capacities of the various high temperature lithium/cobalt oxide cells

Cathode type	Plateau I Voltage (V)	Plateau II Voltage (V)	Plateau III Voltage (V)	Plateau IV Voltage (V)	Max. discharge capacity (mA-hr/ g cobalt oxide)
Co_3O_4	1,31	1,41	1,47	-	546
Co_3O_4,Li_2O	1,31	1,41	1,47	1,53	375
CoO	1,31	1,41	-	-	254
CoO,Li_2O	1,32	1,41	1,47	1,52	447
Co(2 g),Li_2O(1 g)	1,31	1,41	-	-	355
Co(1 g),Li_2O(3 g)	1,31	1,41	1,47	-	

Optimum cell performances in terms of both discharge capacity and cycle life were obtained from cells with Co_3O_4 cathodes without any excess Li_2O. Cells containing CoO cathodes to which no excess Li_2O had been added, delivered very poor discharge capacities. Although fairly reasonable discharge capacities were obtained from Li-Al/LiCl, KCl/Co,Li_2O cells, they achieved very poor lifetimes and often failed after only a few cycles.

3.4 ASSESSMENT OF OVERPOTENTIAL [111,112]

3.4.1 Introduction

Overpotential may be described as the difference in potential of an electrode when a finite current is passed through the electrode, from the potential of the electrode at zero current. In this section overpotential is discussed and the method of obtaining current/voltage readings for overpotential assessment of the high temperature cells is described. The overpotential effects found in the high temperature cells is also discussed.

3.4.2 General

Consider the reversible potentials adopted by a metal electrode M, when placed in a solution of M^+ ions. The steady potential results from the rapid establishment of the equilibrium:

$$M \rightleftharpoons M^+ + e \qquad (3.10)$$

no net current flowing when the forward and backward rates of the above system are equal. The further such an equilibrium lies to the right, the more negative is the electrode potential. If the equilibrium is established very rapidly, then it is possible for a potential rather more oxidizing or reducing than the equilibrium value to be imposed upon the electrode and to cause a net current flow, but without unduly disturbing the electrode potential. This is because, although the applied excess potential causes a net reaction in one direction, the equilibrium reasserts itself so rapidly that the electrode potential hardly alters, the Nernst equation still holding. A graph of current versus potential will ideally take the form shown in Figure 3.13. The small slope is due to the relative slowness of mass transfer processes with respect to the electron exchange rate.

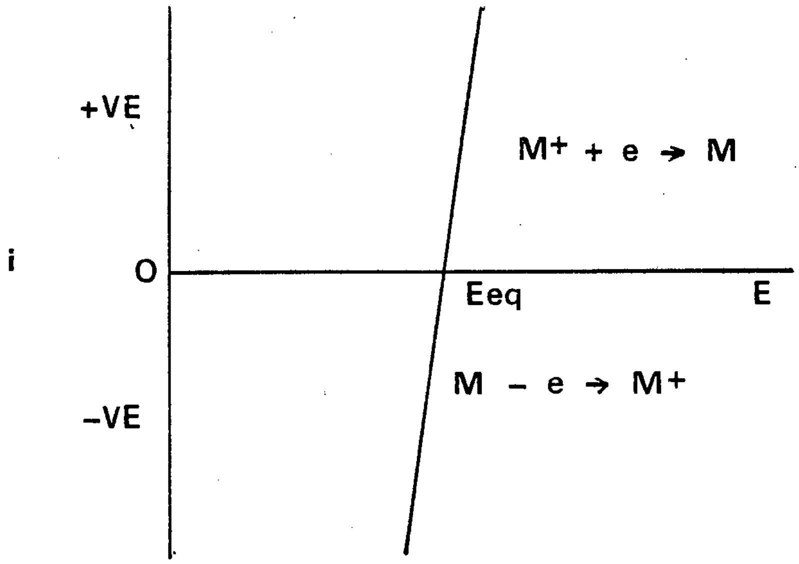

Figure 3.13:

Ideal current-potential relationship for the system $M \rightleftharpoons M^+ + e$ in which equilibrium is established almost instantaneously

However, if such a large potential is applied that a large current flows, the electrode equilibrium will not be able to maintain itself at a rate which can keep pace with that at which decomposition occurs. The potential must now alter if the current is to be maintained. The electrode process has now become effectively uni-directional and is said to take place irreversibly. The new potential will be more negative for a cathodic (reduction) process and more positive for an anodic (oxidation) process. The difference between an equilibrium and non-equilibrium potential is known as overpotential or overvoltage and is given the symbol η. Overpotential can be observed experimentally using a three electrode system and measuring the potential of the working electrode with respect to a reference half-cell. Thus:

$$\eta = E_{reaction} - E_{equilibrium} \qquad (3.11)$$

So defined, η is the total overpotential η_T, which consists of three quantities:

i) activation overpotential, η_a
ii) ohmic overpotential or IR drop, η_o
iii) concentration overpotential, η_c

Therefore:

$$\eta_T = \eta_a + \eta_o + \eta_c \qquad (3.12)$$

3.4.3 Activation Overpotential

Activation overpotential is related to the kinetics of electron transfer processes occurring within the cell. For example, a slow electron transfer has a high activation energy. If such a reaction is to proceed at a reasonable rate and produce an efficient quantity of product, a significant increase of applied potential over the equilibrium value is necessary. This excess potential is known as activation overpotential. This description emphasizes that the slow, rate-determining step in the process is the electron transfer due to the high activation energy barrier which it must cross.

3.4.4 Ohmic Overpotential

Ohmic overpotential or IR drop arises because current flows against the resistance of the cell. The most common form of ohmic overpotential arises from the passage of electric current through an electrolyte solution surrounding the electrode. Such a solution is not of infinite conductivity and shows resistance to the current flow, with the result that an ohmic or IR drop in potential occurs between the working electrodes.

A less common form of ohmic overpotential is caused by the formation, on the surface of the electrode, of an adherent layer of reaction product which is a relatively poor conductor of electricity.

3.4.5 Concentration Overpotential

This is a small, but important, effect which arises due to concentration changes induced in the vicinity of electrodes by electrochemical reactions occurring there.

Consider the simplest of all possible electrolysis cells in which two identical electrodes, M, dip into a solution of M^+ ions and let the electrode equilibria be established rapidly. If even a small potential difference is applied between the electrodes, the equilibrium is destroyed, one electrode becoming a cathode and the other an anode. At the cathode, M^+ ions are discharged at a faster rate than they dissolve and at the anode, M passes into solution more rapidly than M^+ ions are discharged. Thus, electrolysis causes a concentration gradient to develop at the surface of each electrode. However, there are three mass transport processes which act simultaneously to diminish these concentration gradients; these are:

i) diffusion of a chemical species from a region of higher concentration to one of lower concentration
ii) electrical migration due to the direction of current flow through the cell
iii) mechanical stirring, which helps decrease the differences between the concentrations at the electrode surfaces and in the bulk of the solution.

For the type of electrolysis described here, mechanical stirring is the most efficient process for eliminating the concentration gradients. However, even if the solution in contact with each electrode is very vigorously stirred, the theory of hydrodynamics indicates that a thin layer of stationary liquid always surrounds an electrode immersed in a moving solution. M^+ ions must diffuse and migrate through this thin layer of stationary liquid either to or from the electrode, as the case may be. Therefore, from the moment that electrolysis starts, the solution close to the cathode surface shows a concentration decrease. For the same current to flow, and therefore the deposition of M^+ to occur at the same rate, a more negative potential will be required. Similarly, a more positive potential will be required at the anode, since the concentration of the solution at the anode surface increases. The effect is to produce a back electromotive force (e.m.f.), so that to maintain the current flow, the applied e.m.f. must be increased by this amount. An electrode whose potential deviates from its equilibrium value due to these causes is said to be 'concentration polarized' and this effect is diffusion limited.

3.4.6 Overpotential Assessment

Equation 3.12 shows that the total overpotential, η_T is equal to the sum of the activation, ohmic and concentration overpotentials. However, the Tafel equation [111] relates the total overpotential, η_T to the net current passing through an electrode by the following equation:

$$\eta_T = a + b \ln I \qquad (3.13)$$

where a and b are constants.

It was therefore possible to assess the total overpotential of various cells by plotting the voltage against the log of the net current (in mA/cm^2). Results were obtained by increasing the amount of current applied to a cell during a charge cycle or drawn from a cell during a discharge cycle and then recording the voltage of the cell at that current once the voltage had equilibrated. In this investigation voltage values were plotted against the natural log of the net current.

The ohmic overpotential or internal resistance contribution can be calculated from the gradient of the curve obtained by plotting the voltage (V) against the current (mA). The internal resistance varies from cell to cell and cannot be completely eliminated and it was therefore necessary to calculate the internal resistance of each cell individually. The ohmic overpotential was calculated for cells having cathodes of all the types investigated in the high temperature lithium/cobalt oxide cells and a range in values between 6,5 Ωcm^2 and 43,3 Ωcm^2 was found. However, the value of 43,3 Ωcm^2 was unusually high and the average value of 14,2 Ωcm^2 gives a better reflection of the typical internal resistance of one of these cells.

Once the ohmic overpotential had been calculated, it was possible to calculate the correction, x, which must be added or subtracted from the measured potential, V, depending on whether current was drawn from (during a discharge cycle) or applied to (during a charge cycle) the cell during the current/voltage readings. Ohm's law [89] states that:

$$I = \frac{E}{R} \qquad (3.14)$$

where I = the current in Amperes
E = the voltage in Volts
R = the resistance in Ohms

Ohmic overpotential is due to the internal resistance of a cell and therefore:

$$\eta_o = IR \qquad (3.15)$$

where η_o = the ohmic overpotential
I = the applied current in Amperes
R = the cell resistance in Ohms

From the above, we can derive the following:

$$x = \frac{I}{6,9\ cm^2} \times \eta_o \qquad (3.16)$$

where 6,9 cm^2 is the surface area of the lithium/aluminium alloy anode which was used as the reference and counter electrode. A plot of the corrected voltage versus lnI therefore depicts only the concentration and activation overpotentials.

Two sets of typical current/voltage readings and the calculated correction for ohmic overpotential, x, to the voltage for a cell during a charge cycle and during a discharge cycle are given in Tables 3.3 and 3.4 respectively. The plots of voltage versus lnI for each set of values are depicted in Figures 3.14 and 3.15 respectively.

TABLE 3.3

Current/voltage readings, lnI (I in mA/cm^2), correction (x) for ohmic overpotential and the corrected voltage (V - x) for cell No. 30, a LiAl/Co$_3$O$_4$(3 g)Li$_2$O(1 g) cell during a charge cycle.

Current (mA)	Voltage (volts)	lnI (I in mA/cm^2)	x	V-x
10	1,421	0,371	0,0114	1,410
20	1,432	1,064	0,0228	1,409
30	1,458	1,470	0,0342	1,424
40	1,478	1,757	0,0456	1,432
50	1,493	1,981	0,0570	1,436
60	1,508	2,163	0,0684	1,440
70	1,524	2,317	0,0798	1,444
80	1,540	2,450	0,0912	1,449
90	1,555	2,568	0,1026	1,452
100	1,571	2,674	0,1140	1,457
110	1,584	2,769	0,1254	1,459
120	1,597	2,856	0,1368	1,460
130	1,611	2,936	0,1482	1,463
140	1,625	3,010	0,1596	1,465
150	1,639	3,079	0,1710	1,468
160	1,652	3,144	0,1824	1,471
170	1,666	3,204	0,1938	1,472
180	1,681	3,261	0,2052	1,476
190	1,696	3,316	0,2166	1,479
200	1,710	3,367	0,2280	1,482
210	1,723	3,416	0,2394	1,484
220	1,739	3,462	0,2508	1,488
230	1,754	3,507	0,2622	1,492
240	1,770	3,549	0,2736	1,496
250	1,785	3,590	0,2850	1,500
275	1,821	3,685	0,3135	1,508
300	1,858	3,772	0,3420	1,516
325	1,894	3,852	0,3705	1,524
350	1,929	3,926	0,3990	1,530
375	1,969	3,995	0,4275	1,542
400	2,016	4,060	0,4560	1,560
450	2,100	4,178	0,5130	1,587

The plots of voltage versus lnI for total overpotential assessment usually yielded good, regular curves. However, in those plots where the voltage had been corrected for ohmic overpotential, the curves were often rather irregular, especially when the readings were taken during a discharge cycle (see Figure 3.15). Once ohmic overpotential had been corrected for, the deviation from linearity of the voltage versus lnI curve is a result of activation and concentration overpotential.

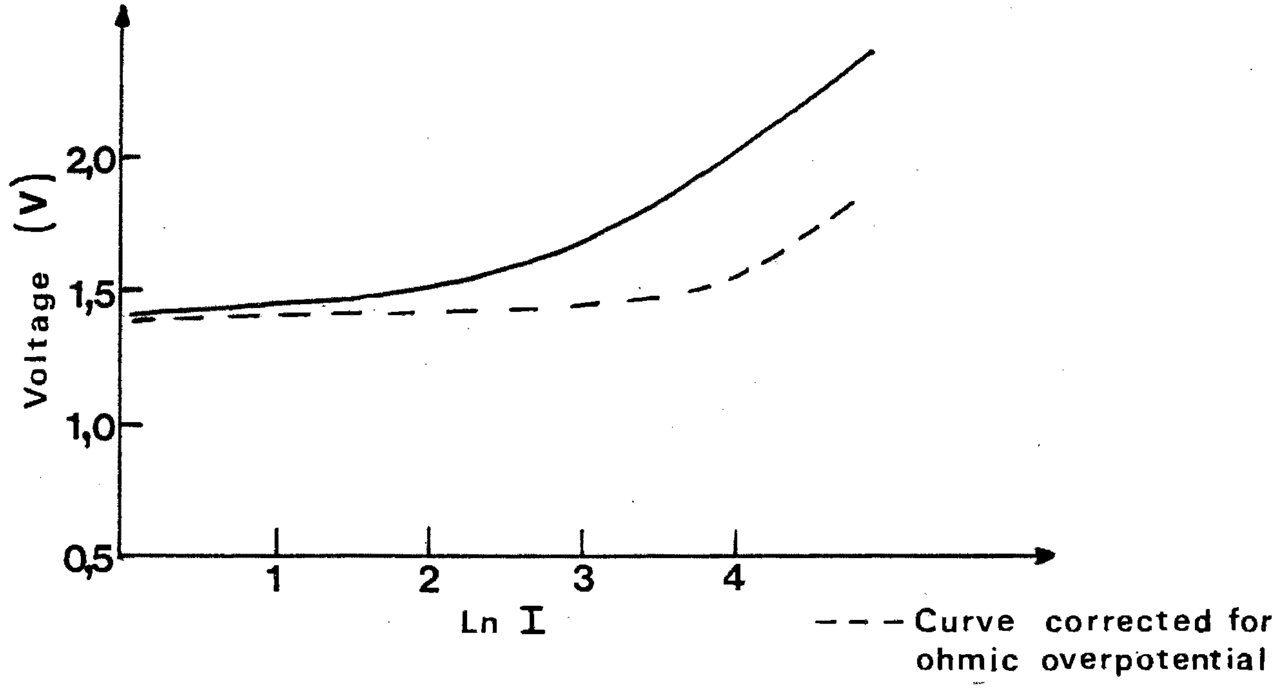

Figure 3.14:
Plot of voltage (volts) versus lnI for cell no. 30
during a charge cycle

TABLE 3.4
Current/voltage readings, lnI (I in mA/cm^2), correction (x) for ohmic overpotential and the corrected voltage (V + x) for cell No. 30, a $LiAl/Co_3O_4$(3 g)Li_2O(1 g) cell during a discharge cycle.

Current (mA)	Voltage (volts)	lnI (I in mA/cm^2)	x	V + x
10	1,329	0.371	0,0114	1,340
20	1,302	1,064	0,0228	1,325
30	1,280	1,470	0,0342	1,314
40	1,261	1,757	0,0456	1,307
50	1,241	1,981	0,0570	1,298
60	1,221	2,163	0,0684	1,289
70	1,202	2,317	0,0798	1,282
80	1,183	2,450	0,0912	1,274
90	1,165	2,568	0,1026	1,268
100	1,147	2,674	0,1140	1,261
110	1,130	2,769	0,1254	1,255
120	1,115	2,856	0,1368	1,252
130	1,099	2,936	0,1482	1,247
140	1,082	3,010	0,1596	1,242
150	1,064	3,079	0,1710	1,235
160	1,049	3,144	0,1824	1,231
170	1,034	3,204	0,1938	1,228
180	1,018	3,261	0,2052	1,223
190	1,002	3,316	0,2166	1,219
200	0,986	3,367	0,2280	1,214
210	0,970	3,416	0,2394	1,209
220	0,950	3,462	0,2508	1,201
230	0,922	3,507	0,2622	1,184
240	0,901	3,549	0,2736	1,175
250	0,880	3,590	0,2850	1,165
275	0,815	3,685	0,3135	1,129
300	0,760	3,772	0,3420	1,102
325	0,700	3,852	0,3705	1,071

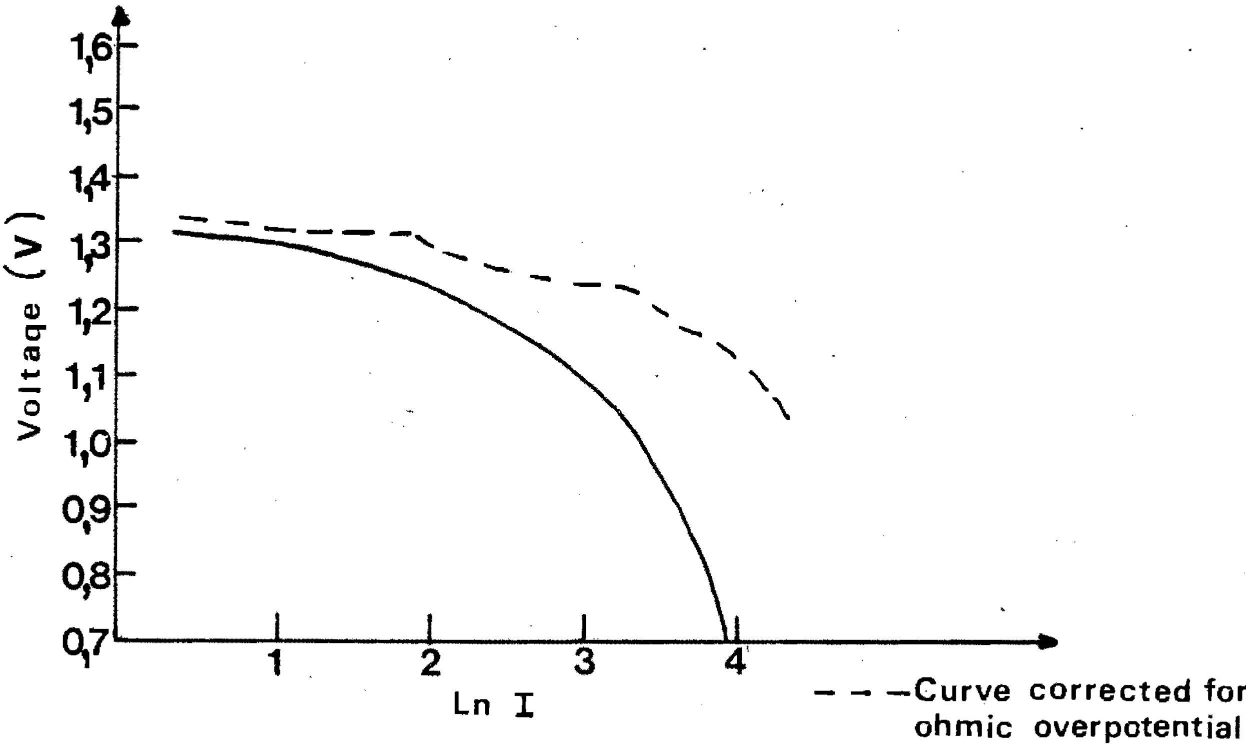

Figure 3.15:
Plot of voltage (volts) versus lnI for cell no. 30
during a discharge cycle

Figures 3.14 and 3.15 also show that overpotential effects for the high temperature cells are fairly low up to lnI = 2 or 3, the change in voltage being only about 100 mV. This indicates that these cells can tolerate up to a certain current fairly well.

Overpotential effects are also responsible for the working voltage of any one plateau varying over the length of the plateau, instead of remaining constant as might be expected. High overpotentials have been reported for lithium-aluminium alloy electrodes at high current densities [93] and since the alloy anode was used as both counter and reference electrodes for obtaining open-circuit-voltage (O.C.V.) readings of the various plateaus, concentration overpotential effects were enhanced. This resulted in the working voltages increasing and decreasing relative to the O.C.V. values during charge and discharge respectively. On open-circuit, the voltage is affected by concentration overpotential only and this is diffusion dependent. This means that if a cell is left on open-circuit for long enough, the voltage should eventually equilibrate to the true equilibrium or E_0 value which is constant along the length of any one plateau. Obviously, the longer a cell has been operating on a particular plateau, the greater the concentration polarization will be and the longer the voltage will take to equilibrate to the E_0 value.

CHAPTER 4

STRUCTURAL CHARACTERIZATION OF COBALT OXIDE CATHODES IN HIGH TEMPERATURE CELLS

4.1 INTRODUCTION

Powder X-ray diffraction techniques were used for the qualitative analysis of cobalt oxide cathodes from the various types of high temperature cells investigated. This technique was also used to determine the stability of Co_3O_4 at elevated temperatures and the reactivity of CoO and Co_3O_4 with Li_2O. In the beginning of this chapter, a brief and fairly general description of the theory of powder X-ray diffraction is given with the emphasis placed on cubic unit cells. The rest of this chapter is devoted to the description and discussion of the results obtained from the various powder X-ray diffraction spectra.

4.2 POWDER X-RAY DIFFRACTION

4.2.1 General

Since 1913, when W.L. Bragg solved the structure of NaCl, the structures of many thousands of crystals, organic and inorganic, have been determined. The basic principles in structure determination depend on the fact that the crystal structure of a substance determines the diffraction pattern of that substance or, more specifically, the size and shape of the unit cell determine the angular positions of the diffraction lines, and the arrangement of the atoms within the unit cell determines the relative intensities of the diffracted X-rays [113].

The determination of an unknown structure proceeds in three major steps [113]:

i) The shape and size of the unit cell are deduced from the angular positions of the diffraction lines. An assumption is first made as to which of the seven crystal systems the unknown structure belongs and then, on the basis of this assumption, the correct Miller indices are assigned to each reflection. This step is called "indexing the pattern" and is possible only when the correct choice of crystal system has been made. Once this is done, the shape of the unit cell is known and its size can be calculated from the positions and Miller indices of the diffraction lines.

ii) The number of atoms per unit cell is then computed from the shape and size of the unit cell, the chemical composition of the specimen and its measured density.

iii) Finally, the positions of the atoms within the unit cell are deduced from the relative intensities of the diffraction lines.

4.2.2 The Theory of Powder X-ray Diffraction

The theory of X-ray diffraction is based on Bragg's Law [114] which states that:

$$2d \sin\theta = n\lambda \qquad (4.1)$$

Where n is an integer indicating the order of the diffraction beam and the angle θ is known as the Bragg angle. For example, consider a set of parallel, equidistant lattice planes, a distance d apart. When a beam of X-rays of wavelength λ is incident on these planes at an angle θ, constructive interference of the radiation reflected from successive planes occurs whenever Bragg's Law is satisfied (Figure 4.1).

All cobalt oxide and lithiated cobalt oxide materials were characterized by cubic unit cells. Therefore, the discussion will be limited to cubic structures. For any cubic crystal, the spacing of the planes with Miller indices (h,k,l) is given by:

$$d^2 = \frac{a^2}{(h^2 + k^2 + l^2)} \qquad (4.2)$$

where a is the lattice dimension and $(h^2 + k^2 + l^2) = S$ [113].

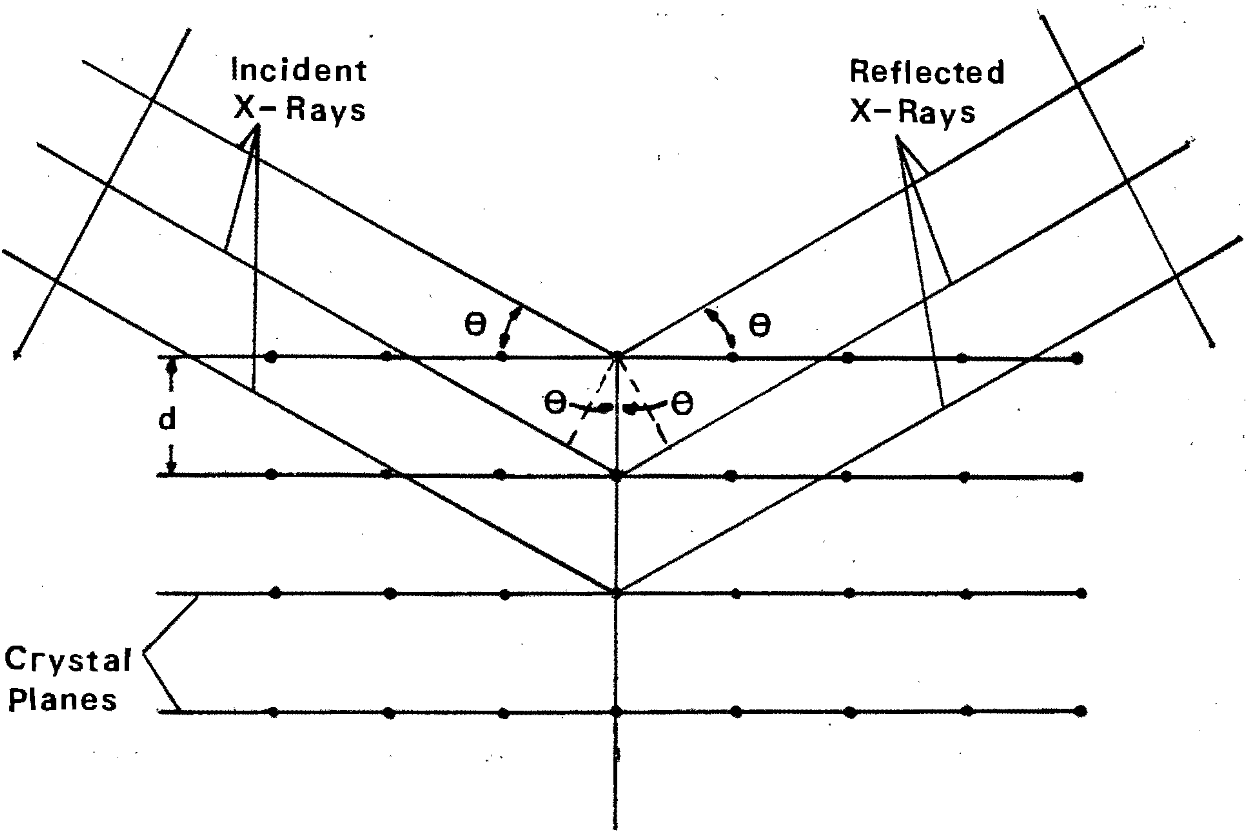

Figure 4.1:
Reflection of X-rays from a set of crystallographic planes

Combining equations 4.1 and 4.2 yields the following equation [113, 114]:

$$\frac{\sin^2\theta}{(h^2 + k^2 + l^2)} = \frac{\sin^2\theta}{S} = \frac{\lambda^2}{4a^2} \qquad (4.3)$$

Equation 4.3 relates the angle of diffraction to the Miller indices of the reflecting planes of the crystal. Since the sum $S = (h^2 + k^2 + l^2)$ is always integral and $\lambda^2/4a^2$ is a constant for any one pattern, the problem of indexing the pattern of a cubic substance is one of finding a set of integers, S, which will yield a constant quotient when divided one by one into the observed $\sin^2\theta$ values. Certain integers, such as 7, 15, 23, 28, 31 etc. are impossible because they cannot be formed by the sum of three squared integers. Once the proper integers, S are found, the indices, hkl of each line can be determined [113].

The proper set of integers, S is not hard to find because there are only a few possible sets. Each of the four common cubic lattice types has a characteristic sequence of diffraction lines, described by their sequential S values:

Simple cubic : 1,2,3,4,5,6,8,9,10,11,12,13,14,16 ...
Body-centred cubic: 2,4,6,8,10,12,14,16 ...
Face-centred cubic: 3,4,8,11,12,16 ...
Diamond cubic : 3,8,11,16 ...

Each set can be tried in turn. If a set of integers satisfying equation 4.3 cannot be found, then the substance involved does not belong to the cubic system and other possibilities must be explored [113].

In applying Bragg's Law to X-ray powder diffraction, use of monochromatic X-rays, such as CuK_α rays is made. These rays are allowed to fall on the powdered sample which is rotated through the various diffraction angles. A detector, which picks up the diffracted rays is also rotated through the various diffraction angles. The diffraction intensity is determined as a function of the Bragg angle, θ.

The powdered sample contains crystallites orientated randomly at all possible angles. As a result, there will always be some of the crystal faces at the appropriate angles for diffraction at each value for θ which satisfies the Bragg equation. For each angle satisfying Bragg's equation, a diffraction line is picked up by the detector and recorded electronically by the deflection of a pen on a recorder. The recorder is calibrated to run in conjunction with the rate of rotation of the sample through the Bragg angles, so that the peaks are translated directly onto the recorder at the angles at which diffraction occurs [114]. Figures 4.2 and 4.3 depict typical X-ray diffraction patterns for Co_3O_4 and CoO.

4.3 STRUCTURAL X-RAY DIFFRACTION ANALYSES OF CATHODES FROM HIGH TEMPERATURE CELLS

In an attempt to identify the products formed during the cycling of these cells, powder X-ray diffraction analyses of cathodes were undertaken at various stages of charge and discharge.

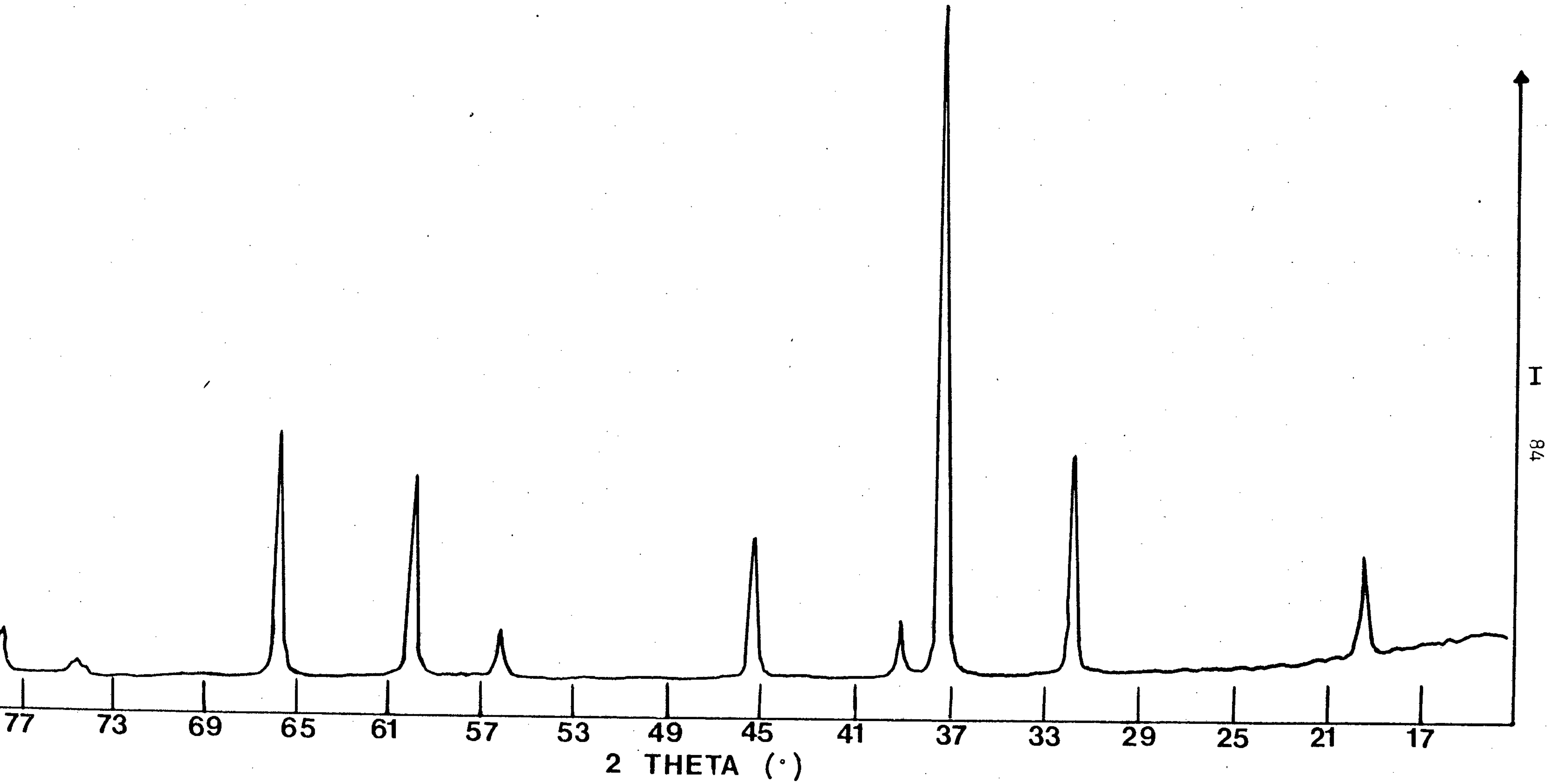

Figure 4.2:

X-ray diffraction spectrum of Co_3O_4

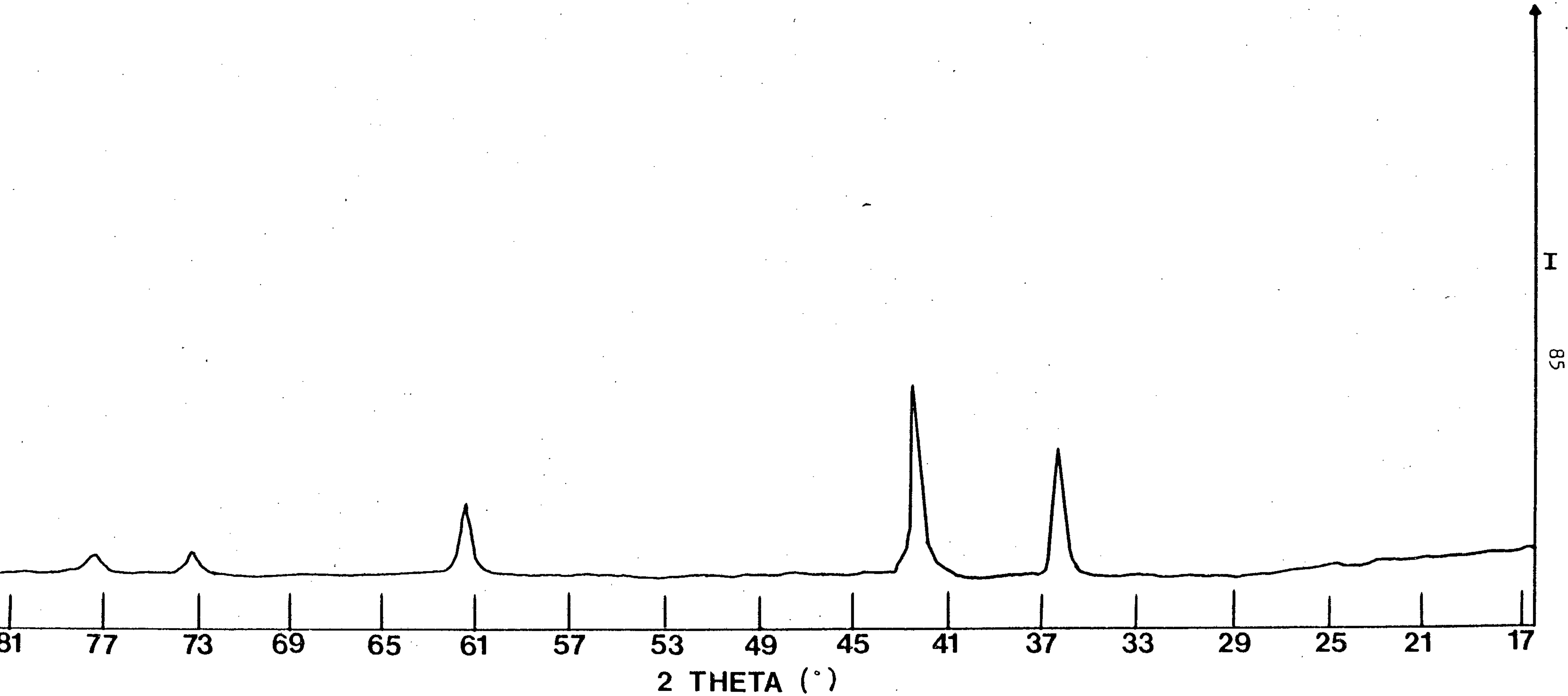

Figure 4.3:

X-ray diffraction spectrum of CoO

The spectrum of a charged CoO,Li_2O cathode that had not been allowed to cycle more than four times, revealed new broad peaks, all of which could be attributed to Co_3O_4. Figure 4.4 illustrates a typical X-ray diffraction (XRD) spectrum of a charged CoO,Li_2O cathode at the end of an early charge cycle. These Co_3O_4 peaks were not evident in spectra of charged CoO,Li_2O cathodes that had been allowed to cycle for substantially longer times. Severe weakening and broadening of the Co_3O_4 peaks were observed in the spectrum of a fully charged Co_3O_4,Li_2O cathode (see Figure 4.5 for a typical XRD spectrum of such a cathode). These results indicate that Co_3O_4 is not stable in the cell environment and, as will be more fully discussed later, investigation into the stability of Co_3O_4 in the LiCl,KCl eutectic was in good agreement with these findings.

The spectra of fully charged Co_3O_4,Li_2O and fully charged CoO,Li_2O cathodes which had only cycled a few times, also contained a few extra diffuse peaks that could not be identified as shown in Figures 4.4 and 4.5. It was concluded that during the charging process, CoO (rocksalt-type structure) is oxidized to Co_3O_4 (spinel-type structure) and that further oxidation of Co_3O_4 gives rise to an unstable compound with postulated formula $Li_{2x}Co_2O_{3+x}$ for $x \geqslant 0$. The charging reactions corresponding to plateaus III and IV can therefore be represented as follows:

$$3CoO + Li_2O \rightleftharpoons Co_3O_4 + 2Li \text{ (alloyed with Al)} \qquad (4.4)$$

$$\begin{aligned} 2Co_3O_4 + (1 + 3x)Li_2O \longrightarrow\ & 3Li_{2x}Co_2O_{3+x} \\ & + 2Li\text{(alloyed with Al)} \qquad (4.5) \end{aligned}$$

The E_0 value of 1,47 V observed for reaction 4.4 at 420 °C differs by 0,18 V from the theoretical value for the reaction calculated from available thermodynamic data [104].

The fact that plateaus III and IV were not always clearly distinguishable during discharge and that after a few successive cycles all evidence of either plateau completely disappeared, indicates that both the hypothetical $Li_{2x}Co_2O_{3+x}$ compound and Co_3O_4 are unstable in the cell environment.

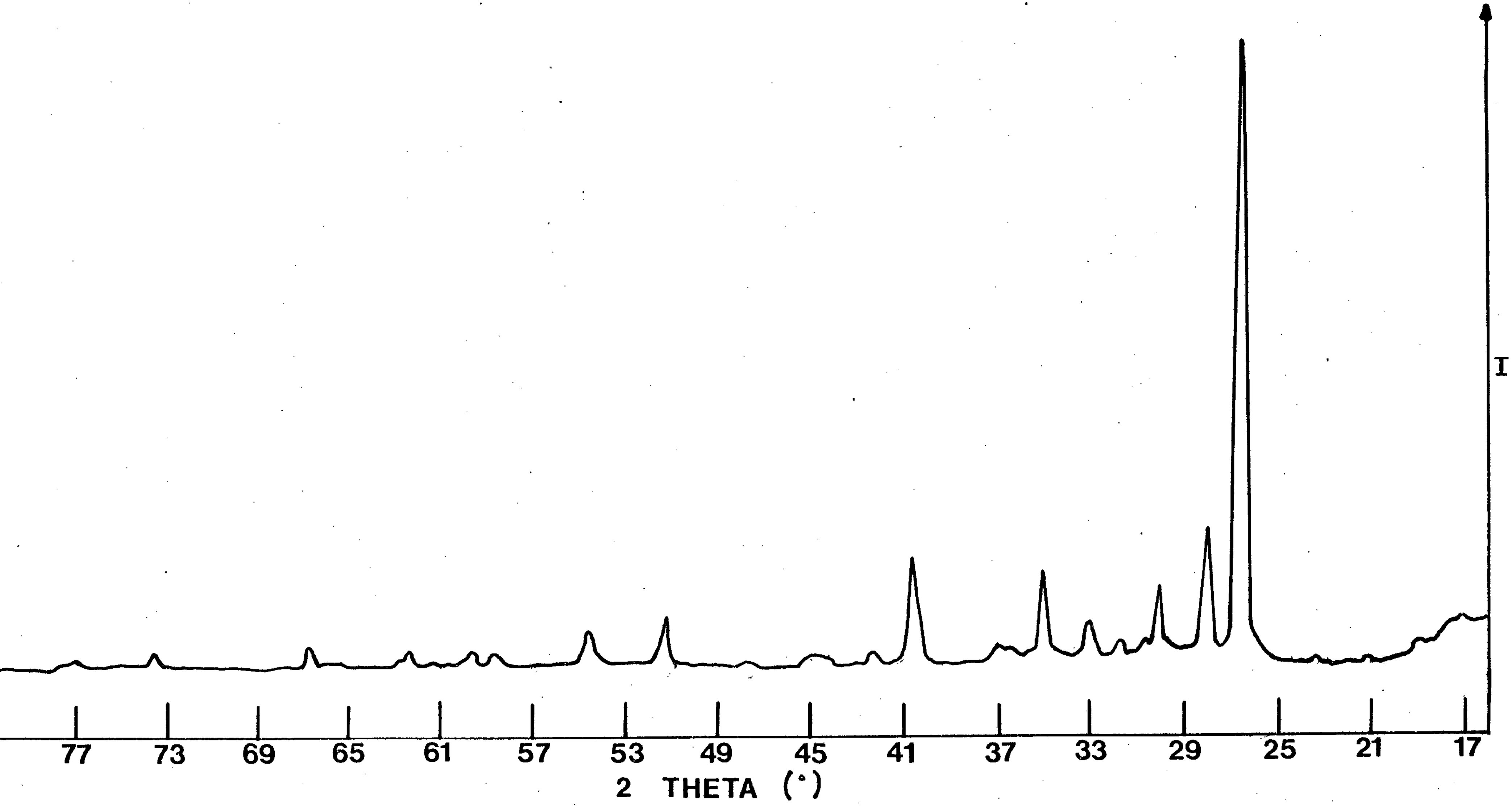

Figure 4.4:

X-ray diffraction spectrum of fully charged CoO,Li_2O cathode at end of early charge cycle

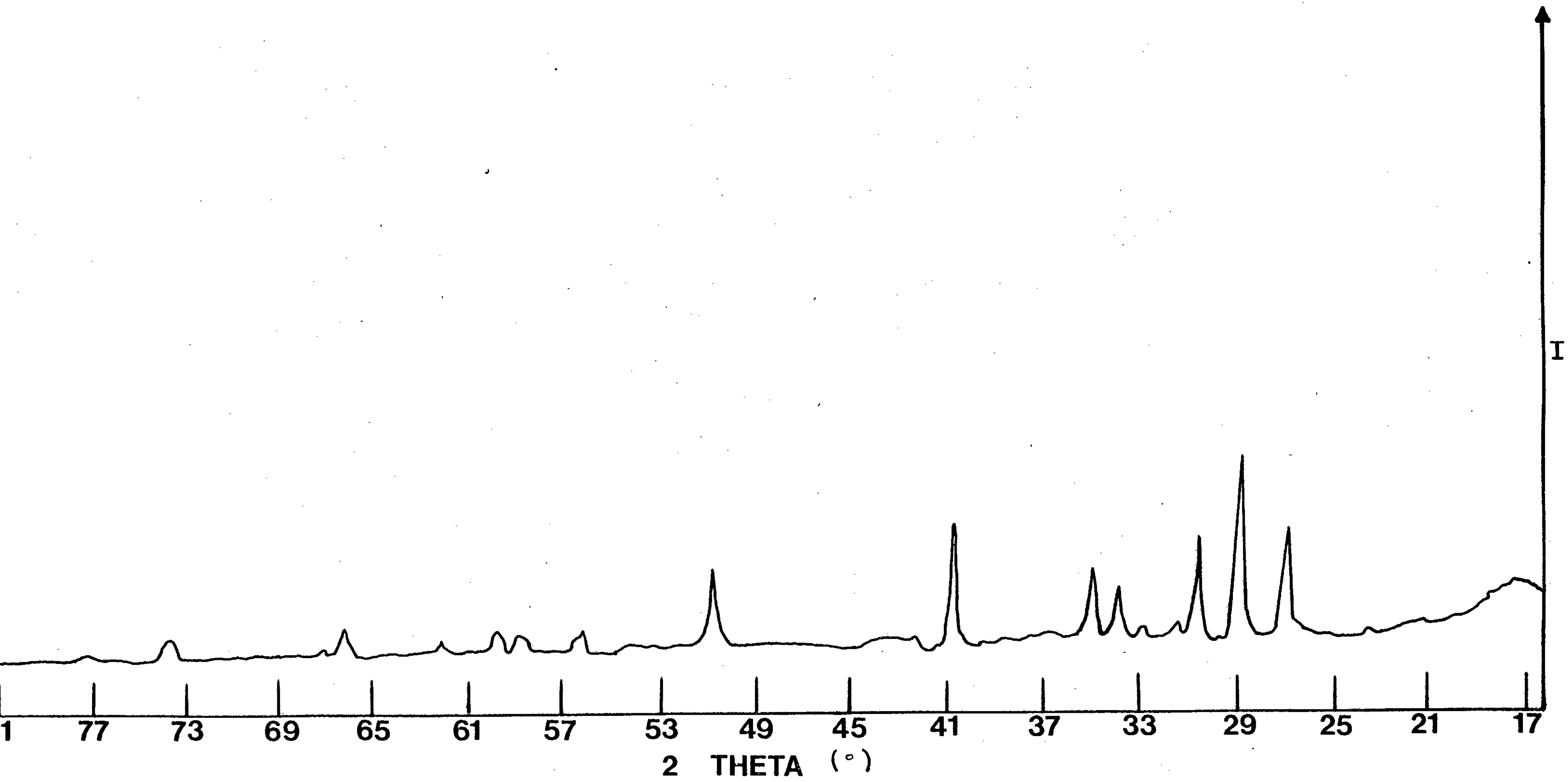

Figure 4.5:

X-ray diffraction spectrum of fully charged Co_3O_4,Li_2O cathode

In addition to the peaks that characterized Co_3O_4 and $Li_{2x}Co_2O_{3+x}$, the spectra of charged CoO,Li_2O and Co_3O_4,Li_2O cathodes, also contained several other peaks that disappeared on washing of the samples. These peaks were also evident in the spectra of unwashed powdered samples of CoO and Co_3O_4 that had been immersed in a LiCl,KCl eutectic melt at 420 °C for several days. The result of this investigation and the unidentified compound formed will be discussed more fully later.

X-ray diffraction analyses of Co_3O_4 and CoO cathodes that had reached a state of charge as represented by plateau II in Figures 3.8 to 3.11 were also undertaken. Well defined peaks indicated the presence of CoO with rocksalt-type structure. This plateau was therefore attributed to the reaction:

$$Co + Li_2O \rightleftharpoons CoO + 2Li \text{ (alloyed with Al)} \qquad (4.6)$$

The theoretical E_0 value of 1,43 V calculated for this reaction at 420 °C from thermodynamic data [104] is in very good agreement with the observed E_0 value of 1,41 V for plateau II.

In all the high temperature cobalt oxide cells investigated. plateau II became the predominant plateau after only a few charge/discharge cycles (2 to 4). This finding is in fact not surprising when one considers that Co^{II} is more stable than Co^{III} [115]. It is interesting to compare these results to those obtained for the high temperature Fe_3O_4 cathodes [31] in which Fe_3O_4 was found to be the most stable phase, while FeO with rocksalt structure is unstable below 580 °C and disproportionates into Fe_3O_4 and α-Fe.

Two metallic phases of cobalt. viz. α-Co (hexagonal close packed) and β-Co (face centred cubic) were evident in the spectra of discharged Co_3O_4 and CoO cathodes, although β-Co was always found to be present in trace amounts. The nature of the reaction that gives rise to plateau I has not yet been determined. However, it is of interest to speculate about the fact that β-Co is always present in trace amounts while plateau I is short and generally contributes less than 10% of the total capacity obtained from any one cell. It is feasible that the oxidation of β-Co to CoO may occur at a voltage different from that at which α-Co is oxidized to CoO. If one assumes that this is the case, then the charging reaction giving rise to plateau I may be represented as follows:

$$\beta\text{-Co} + Li_2O \rightleftharpoons CoO + 2Li \text{ (alloyed with Al)} \qquad (4.7)$$

The E_0 value observed for this plateau was between 1,31 and 1,32 V. Unfortunately, no thermodynamic data is available for the oxidation of β-Co to CoO and therefore it was not possible to calculate a theoretical E_0 value for this reaction. β-Co exists above 450 °C, but below this temperature, mixtures of β-Co and α-Co exist [116]. The high temperature cells were operated at 420 °C, so one might expect to find an appreciable amount of β-Co present at this temperature. However, assuming that reactions 4.6 and 4.7 give rise to plateaus II and I respectively, then α-Co would be formed before β-Co during the reduction process. This is in agreement with the X-ray diffraction spectra of fully discharged Co_3O_4 and CoO cathodes which always showed α-Co to be present in much larger quantities than β-Co.

Cells which were loaded in the fully discharged state, tended to have very long charge cycles and relatively short discharge cycles. However, plateau V, which was attributed to the chlorination of cobalt, was always present and in many cases was the dominant plateau for these cathodes. It is possible that $CoCl_2$ formed during the oxidation giving rise to plateau V, was dispersed rapidly into the LiCl,KCl electrolyte, resulting in short discharge cycles.

4.4 UNIDENTIFIED PEAKS IN X-RAY DIFFRACTION SPECTRA OF CATHODES FROM HIGH TEMPERATURE CELLS

The spectra of fully charged CoO,Li_2O and Co_3O_4,Li_2O cathodes often contained a fairly strong peak at d = 2,71 Å and a weak, diffuse peak at d = 3,83 Å. The compound giving rise to these peaks could not be identified, but was obviously stable in air, since these peaks were evident in samples which had been exposed to air. They did however disappear on washing of the samples. These unidentified peaks were also evident in the X-ray diffraction spectra of unwashed powdered samples of CoO and Co_3O_4 that had been immersed in a LiCl.KCl melt at 420 °C for several days and were attributed to an unidentified water soluble compound formed by reaction of the oxides with the melt.

4.5 THE STABILITY OF COBALT OXIDE AT ELEVATED TEMPERATURES

The X-ray diffraction spectrum of a sample of Co_3O_4 which had been heated at 420 °C under argon for several hours, revealed that no structural changes had occurred. It was therefore concluded that operation at the cell temperature (i.e. 420 °C) does not result in any breakdown of Co_3O_4.

4.6 REACTIVITY OF COBALT OXIDES WITH Li_2O

The X-ray diffraction spectrum of a sample of CoO which had been reacted with Li_2O under vacuum at 420 °C for 20 hours, indicated the presence of significant amounts of Li_6CoO_4. A number of fairly weak peaks which could not be identified, also characterized this spectrum. These peaks, together with the formation of Li_6CoO_4, reflect the reactivity of CoO with Li_2O at 420 °C. The X-ray diffraction spectrum of this sample after it had been washed with water, revealed the presence of only unreacted CoO and cobalt hydroxide ($Co(OH)_2$), the peaks due to Li_2O and Li_6CoO_4 having disappeared. It must be stressed however, that in no case was any evidence of Li_6CoO_4 ever found in the X-ray diffraction spectra of any of the high temperature cell cathodes.

Co_3O_4 was found to be stable in Li_2O and on washing of the Co_3O_4 sample that had been heated with Li_2O under vacuum at 420 °C for 20 hours, only Co_3O_4 peaks were evident in the X-ray diffraction spectrum, those due to Li_2O having disappeared.

4.7 CONCLUSIONS FOR HIGH TEMPERATURE LITHIUM/COBALT OXIDE CELLS

Relatively short lifetimes were obtained from the high temperature Li-Al/LiCl,KCl/Co_3O_4 and Li-Al/LiCl,KCl/CoO cells. This is in contrast to the superior lifetime performances achieved from similar cells containing α-Fe_2O_3 and Fe_3O_4 cathodes [31]. The iron-oxide cells delivered capacities in excess of 400 mA-hr/g for several months, whereas high discharge capacities were generally delivered by Co_3O_4 and CoO cathodes during the early cycles of cell operation only. This can be attributed to the fact that, in the iron oxide system, the lithiated iron oxide phases were stable in the LiCl,KCl electrolyte: this is apparently not the case for the cobalt oxide system.

Bearing in mind the importance of the structural properties of the cathode, it is interesting to compare the results for the high temperature lithium/cobalt oxide cells with those reported by Godshall et al, who describe the electrochemical performance of $LiCoO_2$ cathodes in a similar cell environment [30]. Their cell discharges according to the reaction:

$$3Li + LiCoO_2 \rightleftharpoons 2Li_2O + Co \qquad (4.8)$$

The reaction occurs on a single plateau (E_0 = 1,336 V, obtained with an $Al,Li_{0,9}Al$ reference electrode) and is reversible provided that the cell is not discharged to its compositional limits. Unlike CoO and Co_3O_4,$LiCoO_2$ was reported to be stable in the LiCl,KCl electrolyte.

In conclusion it is evident from the available data, that, during the charge/discharge cycling of Co_3O_4 and CoO cathodes, several distinct phases are generated. The reaction sequence at the cathode during charge (in the presence of excess Li_2O) and discharge as determined by powder XRD methods may be represented as follows:

	Structure	Oxidation state of Co
$Li_{2x}Co_2O_{3+x}$ ($x \geqslant 0$)	Unknown	+ 3
$\uparrow$ (a)		
Co_3O_4	Spinel	+ 3, + 2
$\updownarrow$ (b)		
CoO	Rocksalt	+ 2
$\updownarrow$ (c)		
Co	Hexagonal-close-packed and face-centred-cubic (i.e. two phases present)	0

The exact nature of the compound $Li_{2x}Co_2O_{3+x}$ and the reversibility of reaction (a) have not been ascertained. The performance of these cells appears to be severely restricted by the following main factors:

i) an instability of the cobalt oxides $Li_{2x}Co_2O_{3+x}$, Co_3O_4 and CoO in the LiCl,KCl eutectic melt at 420 °C

ii) dispersion of the discharge product, Li_2O into the electrolyte.

CHAPTER 5

CHEMICAL LITHIATION OF Co_3O_4 AT 50 °C AND ELECTROCHEMICAL LITHIATION OF Co_3O_4 AT AMBIENT TEMPERATURE

5.1 INTRODUCTION

This chapter reports results of the chemical and electrochemical lithiation of Co_3O_4 at ambient temperature. Structural characterization of the lithiated product by powder X-ray diffraction technique is presented.

5.2 CHEMICAL LITHIATION OF COBALT OXIDE AT 50 °C

The lithium content of the $Li_xCo_3O_4$ samples as determined by atomic-absorption methods are listed in Table 5.1 together with the reaction conditions. It is evident from these results that the values of x were dependent on the concentration of lithium (in the form of n-butyllithium) and on the reaction time. The maximum x value obtained was 1,92, indicating that almost two lithium ions can be inserted into Co_3O_4 per formula unit on reaction with n-butyllithium.

TABLE 5.1

Reaction conditions for the lithiation of Co_3O_4 showing the dependence of x on the concentration of lithium and on reaction time.

Reaction time (hours)	Reaction temperature (°C)	Moles Li added per mole Co_3O_4	% lithium	x.
24	50	1,2	1,58	0,56
48	50	1,2	1,72	0,61
24	50	1,7	1,45	0,51
48	50	1,7	2,38	0,85
24	50	2,0	2,46	0,88
48	50	2,0	2,31	0,82
115	50	3,5	5,25	1,92

The X-ray diffraction profiles up to $2\theta = 80^{\circ}$ of Co_3O_4 and $Li_xCo_3O_4$ (x = 1,92) are displayed in Figures 5.1 and 5.2 respectively.

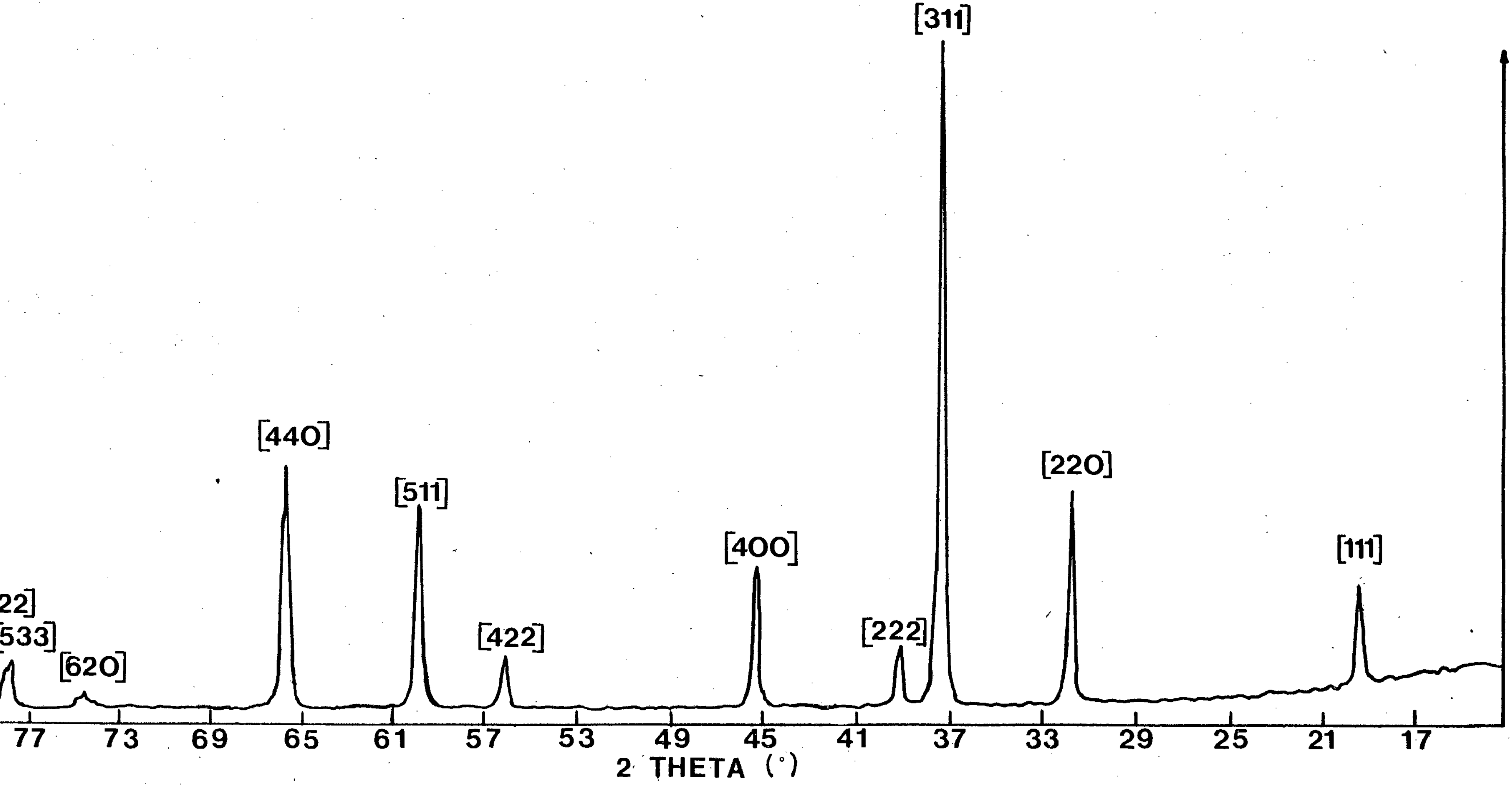

Figure 5.1:

X-ray diffraction profile of Co_3O_4

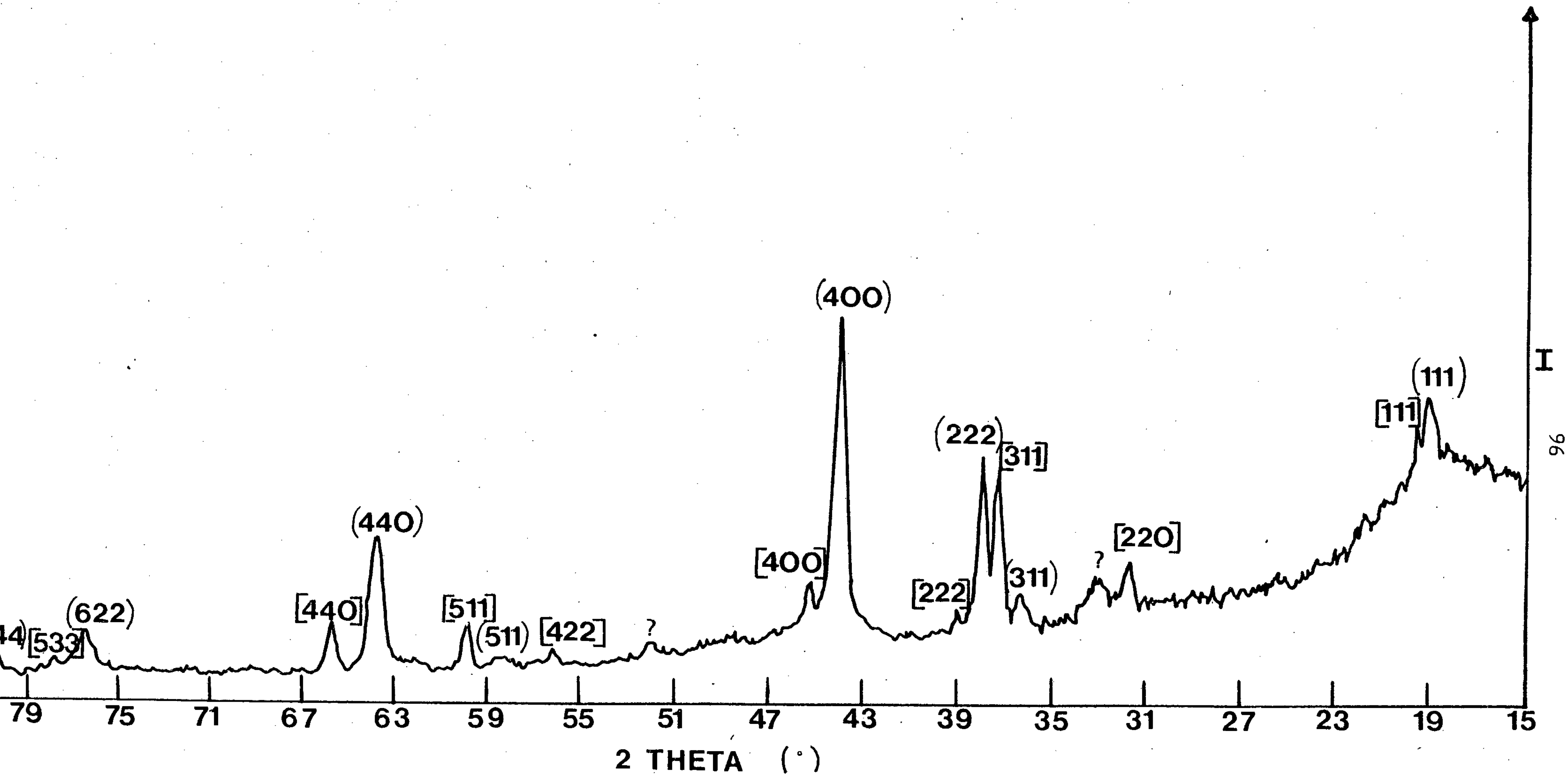

Figure 5.2:

X-ray diffraction profile of $Li_xCo_3O_4$

Table 5.2 lists the X-ray intensity data obtained for $Li_{1,92}Co_3O_4$. Data for Co_3O_4 (spinel) and CoO (rocksalt) have been included in the table for comparison.

TABLE 5.2

X-ray diffraction data of Co_3O_4, CoO and $Li_xCo_3O_4$ (x = 1,92) for $2\theta \leqslant 132$ °.

'a' lattice parameter (Å)	Co_3O_4 [117]	CoO [88]	$Li_{1,92}Co_3O_4$
	8,084	8,520	8,309
h k l	Spinel $^I/I_1$	Rocksalt $^I/I_1$	$^I/I_1$
1 1 1	20	-	17,3
2 2 0	40	-	
3 1 1	100	-	8,5
2 2 2	12	75	43,0
4 0 0	25	100	100,0
3 3 1	-	-	2,3
4 2 2	12	-	
3 3 3 } 5 1 1 }	35	-	5,2
4 4 0	45	50	45,2
5 3 1	-	-	1,2
6 2 0	6	-	
5 3 3	12	-	
6 2 2	8	20	18,8
4 4 4	4	16	14,8
7 1 1	4	-	
6 4 2	8	-	
7 3 1	16	-	
8 0 0	8	10	6,4
8 2 2	6	-	
7 5 1	16	-	
6 6 2	6	14	9,9
8 4 0	-	30	15,2
8 4 4	-	-	19,1

Note: The ASTM Powder Diffraction File does not list X-ray intensity data for Co_3O_4 beyond $2\theta = 112,4$ ° and for CoO beyond $2\theta = 108,1$ °.

Although the idealized CoO rocksalt structure is normally assigned to space group Fm3m (O_h^5), a = 4,260 Å [88], its Co^{2+} ions can be regarded as occupying all the octahedral sites of space group Fd3m, the 64 tetrahedral sites remaining empty. In Table 5.2 the diffraction pattern of CoO has been indexed to a super cell with a = 2 x 4,260 Å to allow direct comparison with Co_3O_4 and $Li_{1,92}Co_3O_4$.

Although the X-ray diffraction pattern of $Li_{1,92}Co_3O_4$ (Figure 5.2) shows evidence of some unreacted Co_3O_4 (most probably the large particles) the peaks of $Li_{1,92}Co_3O_4$ were generally well resolved, enabling a reasonably accurate determination of their intensities. Intensities were measured gravimetrically using a 5-figure balance. Although the diffraction profile of $Li_{1,92}Co_3O_4$ could be indexed to the spinel space group Fd3m (O_h^7), a comparison of this profile (Figure 5.2) with that of Co_3O_4 (Figure 5.1) shows differences in both the intensities and positions of the peaks. The difference in the intensities of the peaks indicates movement of the cobalt atoms within the cubic-close-packed oxide lattice. In addition the peaks of the diffraction profile for $Li_{1,92}Co_3O_4$ are shifted to lower 2θ values compared with those of the Co_3O_4 diffraction profile; this indicates an expansion in the oxide lattice during the lithiation process. Insertion of lithium into Co_3O_4 resulted in an expansion of the cubic cell edge from 8,084 Å to 8,309 Å, which represents an 8,58% increase in the volume of the Co_3O_4 unit cell. This is a significantly larger increase in volume than that of 2,8% reported for the lithiation of Fe_3O_4 [32].

A cursory examination of Table 5.2 indicates that the structure of $Li_{1,92}Co_3O_4$ is intermediate between spinel and rocksalt, but is predominantly rocksalt. In fact, the relative intensities of the diffraction peaks of $Li_{1,92}Co_3O_4$ correlate closely with those of CoO (rocksalt). These findings are in very good agreement with those of Thackeray et al [32] in their studies of the lithiated iron oxides. They produced $Li_xFe_3O_4$ (x = 1,5), the diffraction profile of which could be indexed to the space group Fd3m (O_h^7). As with the $Li_xCo_3O_4$ compounds, $Li_{1,5}Fe_3O_4$ was found to have a structure intermediate between spinel and rocksalt, but which was also predominantly rocksalt. Structural analysis of $Li_{1,5}Fe_3O_4$ indicated that the $[Fe_2]O_4$

sublattice of the Fe_3O_4 spinel structure remained intact during lithiation.

The fact that the $Li_xCo_3O_4$ compounds have structures which are predominantly rocksalt, of necessity implies that the tetrahedral Co^{2+} ions must be displaced from the 8a sites to empty 16c sites via a common 8a/16c face.

In an initial attempt to characterize the structure of $Li_{1,92}Co_3O_4$ a model for $Li_{1,0}Co\ [Co_2]O_4$ was computed using the Lazy Pulverix program. This program computes what the X-ray diffraction pattern should be for a known structure, the structural parameters being the "input" for the program. For the $LiCo[Co_2]O_4$ model computed in this investigation, the "input" conditions consisted of one Li^+ ion and one Co^{2+} ion per formula unit positioned in the 16c sites of space group Fd3m. The oxygen and remaining $Co^{3+/2+}$ ions occupied the 32e and 16d sites respectively. This structure may therefore be regarded as a partially ordered rocksalt structure; the octahedral B sites of the spinel structure are unaffected by lithiation and the remaining octahedral sites are randomly occupied by Li^+ and Co^{2+} ions. Table 5.3 lists the hkl values and relative intensities of the X-ray diffraction pattern computed for this model using the Lazy Pulverix program; the relative intensities of the X-ray diffraction profile obtained from $Li_{1,92}Co_3O_4$ have been included for comparison.

The relative intensities of the X-ray diffraction profile of $Li_{1,92}Co_3O_4$ correlate well with those obtained for the $LiCo[Co_2]O_4$ model computed using the Lazy Pulverix program. (It must be noted that an additional 0,92 Li^+ ions to the computed structure would not significantly alter the calculated intensities as lithium is a very light scatterer of X-rays). This seems to suggest that the 8a site Co^{2+} ions are displaced to the 16c sites during lithiation, as expected, and that the inserted Li^+ ions up to $x = 1$ occupy the remaining 16c sites. At $x = 1$ in $Li_xCo_3O_4$, all the 16c octahedral sites are filled. Therefore, for $x > 1$, Li^+ ions entering the spinel framework must either occupy tetrahedral vacancies, 8a, or fill octahedral sites at the expense of cobalt ions which would be extruded from the oxide lattice as metal cobalt, Co^0. That is, the reaction would either be:

TABLE 5.3

X-ray diffraction data for $LiCo[Co_2]O_4$ computed using Lazy Pulverix program and X-ray diffraction intensities obtained for $Li_{1,92}Co_3O_4$

h k l	Intensity of computed XRD pattern	Intensity of XRD pattern for $Li_xCo_3O_4$
1 1 1	30,7	17,3
2 2 0	<0,1	-
3 1 1	7,1	8,5
2 2 2	58,5	43,0
4 0 0	100,0	100,0
3 3 1	1,4	2,3
4 2 2	<0,1	-
5 1 1	4,5	5,2
3 3 3	0,1	-
4 4 0	49,1	45,2
5 3 1	3,5	1,2
4 4 2	<0,1	-
6 2 0	<0,1	-
5 3 3	0,8	-
6 2 2	26,7	18,8
4 4 4	13,4	14,8
5 5 1	1,3	-
7 1 1	0,4	-
6 2 2	<0,1	-

$$0{,}92Li + LiCo[Co_2]O_4 \longrightarrow (Li_{0,92})_{8a}(LiCo)_{16c}[Co_2]_{16d}O_4 \text{ or}$$

$$0{,}92Li + LiCo[Co_2]O_4 \longrightarrow Li_{1,92}Co_{2,08}O_4 + 0{,}92Co$$

In the case of Fe_3O_4, it was originally proposed [32] that lithiation in excess of $x = 1$ resulted in the 8a and/or 48f tetrahedral sites being occupied, occupation of the 8b sites being energetically unfavourable as these tetrahedra share all four faces with neighbouring, occupied 16d octahedra. However, compounds with $x > 1$ were observed to be unstable and tended to ignite in air, particularly for high values of x.

This was attributed to lithium diffusion from the bulk of a particle back to the surface where oxidation of metallic lithium readily occurs [37]. However, in view of subsequent studies [33] and the disclosure that traces of "unreacted iron oxide" were present after reaction of Fe_3O_4 with n-butyllithium [32], it appears that for $x > 1$, finely divided iron may also be extruded from the lattice to accommodate the excess lithium. The surface iron is readily oxidized when exposed to air.

In view of these findings, it was initially thought that lithiation of $Li_xCo_3O_4$ in excess of $x = 1$, was more likely to result in extrusion of Co^{2+} ions from the 16c sites than in occupation of the tetrahedral sites by the excess Li^+ ions because of the close proximity of the 8a and 16c sites (~1,8 Å). Furthermore, after being dried under vacuum, $Li_{1,92}Co_3O_4$ was found to be ferromagnetic as could be seen from the interaction of the dried $Li_{1,92}Co_3O_4$ particles with the magnetic stirrer in the reaction vessel. This was initially attributed to the presence of cobalt metal in very finely divided form, even though no cobalt could be detected in crystalline form on the powder X-ray diffraction profile.

In order to determine which process occurs during lithiation beyond $x = 1$, an attempt was made to refine the structure of $Li_{1,92}Co_3O_4$ using a least squares intensity refinement program developed by Wiseman. The Wiseman program refines the structural parameters of a compound from the Bragg intensities obtained from the X-ray diffraction profile of that compound. The structure of $Li_{1,92}Co_3O_4$ was refined using 14 intensities obtained from 15 reflections. The refinement was carried out with a model similar to that used previously for $Li_xFe_3O_4$ [32] and $LiMn_3O_4$ [37]. Listed below is a summary of the structural parameters which were refined for $Li_{1,92}Co_3O_4$ using the Wiseman program. No more than 5 parameters were refined during any one least-squares cycle.

i) Scale factor
ii) Occupancy of Li^+ on the 8a sites
iii) Occupancy of Li^+ on the 16c sites } sum restricted to 2
iv) Occupancy of Co on the 16c sites } per formula unit.

v) Occupancy of Li^+ on the 16d sites } sum restricted to 2
vi) Occupancy of Co on the 16d sites } per formula unit.
vii) Temperature factor, B for cobalt
viii) Temperature factor, B for oxygen
ix) x,y,z parameters for oxygen

An R factor of 5,63%, where

$$R = \sum \left| I_{obs} - I_{calc} \right| / \sum I_{obs}$$

was obtained with a structure having the refined atomic parameters which are given in Table 5.4. Observed and calculated Bragg intensities are listed in Table 5.5.

TABLE 5.4

Structural parameters of $Li_{1,92}Co_3O_4$ (R = 5,63%)

Atom	Position	x	y	z	B (Å^2)	Occupancy* n
Li^+	8a	0,125	0,125	0,125	1,0	0,27(17)
Li^+	16c	0,000	0,000	0,000	1,0	0,50 (3)
Li^+	16d	0,500	0,500	0,500	1,0	-0,02 (5)
Co	16c	0,000	0,000	0,000	0,4(4)	0,50 (3)
Co	16d	0,500	0,500	0,500	0,9(3)	1,02 (5)
O^{2-}	32e	0,254(2)	0,254(2)	0,254(2)	3,3(6)	2,00

Figures in brackets represent the standard deviation.
* The occupancy is given in terms of the relative number of atoms in the unit cell.

Other physically realistic models failed to provide a better fit to the data. The results of the Wiseman program enable the following important conclusions to be made about the structure of $Li_xCo_3O_4$ (x = 1,92):

i) refinement of the cobalt occupancy of the 16d (B-sites) positions (total = 2,04(10)) showed that the $[Co_2]O_4$ framework of the original Co_3O_4 spinel remained intact within experimental error

TABLE 5.5

Observed and calculated intensities for $Li_{1,92}Co_3O_4$

h k l	I_{calc}	I_{obs}
1 1 1	283	281
3 1 1	146	138
2 2 2	690	697
4 0 0	1 580	1 620
3 3 1 5 1 1	} 32	38
3 3 3	50	84
4 4 0	803	732
5 3 1	31	20
6 2 2	315	305
4 4 4	204	240
8 0 0	91	104
6 6 2	159	161
8 4 0	268	246
8 4 4	288	309

ii) one Li^+ ion and one Co^{2+} ion per formula unit randomly occupy the 16c positions, confirming that lithium insertion into Co_3O_4 results in displacement of the 8a Co^{2+} ions to empty 16c sites

iii) refinement of the number of Li^+ ions on the 8a sites yielded a positive occupancy resulting in a final refined stoichiometry of $Li_{1,54}Co_3O_4$.

These results indicate, rather unexpectedly, that lithiation of Co_3O_4 in excess of x = 1, results in occupation of the 8a sites by Li^+, rather than extrusion of cobalt. This indicates that metastable phases can be generated at ambient temperature in which small cations such as lithium can reside simultaneously in face-shared tetrahedra (8a) and octahedra (16c) with an intersite distance of only 1,8 Å (the ionic radius of Li^+ = 0,59 Å).

5.3 AMBIENT TEMPERATURE ELECTROCHEMICAL LITHIATION OF COBALT OXIDE

Ambient temperature electrochemical lithiation of cobalt oxide was carried out as a check on both the maximum degree of lithium insertion

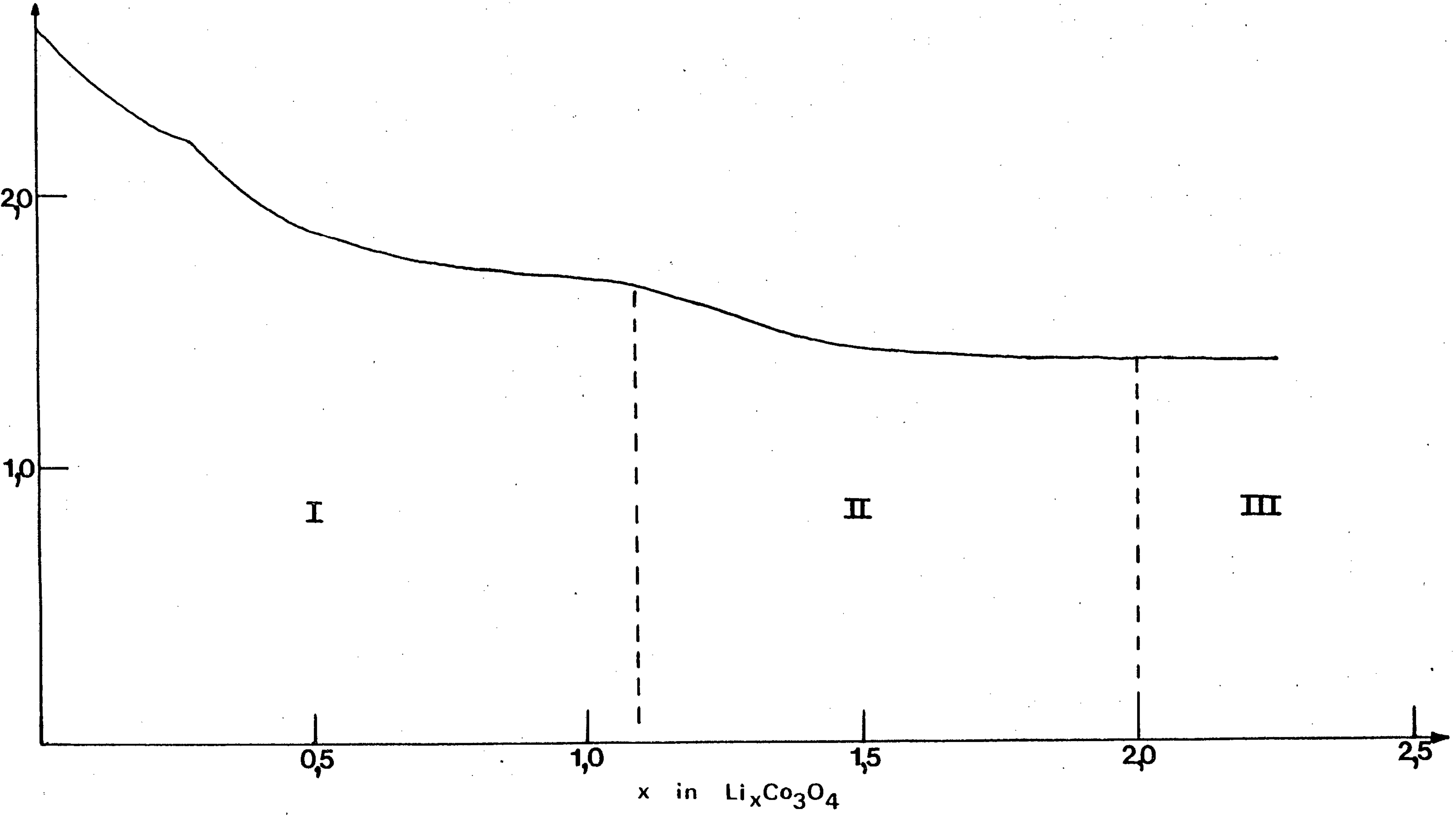

Figure 5.3:

Open-circuit-voltage vs x for Li/1M $LiBF_4$ in propylene carbonate/$Li_xCo_3O_4$

into Co_3O_4 and the conclusions drawn about the structure of $Li_xCo_3O_4$ as determined by chemical lithiation.

The plot of open-circuit voltage versus x for the Li/Co_3O_4 cell is given in Fig. 5.3. This plot is characterized by two single-phase regions I and II, in which lithium is inserted into the oxygen framework, and a two-phase region III, in which Li_2O and cobalt metal are generated by further discharge of the fully lithiated compounds. It was evident that Co_3O_4 can accommodate between 1,5 and 2,0 Li^+ ions per formula unit within its structure consistent with the results of chemical lithiation methods, and the structural refinement. Furthermore, from the break in the curve near $x = 1,0$, which separates phase I from phase II, it appears that the insertion process occurs in two steps as outlined in the following section. The open-circuit voltage versus x curve for electrochemical lithiation of Co_3O_4 is very similar to the corresponding curve for Fe_3O_4 [32].

5.4 CONCLUSIONS FOR LITHIATION OF COBALT OXIDE

Given the electrochemical information, the X-ray diffraction data obtained from the chemically lithiated samples and the results of the Lazy Pulverix and Wiseman programs, the following mechanism for insertion of lithium into Co_3O_4, is postulated:

$$Co^{2+}{}_{8a}[Co_2^{3+}]_{16d}O_4$$

$$\downarrow\ x_c\ Li$$

$$(Li^{+}{}_{x_c}Co^{2+})_{16c}[Co_2^{3+/2+}]_{16d}O_4$$

$$I \downarrow\ (1 - x_c)Li$$

$$(Li^{+}Co^{2+})_{16c}[Co_2^{3+/2+}]_{16d}O_4$$

$$II \downarrow\ 1,0\ Li$$

$$(Li^{+})_{8a}(Li^{+}Co^{2+})_{16c}[Co_2^{2+}]_{16d}O_4$$

$$III \downarrow\ 6,0\ Li$$

$$4Li_2O + 3Co$$

Cooperative displacement of the 8a-Co^{2+} ions to empty 16c octahedral sites, occurs at a critical Li^+ ion concentration, x_c. During reaction I, the 16c octahedral-site vacancies are filled by lithium, the end composition corresponding to the partially ordered rocksalt phase $(LiCo)_{16c}[Co_2]_{16d}O_4$. During reaction II, further insertion of lithium into the structure occurs, involving a filling of the tetrahedral sites by Li^+ ions. The $[Co_2]_{16d}O_4$ subarray remains intact during lithiation, and acts as a close-packed-anionic 3-dimensional framework for Li^+ ion transport. Lithiation beyond $x = 2$ results in a breakdown of the structure into the most probable products Li_2O and Co.

In the absence of cobalt extrusion the magnetic proportions of lithiated Co_3O_4 could possibly be explained in the following way:

The average formal cobalt valence balances the charge per formula unit during the mechanism proposed above i.e. lithium insertion into Co_3O_4 necessitates the reduction of Co^{3+} to Co^{2+}. Co_3O_4 has low spin $Co^{3+}(t_2^6\ e^0)$ on the B sites (16d sites). Co^{3+} is a d^6 ion and is generally low spin with no unpaired electrons and is therefore diamagnetic. At ambient temperature the A-site Co^{2+} couple antiferromagnetically. The question arises as to whether low spin Co^{3+} on the B sites becomes high spin Co^{2+} (a d^7 ion = $t_2^5\ e^2$) on lithiation of Co_3O_4, or whether the added electrons are itinerant to give $Co(^{3-x})(t_2^6\ \sigma^*)$ [118].

Moreover, with the large lattice expansion that occurs during lithiation, do the remaining diamagnetic low-spin Co^{3+} become high-spin Co^{3+} to give a high-spin mixed valency on the B-sites: $Co_{2-x}^{3+}Co_x^{2+} = t_2^{4+x}e^2$ with the x mobile electrons hopping between the cobalt ions. In any case a ferromagnetic coupling between Co^{2+} ions on the A-sites coupled antiparallel to magnetic cobalt on the B-sites can be expected to give an effective ferromagnetism. However X-ray data have shown that the Co^{2+} ions do not remain on the A-sites at least for extensive lithiation. It is clear that further work is necessary to establish the exact cause of the magnetic behaviour induced into Co_3O_4.

The value of x_c, the critical lithium concentration at which the 8a-cobalt ions are displaced to 16c sites still has to be determined. This is assumed to be small, $< 0,1$. The displacement of Co^{2+} from tetrahedral 8a to octahedral 16c sites probably occurs due to the electrostatic forces between Li^+ ions in 16c sites and the 8a-Co^{2+} ions. A 16c site of the spinel structure shares faces with two 8a sites on opposite sides. In Co_3O_4, the 8a sites are occupied by Co^{2+} ions, so a Li^+ ion in a 16c site would experience a strong electrostatic repulsive field from Co^{2+} ions in neighbouring 8a sites; at $x = x_c$ the electrostatic force is strong enough to push the Co^{2+} ions into neighbouring, empty 16c positions [32].

In view of the above results, it is possible to make the following conclusions about lithium insertion into Co_3O_4 at ambient temperature:

i) Li^+ ions can be inserted into the spinel structure of Co_3O_4 at ambient temperature.

ii) The $[Co_2]O_4$ subarray of the spinel structure remains intact during lithiation. This indicates the possibility of designing close-packed-anion framework structures in which the 16c-octahedral and 8a-(and possibly 48f) tetrahedral sites of the spinel structure offer a 3-dimensional interconnected interstitial space available for Li^+ ion transport.

iii) At a critical lithium-ion concentration, x_c (which is thought to be small), the 8a-site Co^{2+} ions are displaced to empty 16c octahedral sites.

iv) Co_3O_4 can accommodate nearly two Li^+ ions per formula unit within its structure. For $0 < x \leqslant 1$, Li^+ ions enter the 16c-sites of Co_3O_4. For $1 < x < 2$ Li^+ ions appear to enter the 8a tetrahedral sites. This result is unexpected particularly on account of the very short 8a-16c intersite distance (1,8 Å).

v) Lithiation of diamagnetic Co_3O_4 appears to induce ferromagnetic properties into the crystal.

SUMMARY

In comparison with other high temperature lithium/transition metal oxide cells investigated, such as the lithium/Fe_3O_4 cell [31], high temperature lithium/cobalt oxide cells perform rather poorly. They suffer from relatively short lifetimes and generally deliver high discharge capacities during the early cycles of cell operation only. The major problems of these cells appear to be an instability of $Li_{2x}Co_2O_{3+x}$, Co_3O_4 and CoO in the LiCl,KCl eutectic at 420 °C and the dispersion of the discharge product, Li_2O into the electrolyte. Although it would be of scientific interest to determine the nature and structure of the unidentified compound, $Li_{2x}Co_2O_{3+x}$, the family of cobalt oxide compounds cannot be regarded as attractive electrodes for high temperature, lithium batteries.

The results for the ambient temperature lithium/cobalt oxide cells are much more interesting. They indicate that Co_3O_4 can act as a close-packed-anion structure capable of lithium insertion and as such, shows promise for primary lithium battery applications requiring low current drain. Furthermore, these cells operate at ambient temperatures, which is far more desirable than the high temperatures necessitated by the higher power density cobalt oxide cells. These results have also emphasized the possibility of designing other close-packed-anion structures particularly those within the spinel family capable of lithium insertion that could act as "solid solution" electrodes. In particular a wide variety of transition metal ions can be stabilized on the B sites of the spinel structure, which promises the possibility of being able to tailor the redox potentials of spinel electrodes in lithium batteries.

REFERENCES

1. D A J Rand, J. Power Sources, **4** (1979) p 101.

2. Electric Vehicle Symposium, CSIR, Institute of Electrical Engineers, Pretoria, 10 and 11 April (1979).

3. Electric Vehicles, Select Committee on Science and Technology, House of Lords Session (1979-80) 1st Report.

4. Electr. Vehicle News, **6** (1977), p 28.

5. W J Walsh, Physics Today, June (1980), p 34.

6. D W Murphy and P A Christian, Science, **205** (1979), p 651.

7. B B Scholtens and W van Gool, "Solid Electrolytes", Academic Press Inc., New York (1978), p 463.

8. H Shimotake, W J Walsh, E S Carr and L G Bartholme, 11th IECEC, p 471.

9. M Ewing, Electronics and Power, July/August (1982), p 523.

10. P Chapman, G Charlesworth and M Baker, Future Transport Fuels, TRRL Suppl. Rep. 251, Transport and Road Research Lab., Crowthorne, England (1976).

11. J H B George, L J Stratton and R G Acton, Prospects for Electric Vehicles, Arthur D Little, Rep. to US, Dept. HEW, NAPAC, Arlington, Va, May (1968).

12. E J Cairns and H Shimotake, Science, **164** (1969), p 1347.

13. S Gross, Energy Conversion, **15** (1976), p 95.

14. Form a precis of a talk given by Dr J Coetzer and Dr M M Thackeray on "High Energy Density Electrochemical Cells" at the CSIR, 19 June (1979).

15. J Birge, J T Brown, W Feduska, C C Hardman, W Pollock, R Rosey and J Seidel in D H Collins (ed.), Power Sources, **6**, Academic Press, London (1977), p 111.

16. N Weber and J T Kummer, Adv. Energy Conv. Eng. ASME Conf., Florida (1967), p 913.

17. B C Tofield, R M Dell and J Jensen, Nature, **276** (1978), p 217.

18. R M Dell and R J Bones, "Fast Ion Transport in Solids", Elsevier North-Holland Inc., (1979), p 29.

19. C R Peters, H Bettman, J W Moore and M D Glick, Acta Crystallogr., B **27** (1971), p 1826.

20. F R Foulkes and P T Choi, Canadian J. of Chem. Eng., **56** (1978), p 236.

21. C A Beevers and M A S Ross, Krist., **97** (1937), p 59.

22. R M Dell, J L Sudworth and I Wynn Jones, 11th IECEC, p 503.

23. N Weber and I T Kummer, "Session on Vehicle Propulsion Batteries" p 37.

24. E C Gay, T D Kaun and F J Martino, 11the IECEC, p 477.

25. C R Barker, Electr. Vehicles Q, June (1978), p 24.

26. E V Focus, **1** No. 9, June 15 (1978), p 6.

27. F C Mrazek and J E Battles, "High Performance Batteries for Off-Peak Energy Storage and Electric Vehicle Propulsion" Progress Report for the Period January-June 1974, ANL-8109, p 72, Argonne National Laboratory (1975).

28. R K Steunenberg, A E Martin and Z Tomczuk, "Improved Cathode Composition for Electrochemical Cell", US Patent No. 3 941 612 (1976).

29. H Shimotake and L G Bartholme, "High Performance Batteries for Off-Peak Energy Storage and Electric Vehicle Propulsion", Progress Report for the Period July-December 1974, ANL-75-1, p 32, Argonne National Laboratory (1975).

30. N A Godshall, I D Raistrick and R A Huggins, Mat. Res. Bull., **15** (1980), p 561.

31. M M Thackeray and J Coetzer, Mat. Res. Bull., **16** (1981), p 591.

32. M M Thackeray, W I F David and J B Goodenough, Mat. Res. Bull., **17** (1982), p 785.

33. M M Thackeray, W I F David and J B Goodenough, J. Solid State Chem., 55 (3), (1984), p 280.

34. M S Whittingham, "Intercalation Chemistry", Academic Press Inc. (1982), p 1.

35. A H Thompson and F J Di Salvo, "Intercalation Chemistry", Academic Press Inc. (1982), p 573.

36. F Levy, ed., "Intercalated Layered Materials", D. Reidel, Holland (1979).

37. M M Thackeray, W I F David, P G Bruce and J B Goodenough, Mat. Res. Bull., **18** (1983), p 461.

38. M S Whittingham, J. Electrochem. Soc., **123** (1976), p 315.

39. M S Whittingham and M B Dines, J. Electrochem. Soc., **124** (1977), p 1387.

40. B E Liebert, PhD Thesis, Stanford University (1977).

41. P G Dickens, S J French, A T Hight and M F Pye, Mat. Res. Bull., **14** (1979), p 1295.

42. M Eisenberg, "Proc. 28th Power Sources Symposium", Atlantic City, New Jersey, June (1978), p 155.

43. M Eisenberg, United States Patent [19], 4 136 233, (1979).

44. M S Whittingham, "Fast Ion Transport in Solids", P D Vashishta, J N Mundy and G K Shenoy (eds.), Elsevier North-Holland Inc. (1979).

45. M S Whittingham, "Intercalation Chemistry: An Introduction", Academic Press Inc. (1982), p 15.

46. M S Whittingham and F R Gamble, Jr., Mat. Res. Bull., **10** (1975), p 287.

47. M S Whittingham and J A Panella, Mat. Res. Bull., **16** (1981), p 37.

48. K Mizushima, P C Jones, P J Wiseman and J B Goodenough, Mat. Res. Bull., **15** (1980), p 783.

49. G Pistoia, J. Power Sources, 9 (1983), p 307.

50. D W Murphy, P A Christian, F J Di Salvo and J N Carides, J. Electrochem. Soc., **126** (1979), p 497.

51. D W Murphy, M Greenblatt, J Cava and S M Zahurak, Solid State Ionics, 5 (1981), p 327.

52. R J Cava, A Santoro, D W Murphy, S Zahurak and R S Roth, Solid State Ionics, 5 (1981), p 323.

53. D W Murphy, P A Christian, F J Di Salvo, J N Carides and J V Waszczak, J. Electrochem. Soc., **128** (1981), p 2053.

54. K A Wilhelmi, K Watterson and L Kihlborg, Acta. Chem. Scand., **25** (1971), p 2675.

55. P G Dickens and M F Pye, "Intercalation Chemistry", Academic Press Inc. (1982), p 539.

56. J S Gore and C R Walk, US Patent 3 929 504 (1975).

57. D W Murphy, P A Christian, F J Di Salvo and J V Waszczak, Inorg. Chem., **18** (1979), p 2800.

58. P Hagenmuller, J Galy, M Pouchard and A Casalot, Mat. Res. Bull., **1** (1966), p 45.

59. A H Thompson and F J Di Salvo, "Intercalation Chemistry", Academic Press Inc. (1982), p 573.

60. K H Cheng, A J Jacobson and M S Whittingham, Solid State Ionics, **5** (1981), p 355.

61. K H Cheng and M S Whittingham, Solid State Ionics, **1** (1980), p 151.

62. D W Murphy, P A Christian, J N Carides and F J Di Salvo, "Fast Ion Transport in Solids", P D Vashishta, J N Mundy and G K Shenoy (eds.), Elsevier North-Holland Inc. (1979), p 149.

63. D W Murphy, F J Di Salvo, J N Carides and J V Waszczak, Mat. Res. Bull., 13 (1978), p 1395.

64. H Y P Hong, J. Power Sources, 5 (1980), p 137.

65. W I F David, J B Goodenough, M M Thackeray and M G S R Thomas, Revue de Chimie Minérale, **20** (1983), p 636.

66. R G Burns and V M Burns, 2nd Int. Symp. on MnO_2, The Electrochemical Society (Cleveland Section), Tokyo (1980), p 97.

67. H Ikeda, T Saito and H Tamura, 1st Int. Symp. on MnO_2, The Electrochemical Society (Cleveland Section), Cleveland, Ohio (1975), p 384.

68. G Pistoia, J. Electrochem. Soc., **129** (1982), p 1861.

69. T Kahara, T Horiba, K Tamura and M Fujita, Proc. Symp. on Power Sources for Biomedical Implantable Applications and Ambient Temperature Lithium Batteries, B B Owens and N Margalit (eds.), The Electrochemical Society, Princeton, New Jersey (1980), p 300.

70. M Voinov, Electrochim. Acta, **26** (1981), p 1373.

71. V Manev, personal communication with G Pistoia.

72. R R Cianelli, J. Crystal Growth, **34** (1976), p 239.

73. J B Goodenough, "Magnetism and the Chemical Bond", Wiley, New York, London (1963).

74. D G Wickham and W J Croft, J. Phys. Chem. Solids, **7** (1958), p 351.

75. V Janovee, V Dvorak and J Petzelt, Czech. J. Phys., B**25** (1975), p 1362.

76. J B Goodenough, "Solid Electrolytes", Chp. 23, P Hagenmuller and W van Gool (eds.), Academic Press, New York (1978).

77. M S Whittingham, Science, **192** (1976), p 1126.

78. J B Goodenough, K Mizushima and T Takeda, Jap. J. Appl. Phys., **19** , Suppl 19-3 (1980), p 305.

79. W A Deer, R A Howie and J Zussman, "Rock-Forming Minerals, **11** Volume 5, Longmans (1971), p 57.

80. A Cotton and G Wilkinson, "Advanced Inorganic Chemistry", (3rd Ed.), John Wiley and Sons, Inc. (1972), p 50.

81. W H Bragg, Phil. Mag. **30** (1915), p 305.

82. S Nishikawa, Proc. Tokyo Math. Phys. Soc., **8** (1915), p 199.

83. E J W Verwey and E L Heilmann, J. of Chem. Phys., **15** (4) (1947), p 174.

84. A F Wells, "Structural Inorganic Chemistry" (2nd Ed.), Oxford University Press (1950), p 379.

85. E J W Verwey, P W Haayman and F C Romeijn, J. of Chem. Phys., **15** (4) (1947), p 181.

86. C Zener and R R Heikes, Rev. Mod. Phys., **25** (1953), p 191.

87. J Shanker and V P Gupta, J. Phys. Chem. Solids, **41** (1980), p 141.

88. ASTM Powder Diffraction File 9-402.

89. "Handbook of Chemistry and Physics" (57th Ed.), CRC Press Inc. (1976-1977).

90. E C Gay, D R Vissers, F J Martino and K E Anderson, J. of Electrochem. Soc., **123** (1976), p 1591.

91. N P Yao, L A Heredy and R C Saunders, J. Electrochem-Soc., **118** (7) (1971), p 1039.

92. H A Laitinen, R P Tischer and D K Roe, J. Electrochem. Soc., **107** (1960), p 546.

93. B M L Rao, R W Francis and H A Christopher, J. Electrochem. Soc., **124** (10) (1977), p 1490.

94. W K Behl and D L Beals, US Army Electronics Command, Ft. Monmouth, New Jersey, Report ECOM-3166, D A Task No. ITO 61102A 34A 00, Aug. (1969).

95. E S Buzzelli, US Patent 3 445 288 (1969).

96. J S Dunning, T G Bradley and E J Zeitner, 11th IECEC, p 491.

97. L P Costas and R P Marshall, Trans. Met. Soc., AIME **224** (1962), p 970.

98. E D Levine and E J Rapperport, Trans. Met. Soc., AIME **227** (1963), p 1204.

99. G Grube, L Mohr and W Breuning, Z. Elektrochem., **41** (1935), p 880.

100. F I Shamnay and P Ya Saldau, Izvest. Akad. Nauk. SSSR Otdel. Khim, Nauk 631 (1937).

101. H A Adams, US Patent 3 428 493, February 18 (1969).

102. E Elchardus and P Laffitte, Bull. Soc. Chim. France, **51** (1932), p 1572.

103. M M Thackeray, PhD Thesis, University of Cape Town (1977).

104. J G Gibson and J L Sudworth, "Specific Energies of Galvanic Reactions and Related Thermodynamic Data", Halsted Press, New York (1973).

105. J P Mathers, T W Olszanski and J E Battles, J. Electrochem. Soc., **124** (8) (1977), p 1149.

106. R A Sharma, Ceramic Bulletin 57 (12) (1978), p 1103.

107. R B Swaroop, G Bandyopadhyay, J T Dusek and T M Galvin, "High Performance Batteries for Electric Vehicle Propulsion and Stationary Energy Storage", Progress Report for the period October 1977 - September 1978, Argonne National Laboratory.

108. F Daniels and R A Alberty, "Physical Chemistry" (4th Ed.), J Wiley and Sons Inc. (1975), pp 92-94.

109. P J Durrant, "General and Inorganic Chemistry", Longmans, Green and Co (1948), p 176.

110. F Daniels and R A Alberty, "Physical Chemistry" (4th Ed.), J Wiley and Sons Inc. (1975), pp 198-199.

111. H J Creighton, "Principles and Applications of Electrochemistry", Volume 1 (4th Ed.), J Wiley and Sons Inc. (1947), p 236.

112. D G Peters, J M Hayes and G M Hieftjie, "Chemical Separations and Measurements: Theory and Practice of Analytical Chemistry", W B Saunders Co (1974), p 397.

113. B D Cullity, "Elements of X-ray Diffraction" Addison-Wesley Publ. Co (1956), p 324.

114. P J Brown and J B Forsyth, "The Crystal Structure of Solids", Arnold, London (1973).

115. F A Cotton and G Wilkinson, "Advanced Inorganic Chemistry" (3rd Ed.), J Wiley and Sons Inc. (1972), p 874.

116. Tariano and Tokich, Trans. Met. Soc., AIME 175 (1948), p 728.

117. ASTM Powder Diffraction File 9-418.

118. M M Thackeray, personal communication with J B Goodenough.